PHYSICAL MODELLING OF THE LIGHTNING LEADERS INTERACTION WITH TALL GROUNDED OBJECTS AND ITS VALIDATION WITH OBSERVATIONS

CHAN MING KIT

Ph.D.

The Hong Kong Polytechnic University

2018

The Hong Kong Polytechnic University

Department of Building Services Engineering

Physical Modelling of the Lightning Leaders Interaction with Tall Grounded Objects and Its Validation with Observations

CHAN Ming Kit

A thesis submitted in partial fulfillment of the requirements for the Degree of Doctor of Philosophy

October 2017

Certificate of Originality

I hereby declare that this thesis is my own work and that, to the best of my knowledge and belief, it reproduces no material previously published or written, nor material that has been accepted for the award of any other degree or diploma, except where due acknowledgment has been made in the text.

_____ (Signed)

CHAN Ming Kit (Name of student)

Abstract

With the advance in smart society, more and more tall grounded objects equipped with high-tech facilities that are sensitive to lightning have been built around the world. Such tall objects include high-rise buildings, communication towers, power transmission line towers, wind turbines etc. When a thundercloud is growing over a tall earthed object, more and more charges accumulate in the cloud, causing the ambient electric field strength below the charged cloud base increases. If the electric field enhancement at the surface of the object reaches a certain critical value, an electrical breakdown process will occur there. This breakdown process may lead an upward leader starting from tip of the object and propagating towards the charged cloud, i.e. an upward lightning discharge is initiated. Since the upward lightning discharge is often with a large peak current and a long duration of continuous current, it may damage the object itself as well as the facilities and lives inside it.

Most upward lightning from grounded objects are negative discharges initiated by upward positive leader (UPL). An UPL can be either self-initiated from a tall grounded object or triggered by other discharge, such as a negative downward leader (DNL) approaching the object. Although there are many observations of UPLs, statistical analysis is not enough to reveal the physical process of UPLs. Modeling of UPLs initiation and propagation is an effective way to reveal the mechanism of UPLs. Therefore, this study aimed at the modeling study of initiation of upward lightning from a tall grounded object for lightning protection analysis. Major works done in this study are summarized as following.

i. A brief review of the classification of different upward lightning was done. The review included: 1) up-to-date observation results of lightning attachment process; 2)

physical characteristics of both positive and negative leaders from both observations and theoretical modeling; 3) properties of the corona space charge layer near the ground during a complete lightning process; and 4) observed optical and electromagnetic features of self-triggered and other-triggered UPLs. (see Chapter 2).

ii. A macroscopic physical model that can simulate an upward leader self-initiated from a tall earthed object under various conditions was developed. Major assumptions and concepts in the model included: 1) a three-zone leader channel structure is defined; 2) the first leader segment is created when the local electric field enhancement on the top of a grounded object reaches the critical breakdown electric field in a certain range; 3) the leader speed is subjected to the conservation of energy and mass inside the streamer-to-leader transition zone around the leader head; 4) a steady leader requires the leader initial speed (energy) should be larger than the minimum (critical) speed observed for leaders in both field and lab experiments ($\approx 10^4$ m/s), which corresponding to a critical corona sheath radius hence a critical corona sheath charge ahead of the leader; 5) the leader charge distribution is calculated by charge simulation method (CSM); 6) the leader ceases when its channel electric field is larger than the ambient electric field. Our calculation shows that the estimated critical corona sheath charge is height dependent. By fine-tuning the energy loss factor, this estimated critical value at ground-level can match well with experimental results. (see Chapter 3).

iii. The above model was applied to an UPL self-initiated from a tall structure under various thunderclouds with and without corona space charge layer effect. Based on the leader initiation criteria, the critical corona sheath length and minimum corona charge as a function of the leader initiation height and the minimum leader initiation height as a function of the thundercloud condition for UPL are estimated and discussed. Simulation

results show that the estimated minimum leader initiation height is higher when the electric field due to the corona space charge layer near the ground is considered. Evolutions of the speed, charge distribution, current, electric field, conductance and conductivity, and channel size of UPL under different thundercloud conditions are also obtained and discussed. Our simulation results have been compared to other existing models. Results are quite similar. In addition, the model is tested with two sets of experiment data. Using a similar initial condition, the increasing trend of our proposed core radius equation can match well with the experimental result. (see Chapter 4).

iv. The model was further modified and used to study an UPL triggered by a DNL from a tall grounded object under different circumstances. With the modified model, general properties of an DNL, as well as the spatial and temporal electric field profile caused by the DNL are evaluated and discussed. By taking into account the vertical electric field profile due to the both the thundercloud and the DNL, multiple UPLs triggered from different heights of grounded objects are simulated and discussed. For validation, two case studies of lightning attachment (UPL connecting to DNL) reported in observations are modelled with the model and promising results are obtained. Our model can also estimate other leaders' physical parameters and the ground electric field change among different horizonal distances. (see Chapter 5).

Publications arising from the thesis

Journal Paper

Chan, M., M. Chen, and Y. Du (2018a), A Macroscopic Physical Model for Self-Initiated Upward Leaders from Tall Grounded Objects and Its Application, *Atmos. Res*., 200, 13-24, doi.org/10.1016/j.atmosres.2017.09.012.

Chan, M., M. Chen, and Y. Du (2018b), Modeling of the Attachment Process Prior to First Return Stroke in Lightning to High-rise Building and Its Application to Observations. (In preparation)

Conference Paper

Chan, M., M. Chen, and Y. Du (2017), A simple physical model for self-triggered upward leaders from high-rise buildings, in: The 33rd International Conference on Lightning Protection (ICLP), 25th - 30th September, 2016, (Estoril, Portugal: IEEE).

Acknowledgements

I would like to express my sincere thanks to my supervisors, Dr. Mingli Chen and Prof. Ya-ping Du, for their professional guidance, enthusiastic encouragement and useful critiques of the research study. In addition, I should be grateful for the Research Grants Council of Hong Kong Government, for its generous stipend to cover my tuition fees and living expenses. Finally, I wish to thank my family members for their support and encouragement throughout my study.

Table of contents

List of Figures

List of Tables

Chapter 1

Introduction to Lightning Physics

1.1 Background on Lightning Discharges

Lightning is a high-current electric discharge. It occurs suddenly in a short period of time. Based on observation results (*Rakov and Uman*, 2003; *Rakov*, 2016), all lightning discharges can be simply classified into two types: either they can bridge the gap between the thundercloud and the Earth or cannot. About 75% of lightning results from the discharge either within clouds or in the air. They are intra-cloud (IC), cloud-to-cloud (CC), and cloud-to-air discharges. When the electric field within a cloud overcomes the electrical resistance of the air, the CC lightning discharge occurs. The remaining 25% of lightning strikes are the more considerable events that involves an object on the ground or in the atmosphere, such as aircrafts (*Williams and Heckman*, 2012). Observation results (*Rakov and Uman*, 2003; *Rakov*, 2016) also summarized four different types of lightning discharges between clouds and the Earth: 1) downward negative lightning, 2) downward positive lightning, 3) upward positive lightning and 4) upward negative lightning. These four types of discharges are usually termed cloud-to-ground (CG) or ground-to-cloud discharges. Among the four types of lightning discharges, negative CG lightning that transports negative charges to the ground is the most common.

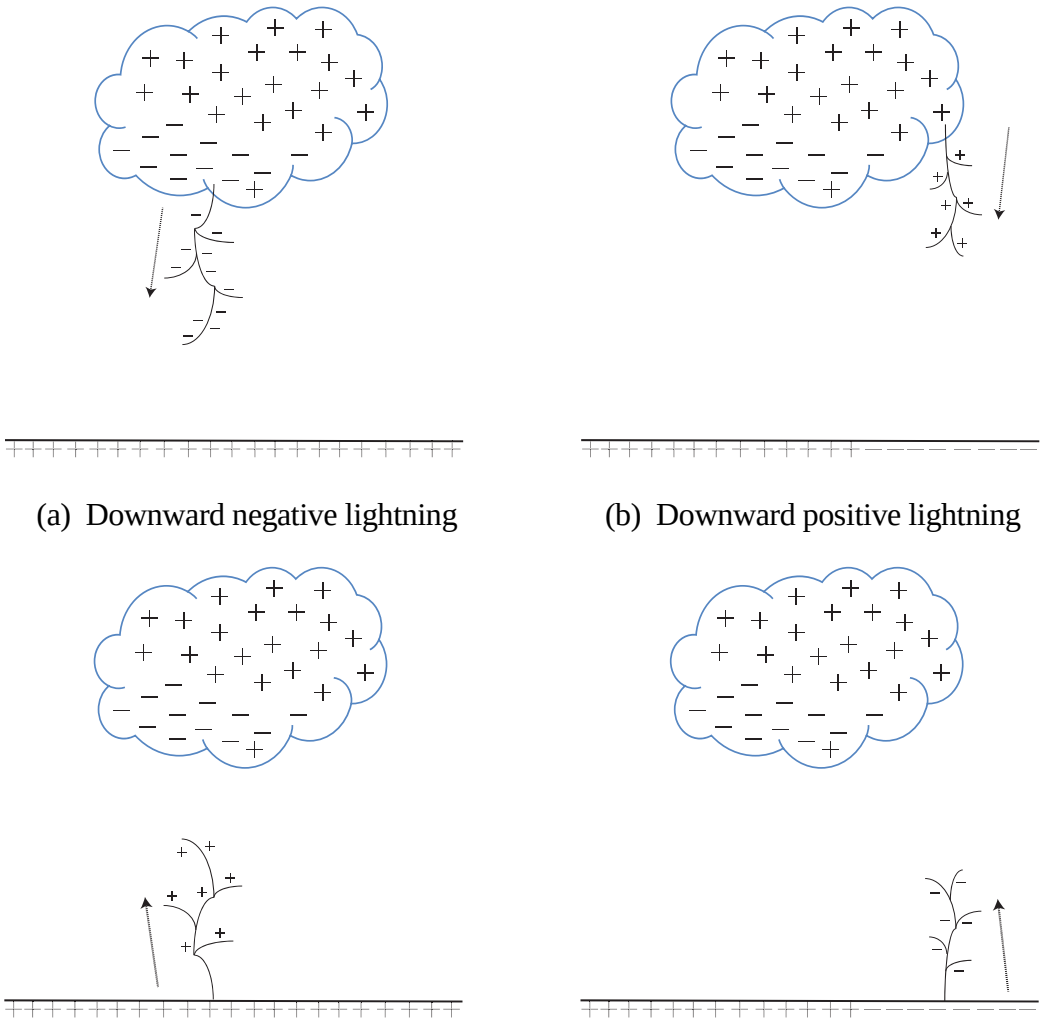

(a) Downward negative lightning (b) Downward positive lightning

(c) Upward negative lightning (d) Upward positive lightning

Figure 1.1. Schematic of four types of CG lightning.

Some observation results also show both positive and negative charges sequentially transferring to the ground during the same flash called bipolar lightning discharges (*Saraiva et al*., 2014). In addition to the natural lightning, lightning can also be triggered artificially by rocket-and-wire technique towards a thundercloud overhead (*Fieux et al*., 1975; *Chen et al*., 2003).

When a DNL approaches the ground, the surface electric fields of earthed objects increase. If the surface electric field of any object exceeds the critical breakdown value, an UPL will be initiated at that object and the attachment process starts. This process ends when one of the streamer zones of triggered UPLs succeed to connect the DNL's streamer zone. After that, a highly conductive path is created within the connected streamer zone and a bidirectional current wave is initiated. One of the current wave moves toward the thundercloud, and the other is drained to the grounded object and reflected from the ground, finally catches up with the upward wave front. This high-current flow can heat up the conducting channel path to nearly 30000 K. Oxygen and nitrogen in the air can react to form nitrogen oxides ($NO_x = NO + NO_2$) at this high temperature. Meanwhile, the sudden increase in channel pressure ($\Delta P \approx 10$ atm or more) and temperature can produce a rapid expansion of the surrounding air. This rapid expansion creates shock waves that produce the sound of thunder. Apart from that, if the ground surface is completely flat, the first return stroke can also occur without any initiation of upward connecting leader (UCL).

Usually, a first return stroke can only neutralize some of the negative ions near the cloud base. If the remaining charges in the cloud are enough to produce another stroke, a continuous leader called a dart leader will move down the residual first-stroke channel, depositing negative charge along the channel. Again, when a dart leader approaches to the ground, upward leaders initiate from grounded objects, a similar leader attachment process takes place. When the descending dart leader is connected to one of these upward leaders, a subsequent return stroke phase occurs.

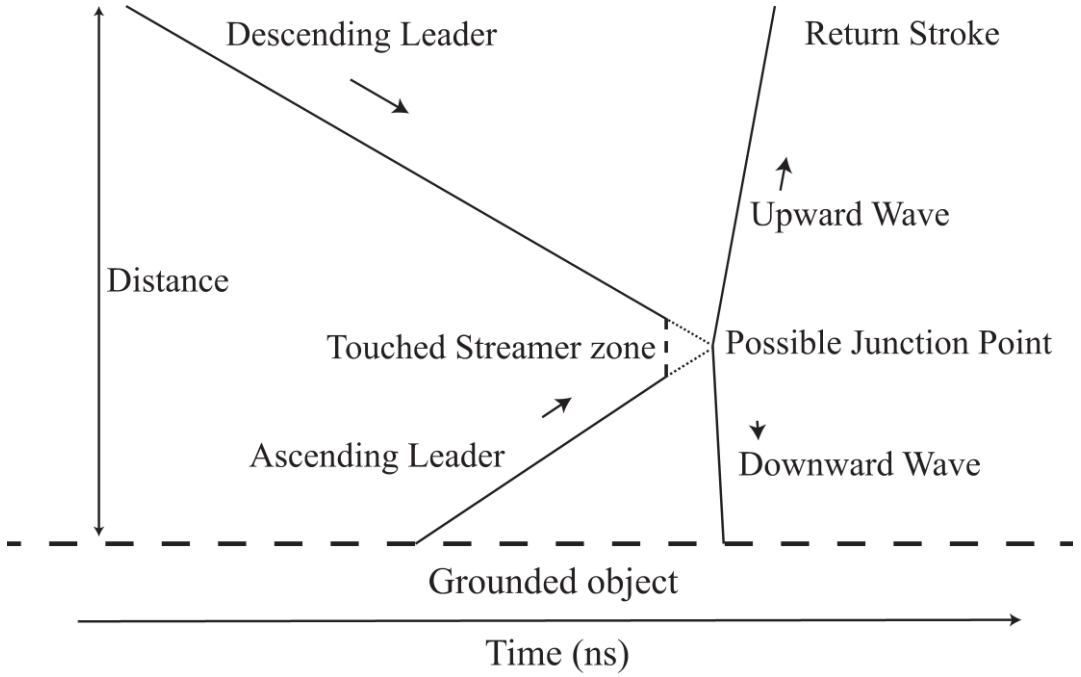

Figure 1.2. A simplified schematic illustration of the lightning initiation sequence.

Nowadays, lightning interaction with tall structures has been attracting a great deal of attention. One of the reason is because of the rapid expansion of wind power generating stations (*Montanyà et al*., 2014) and transmission towers (*Baba and Rakov*, 2016). There is a common assumption that if the height of an object is above 500 m, it will only experience upward lightning discharges (*Diendorfer*, 2014). Numerical modeling of the upward leader evolution is important for understanding the mechanism of lightning initiation and determining the electrical parameters of this type of discharges. These parameters are essential for us to design effective lightning protection systems for tall grounded objects, such as transmission towers and wind mills. Even though the inception mechanism and criterion of upward leaders has been studied for a few decades, usually, the leader charge distribution and leader's velocities were taken from the experimental data and only a continuously growing leader was considered. The charge density was fixed as a constant along the leader as well. Therefore, it is necessary to develop a better physical model.

1.2 Research Objectives

Our main objective of this project is to study the lightning leader interaction with tall grounded objects, before the final breakdown occurs. First, we will develop a macroscopic physical model that can simulate an upward leader self-initiated from a tall grounded object under various conditions. Second, we will apply the model to an UPL self-initiated from the top of a tall grounded object with or without the consideration of the effect of space charge layers near the ground. This model is tested with two experiments for validations. We further modify the model to simulate a DNL propagation. Then, by considering the spatial and temporal vertical electric filed due to the DNL and the charged cloud, some UPLs triggered from different heights of grounded objects will be evaluated. Finally, simulation results will be compared with an observation for validations and modifications.

1.3 Synopsis of the Thesis

This thesis begins to review the basic understanding of lightning leader in Chapter 2. Details of our proposed self-triggered UPL model are described in Chapter 3. Simulation results and validation of this model are presented and discussed in Chapter 4. In Chapter 5, a physical DNL model and its spatial and temporal electric field changes profile are presented. This is done by modifying our proposed UPL model. Some examples and two case studies of lightning leader attachment are also evaluated and discussed in this chapter. Finally, we will summarize all the present studies in Chapter 6.

Note that, the atmospheric electricity sign convention: a negative electric field on the ground indicates the presence of negative charge overhead is used in this thesis.

Chapter 2

Literature Review

2.1 Introduction

Under fair-weather conditions, the ambient electric field (E_A) near the ground surface is about 100 – 130 V/m. If there is a large charged cloud growing under the ground surface, the value of E_A will increase. If the electric field enhancement at the surface of any grounded object reaches a certain critical value, an electrical breakdown process will occur there. This breakdown process may lead an upward leader starting from the tip of this object and propagating towards the charged cloud, i.e. an upward lightning discharge is initiated. Since the upward lightning discharge is often with a large peak current and a long duration of continuous current, it may damage this object itself as well as the facilities and lives inside it.

Usually, the most common way to measure the value of E_A verse altitude within the troposphere is balloon soundings (*Nicoll*, 2012). Observation results (*Stolzenburg et al*., 2002, 2007) show that the value of E_A in each leader process below the cloud base is nearly uniform. In addition to balloon soundings, field mills are often used to measure the value of E_A on the ground. Field mills, which convert the slowly time varying electric field into an amplitude moderated ac voltage, can determine the static and slowly time varying electric field on the ground.

In this chapter, we will give a brief review of some recent observations and theoretical modeling of the leader part of upward lightning discharges.

2.2 Space Charge Layer Effect due to Corona at Ground Level

Willett et al. (1999) did an ambient-field distribution measurement in Florida during the summer of 1996. They used field mills that were carried by a rocket to measure the vertical electric field up to an altitude of about 4 km. In their experiment, one of the rocket measured the ground-level electric field was about -6 kV/m, and it increased with height to about -24 kV/m at 500 m above ground. When the rocket reaches higher, the field stayed relatively constant. Experiential results showed the increasing electric field was attributed to space charge layers. Space charge layer means the space charges in the space between the ground and the cloud base. The electric field at ground level due to the space charge layer varies slowly over time scales of seconds to minutes. As the duration of a lightning leader is within a hundred of milliseconds, we can assume the electric field profile is time independent during the leader process. *Toland* and *Vonnegut* (1977) also reported the ground-level electric field over a lake in New York ranging from -38 to -130 kV/m.

When a thunderstorm is formed, a corona discharge is initially initiated from a tall grounded object and the corona space charge injected near the top of the object could inhibit the corona development at ground level. Meanwhile, many coronating points near the ground surface together create an additional space charge layer. This effect is practically important for lightning protection.

2.3 Self-initiated Upward Leaders from Grounded Objects in Upward Discharges

In this section, we are going to make a brief review about the leader part of upward lightning discharges. A full comprehensive description of the upward lightning can be found in a well-known reference book written by *Rakov* and *Uman* (2003). Usually, every upward lightning can be classified into three types: 1) upward negative lightning, 2) upward positive lightning and 3) upward bipolar lightning:

Upward negative lightning discharges are initiated by upward positive leaders from the tops of grounded objects. Positive leaders can move either continuously or in a stepped fashion. The leader bridges the gap between the object and the negative charge source in the cloud and serves to establish an initial continuous current. The upward positive leader and initial continuous current constitute the initial stage of an upward flash.

Upward positive lightning discharges are initiated by upward negative leaders from the top of a grounded object bridging the gap between the object and the in-cloud discharge channel. Observation results showed that most of the upward negative leaders propagate stepwise.

Bipolar lightning discharges are often initiated by an upward leader from a tall grounded object, but they can also be cloud-to-ground flashes. It is a lightning event where the current waveform measured at the channel base exhibits a polarity reversal within the same flash. Although bipolar flashes have been investigated by observation measurements of lightning currents on tall towers for more than seven decades, the physical theory of bipolar lightning is poorer than that of either negative or positive lightning. Modern high-speed video images and correlated current records can help us to get a better understanding

of this lightning discharges phenomenon and the corresponding physical mechanism. One of the possible explanation can be found in **Figure 2.1**.

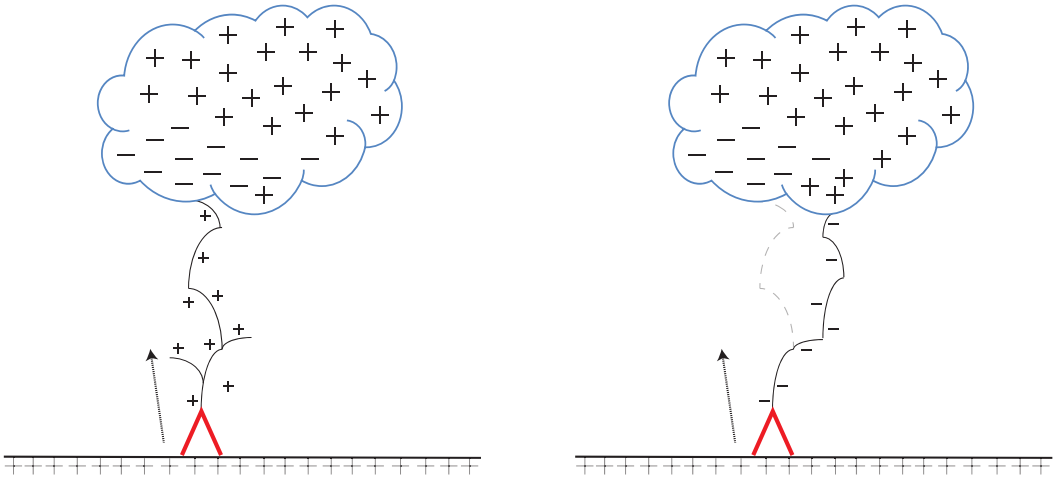

(a) (b)

Figure 2.1. A possible explanation of observed bipolar upward lightnings.

2.4 Electric Field Characteristics of Upward Discharges

Because of the different electric field waveforms, each upward lightning can be identified as either self-initiated or other-triggered through the E-field measurement, which can be measured by flat plate antennas.

E-field measurements show that while the waveform of the self-initiated upward lightning is containing a sudden and rapid electric field change without significant field change before the lightning discharge occurs, the electric field waveform of the other-triggered upward lightning can observe an opposite polarity field change before the upward lightning was initiated.

2.5 UCLs Triggered from Grounded Objects by a Downward Leader during Downward Discharges

When a downward leader approaches the ground, if the enhanced surface electric field reaches the critical value, an upward leader will be either initiated on the ground or at the surface of a grounded object. Then the lightning attachment process starts. When both streamer zones ahead of the downward and upward leaders come in contact, the first return stroke begins and a large bidirectional current flow starts to move from the connected streamer zone to the charged cloud. In addition to the downward negative flash, *Saba et al*. (2015) have observed a downward positive leader (DPL) initiates an upward negative connecting leader in the U.S.

Sometimes, the down-coming leader can initiate more than one upward leaders without connecting. *Warner* (2012) has observed upward lightning leaders initiated simultaneously from different tall towers in Rapid City. As the induced electric field due to the downward leader is transient, unconnected upward leaders may stop propagating.

2.6 Simplified Leader Structure

Although a lightning leader is a complex structure, it can be simply separated into three parts: the streamer zone, the leader tip and the channel. The leader tip is brighter than either the leader channel or the streamer zone. There is also a streamer-to-leader transition that converses a cold streamer corona discharge to a hot leader channel.

It is generally believed that the leader core channel is a plasma formation characterized by a temperature of order 10^4 K and relatively high conductivity of order 10^4 S/m. Therefore, leader tip looks like a high-voltage electrode and the streamer zone can be viewed as a machine that the electrical energy in the gap is made available to the

extending leader channel. **Figure. 2.2** shows a simplified explanation for a new channel segment adds to the leader. In a millisecond scale, while the positive leader tends to grow continuously, the growing mechanism of a negative leader is more complex and shows stepwise behaviour.

A brief description of the growth of a negative leader as follow: First, when a space leader breakdown takes place in the air, it tends to extend in two directions, the positive charged one towards the tip of the leader and the other in the opposite direction. At this moment, as the potential difference in the gap between both leaders is large, a burst of negative corona flash occurs and generates a large flux of thermal runaway electrons. These energetic electrons subsequently produce bremsstrahlung radiation (*Moore et al*., 2001; *Xu et al*., 2014). When the tip of the space leader meets the tip of the stepped leader, they merge together to from a longer stepped leader channel.

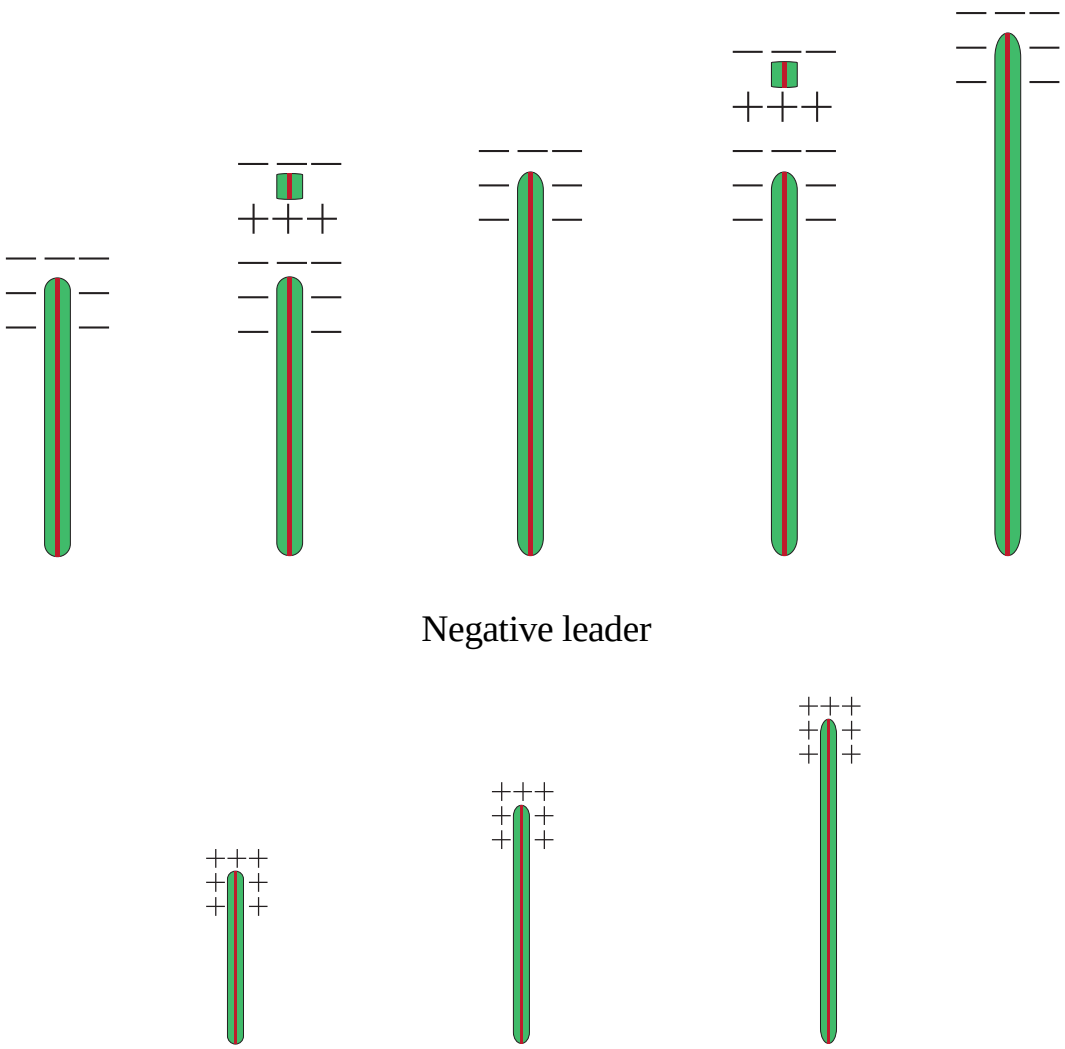

Figure 2.2. Schematic plot for concept of the negative (top panel) and the positive (bottom panel) leaders in the air.

2.7 Observed Characteristics of UPLs and DNLs

Wang and *Takagi* (2012) have summarized two types of upward lightning initiation. One is called “self-initiated” and the other is called “other-triggered”. It is commonly assumed that while the self-initiated lightning is self-initiated at the top of a tall object, whenever the electric field produced by the thundercloud exceeds a certain level, the other-triggered lightning is also initiated at the top of a tall object but is triggered by a nearby

preceding lightning activity, such as a DNL and the first return stroke, causing a sudden polarity change. The initial stage of the upward lightning is characterized by a leader moving up from the top of the object towards the thundercloud. This leader can produce a slowly rising continuous current. *Wang et al*. (2008a) have also reported three upward bipolar lightning flashes observed from a windmill and its lightning protection tower.

For the DNLs, *Chen et al.* (1999) have observed a luminosity wave from the leader tip propagates back to the leader channel. Later, *Hill et al.* (2011) have used high speed video cameras to observe this upward-propagating wave. Both observational results showed that down-coming negative lightning leaders exhibit stepwise behavior. A detailed description of this mechanism can be found in (*Dwyer and Uman*, 2014). In addition, a statistical analysis (*Campos et al*., 2014) has summarized the 2-D speed of DNLs is in a range of 0.90-19.8 $\times 10^5\, ms^{-1}$, with an average value of 3.30 $\times 10^5\, ms^{-1}$.

2.8 Modeling of Upward Leaders

Nowadays, many existing lightning leader channel models are based on the Gallimberti's thermo-hydrodynamical model (*Gallimberti*, 1979). This model relates the internal electric field as a function of the injected current. It assumes that all the injected current is used to dilate the leader, and that the mass of each leader cylindrical segment remains constant as the expansion takes place.

Based on the Gallimberti's model, *Becerra* and *Cooray* (2006a) have recently introduced a self-consistent upward leader propagation model (SLIM). They have proposed a streamer approximation that assuming the area covered by the streamer region required for the simulation process is like a cone. The area accumulation between the potential of two consecutive leader segments is proportional to the streamer charge and

the proportional constant is a geometrical factor that connects the total corona charge with the area. They have also developed a stable leader initiation criterion that the critical charge (Q_{crit}) necessary to thermalize the first leader segment should be equal or larger than 1 μC. However, a recent laboratory result (*Wu et al*., 2013) has shown Q_{crit} is in the range of 0.2-0.3 μC with different stem-to-leader transition time (≈ 10 μs). Another long air gap discharge study also showed that the injected charge is proportional to the leader length with a linear fitting of Q/L = 29.9 μC/m (*Chen et al*., 2016). Nevertheless, their simulation results can match with the leader current of an altitude-triggered lightning experiment.

Different to the SLIM, Rizk (2009) has assumed the critical charge is not a constant but is proportional to the continuous leader inception voltage ($Q_{crit} \propto U$). To maintain the leader propagation, the electric field and the corona charge around the leader tip must also exceed a critical value.

Rizk has also derived a semi-empirical equation for the leader tip potential that is given by

$$U_{tip}^{(i)} = l_L^{(i)} E_\infty + v_L^{(i)} \theta E_\infty \ln\left(\frac{E_{str}}{E_\infty} - \frac{E_{str}-E_\infty}{E_\infty} e^{-\frac{t^{(i)}}{\theta}}\right), \qquad (2.1)$$

where $l_L^{(i)}$ is the leader length at each i^{th} segment, E_∞ is the final quasi-stationary leader gradient, θ is the leader time constant.

2.8.1 Some Details about the Model SLIM

Note that equations are extracted from (*Gallimberti et al*., 2002; *Becerra* and *Cooray* 2006a).

Relate the leader electric field directly to the injected current

$$a_{L_i}^2(t) = a_{L_i}^2(t-\Delta t) + \frac{(\gamma-1)\Delta Q(t-\Delta t)E_{L_i}(t)}{\pi\gamma p_0}, \qquad (2.2)$$

$$\Delta Q = K_Q \int_{l_L}^{l_s}\big(U_1(l) - U_2(l)\big)dl, \qquad (2.3)$$

where a_{L_i} is the leader radius, γ is the ratio of the specific heats, p_0 is the standard atmospheric pressure, E_{L_i} is the internal electric field, ΔQ is the charge inside the streamer zone, K_Q is the streamer geometrical factor, and the integral term is the difference between the geometrical potential distribution before and after the formation of the streamer zone from the leader tip (l_L) to the streamer front (l_s).

By conservation of mass, the molecules' density can be written as

$$\pi n(t)a_{L_i}^2(t) = \pi n(t-\Delta t)a_{L_i}^2(t-\Delta t). \qquad (2.4)$$

Using the hypothesis that E_L/n remains constant,

$$\frac{E_{L_i}(t+\Delta t)}{E_{L_i}(t)} = \frac{a_{L_i}^2(t)}{a_{L_i}^2(t+\Delta t)}. \qquad (2.5)$$

The leader speed is calculated as

$$v_L = \frac{2}{7kn\Delta T}\left(f_{ert} + f_v\left(\frac{\tau_L/\tau_{vt}}{1+\tau_L/\tau_{vt}}\right)\right)\int JEdz, \qquad (2.6)$$

where k is Boltzmann constant, n is the neutral particle density at the critical temperature, ΔT is the temperature difference between the critical temperature and the ambient temperature, f_{ert} is the fraction of the input energy transferred into electronic,

rotational and translational excitation, f_v is the fraction of the input energy used for vibrational excitation, τ_L is the leader transition time, τ_{vt} vibrational-translational relaxation time, J is the leader current density and E is the average electric field in the transit region.

The potential drop along the leader channel containing n segments is equal to $\Delta U_L(t) = \sum_{i=1}^{n} E_{L_i}(t) l_{L_i}$. The lengths of the following newly created leader segments are computed using the constant relation between leader current and speed:

$$I_L = v_L \lambda_L, \qquad (2.7)$$

where λ_L is the line charge density required to transform the streamer located in the active region in front of the already formed leader channel into a new leader segment.

2.8.2 Some Existing Upward Leader Speed's Equations

Bazelyan and *Razhansky* (2008) proposed that an upward leader's speed v_L, can be approximated as:

$$v_L \approx a\sqrt{\Delta U_{tip}}, \qquad (2.8)$$

where $a = 15\ \mathrm{ms^{-1}V^{-0.5}}$ and ΔU_{tip} is the potential difference between the leader tip and the ambient (the external field).

Different from equation (2.8), *Lalande* and *Mazur* (2012) have suggested the leader's speed is related to the leader potential drop, which is the driving force for of the leader progression:

$$v_L = v_0\left(1 - e^{\frac{-2\Delta U_t}{k}}\right), \qquad (2.9)$$

where ΔU_t is the potential drop ahead of the leader and v_0 a constant.

2.9 Recent Lightning Attachment Process Characteristics

Even though the lightning attachment process has been studied more than four decades, this is still poorly understood. Recently, a high-speed optical system named LAPOS (Lightning Attachment Process Observation System) has been used to observe the characteristics of lightning attachment process of natural lightning flashes (*Wang et al*. 2015). They found that a stronger lightning flash tends to initiate at a higher junction point. In another study, (*Tran et al*. 2014) have observed a new phenomenon that a poor conductive pre-return-stroke path named faintly luminous formation (FLF) is built up between the downward leader tip and the ground termination point before the first return stroke occurs. From this new phenomenon, *Tran* and *Rakov* (2015) have also introduced a new method to estimate the striking distance.

2.10 Modeling Lightning Attachment Process

Studying the lightning attachment process can help us to evaluate the transition between the leader stage and the return stroke stage of a lightning flash. As a first return stroke is always preceded by a downward leader, a leader model can be used as an initial channel condition for simulating the first return stroke (*Chen and Du,* 2009; *Cai et al*., 2017).

The first lightning attachment process model was introduced by *Eriksson* (1987). He has developed an improved 3-D Electrogeometric model, Collection Volume Method (CVM) and applied the concept of critical radius to estimate the striking distance. A few years later, *Dellera* and *Garbagnati* (1990) and *Rizk* (1994) proposed their own engineering models to simulate the lightning attachment process. Recently, the SLIM has also been applied to study the attachment process (*Cooray*, 2013).

The propagating speed ratio of the downward (V_D) and upward (V_U) leaders is believed to be the main parameter to evaluate the attachment process. While *Dellera* and *Garbagnati* (1990) assumed the speed ratio is varied between 1:1 and 4:1, *Rizk* (1994) and *Mazur* (2000) assumed the speed ratio is a constant. In comparison to observation, *Lu et al*. (2015) has recently shown the 2-D speed ratio between V_D and V_U is not a constant but decrease from 4.9 to 0.2.

2.11 Highly-time-resolved Observations of Leaders

Prof. Boys (1928) has invented a two-lens streak camera system to record the phases of a lightning discharge called Boys camera. The Boys camera has been used to capture most features of lightning flashes that take place below thunderclouds for 50 years.

Today, thanks to the invention of the high-speed video cameras, the features of lightning flashes can be obtained in very wide range of frame rate. Although the 1000 ips frame rate is capable of visualizing most of the phases of cloud-to-ground lightning, a higher frame rate is required for other lightning processes. For example, the observation of upward connecting leaders may require at least 10000 ips.

Most high-speed cameras contain a trigger system based on signal that detects a signal from other external sources such as the current or electric field sensor input. In fact, the field of view decreases as the recording speed is increased. One must consider the desired field of view and recording speed before selecting an appropriate lens. By using high-speed cameras, it is possible to register events related to each of the polarities of leader propagation. While a stable positive leader presents continuous propagation, a negative leader presents stepped propagation.

Nowadays, many high-speed cameras are GPS synchronized and provide time-stamped images with no frame-to-frame brightness persistence. The synchronization allows the correlation of each flash recorded with the ones detected by the lightning location system such as lightning mapping arrays and interferometers.

The Lightning Mapping Array (LMA) developed by researchers at the New Mexico Institute of Mining and Technology, is the most recent and most advanced very high frequency (VHF) time of arrival (TOA) system. VHF is defined as the frequency range of radio waves between 30 MHz and 300 MHz. Nowadays, LMA has become a major tool for both lightning research and operational applications. The idea of using the VHF technique for lightning location system was first suggested by *Oetzel* and *Pierce* (1969). The basic principle of the TOA location system can be found in *Cooray* (2014).

However, TOA techniques can only be applied to locate radiating isolated pulses. To locate the noise-like bursts of electromagnetic radiation correctly, an interferometric method is an alternative way for locating a source of VHF radiation emitted by lightning. The first VHF radio interferometry was designed by *Hayanga* and *Warwik* (1981) for lightning studies. The general principle of VHF interferometry is to measure the phase difference among different VHF pulses received by a set of antennas separated by a finite distance. Then the azimuth location of the lightning source can be estimated. A brief review of the VHF radio interferometry technique can be found in *Kawasaki* (2012).

2.11 Summary

In this chapter, a brief introduction of the corona space charge layer near the ground and the classification of upward lightning were presented. Then, some recent observation results of the lightning attachment process were reviewed. Further, the physical characteristics of both positive and negative leaders including some recent observations and theoretical modeling of upward leaders were described and reviewed. Finally, some optical observation and lightning location techniques were briefly reviewed.

Chapter 3

A Macroscopic Physical Model for Self-Initiated Upward Leaders

3.1 Introduction

This chapter introduces a macroscopic physical model for a self-initiated upward leader based on electrostatics rather than the thermos-hydrodynamics (*Gallimberti*, 1979), aiming at interpretation of leader initiation and propagation behaviors from the point of view of energy conservation. This model can simulate an upward leader initiated from a grounded object, such as a transmission tower or a windmill under thunderclouds. The overall approach seems to be similar to other existing models, but some critical assumptions are different. Specifically, by introducing a tri-zone leader channel structure, a set of equations describing the evolution of the charge, electric field and current, and the size of the leader channel are figured out based on electrostatics; an equation describing the propagation speed of a stable upward leader is derived based on energy conversation law; and a physical criterion for an upward leader inception and stable propagation is proposed and tested.

3.2 Upward Leader Modelling: The Inception Criteria and Conditions and the Propagation Properties

In this section, we aim to introduce a model to evaluate an overall upward leader process initiated from a tall grounded object in terms of the charge, current, electric field and conductivity along the leader channel in the basis of electrostatics. When the local electric field around the top of a tall grounded object is greater or equal to the breakdown strength of the air, an arcing process occurs and an upward leader is initiated there. The input electrical energy to the leader is determined by its current and conductance. The charge transfers hence the leader current highly depends on the ambient electric field profile established by charges in the thundercloud. Most of the input energy is dissipated in ways of air ionization, heating and radiation, as well as the leader channel expansion. In the following, we are going to define the leader channel structure and the electrostatic condition for each part of the channel structure, and then the leader initiation criterion and the leader evolution rule.

3.2.1 Tri-zone Leader Model

Although a leader channel structure is complicated, it can be simplified as three parts (*Rakov and Uman*, 2003; *Rakov*, 2016): the bright leader tip, the cold streamer zone ahead of the leader tip, and the hot conductive channel behind the leader tip. There is also a streamer-to-leader transition zone within the leader tip, converting a streamer into a leader segment. As the arcing process occurs in the leader tip, the leader keeps growing and extending forward. Based on such a thought, we propose a three-zone leader channel structure as shown in **Figure 3.1**, where R_L stands for the conductive leader core radius, R_T the streamer-leader transition zone radius, and R_C the corona streamer sheath radius. Inside the leader core, positive and negative particles can move freely and the radial

electric field is nearly zero; Inside the corona sheath, the electric field is assumed to be approximately the critical breakdown electric field, E_C; Inside the transition zone, the electric field is assumed to be brought up gradually from near zero to near E_C continuously; And outside the corona sheath, the electric field may exponentially reduce to E_A.

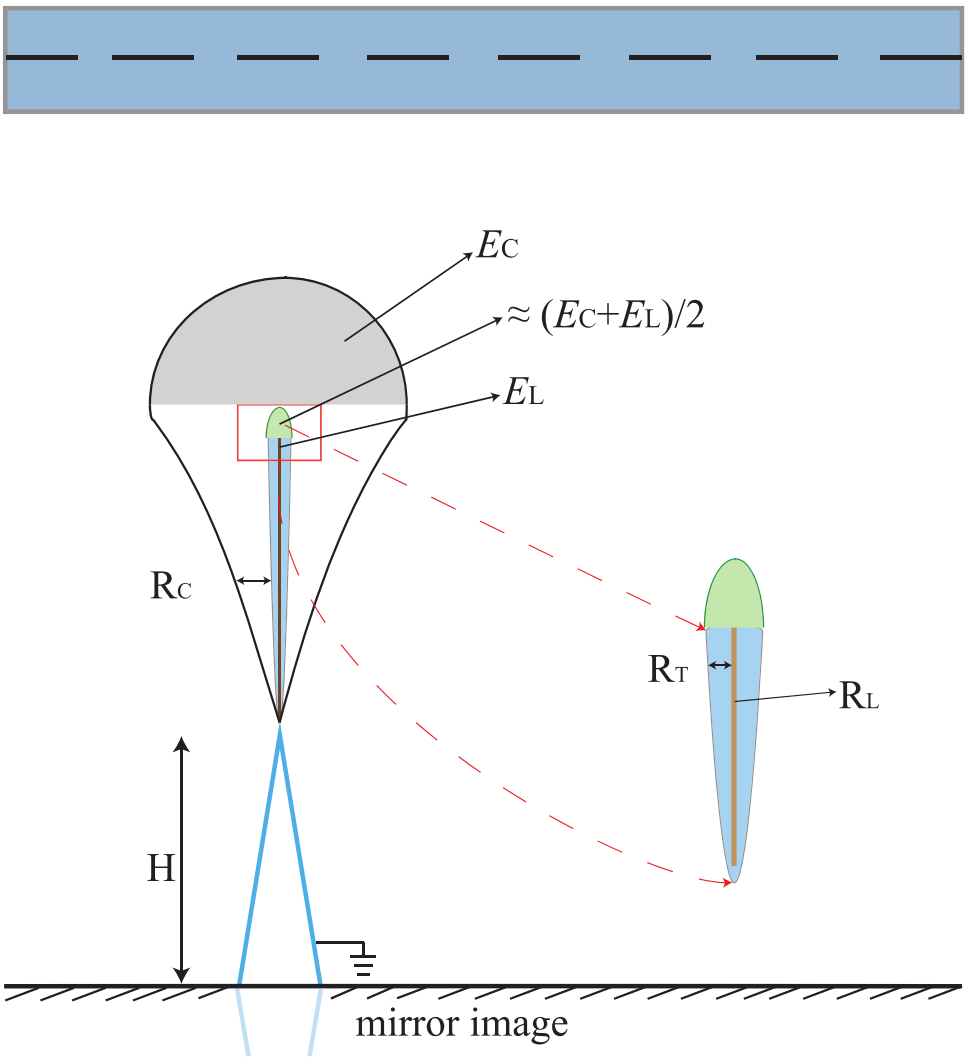

Figure 3.1. Sketch of a tri-zone upward leader structure induced on the metallic grounded structure (not to scale). The grey color in the figure represents the region of the streamer zone and green color the region of the leader tip. The double arrow symbol indicates the rough size of each zone.

3.2.2 Assumptions of concepts and parameters involved in the model

i. For simplicity, the upward leader is assumed to propagate along a straight line and it does not branch. The leader gets energy from E_A, which may include: i) the electric field due to the charges in the thundercloud, E_{cloud}, ii) that due to the corona space charge layer near the ground, E_{corona}, and iii) that due to the charge transfer by other nearby discharge, E_{other}. That is, $E_A = E_{cloud} + E_{corona} + E_{other}$.

ii. Although the thundercloud charge structure is complicated, many measurements show that the vertical E_A in each leader process under the cloud base is nearly constant (Stolzenburg *et al*. 2002, 2007). Hence, the charged cloud may be simplified as a conductive plane with a potential, φ_{cloud} (e.g. -60 MV), at a height, H (e.g. 3000 m), resulting in a constant E_{cloud} (e.g. -20 kV/m) between the cloud base and the ground, the electric field due to the corona space charge layer near the ground, E_{corona}, may be determined based on the observed space electric field profile versus height under a thundercloud, which will be discussed later in next section.

iii. The electric field change due to a nearby discharge such as a downward leader, E_{other}, could be either positive or negative and changing with time and space. If the resulted E_A is not stronger than the leader core longitudinal electric field, E_L, the leader will vanish. A similar phenomenon often occurs in unconnected upward leaders triggered by a downward leader (*Warner*, 2012), which will be discussed in detail in Chapter 5.

iv. E_A may be enhanced or distorted surrounding the lightning rod or a high-rise structure. When the enhanced electric field around the tip of the rod or the high-rise structure reaches E_C in a certain space range (the critical corona radius: R_{crit}), a leader is supposed to initiate there. In another word, a successful leader initiation and stable propagation requires the local electric field around the leader head reaches E_C in a range larger than R_{crit}, which will be discussed in detail in next section.

v. We suppose the lightning channel is cylindrically symmetric and extends either upward or downward in straight. Therefore, the symmetric cylindrical coordinate system (altitude *z*, radius *r*) is adopted, with the ground set as z = 0 and the lightning channel centred along the *z* axis.

3.2.3 Physics of the Model

3.2.3.1 Leader Inception Condition

The extend of local electric field enhancement depends on the height and shape of a grounded structure (*Alessandro*, 2003). Suppose there is a lightning rod or an equivalent sharp object on the top of this structure, and the leader inception needs the local enhanced electric field around the rod tip (E_{tip}) larger than the critical electric field (E_C) in in a range larger than the critical corona radius (R_{crit}) there.

This is:

$$E_{tip} \approx \frac{\int_0^{Hr} E_A(z)dz}{2r} > E_C, \qquad \text{and} \qquad \frac{\int_0^{Hr} E_A(z)dz}{E_C} > R_{crit}, \quad (3.1)$$

where, H_r is the rod tip height above the ground, r the lightning rod tip radius, and E_A(z) the ambient electric field profile without taking account the influence of the structure.

Observations show that the electric field on the ground due to the corona space charge layer, E_{ground}, with pointed objects under the thunderstorm is usually not larger than a certain value (*Willett et al*., 1999; *Biagi et al*., 2011), but might be very high over the sea (*Toland and Vonnegut*, 1977). If this space charge layer is included, in the case E_{cloud} is larger than E_{ground}, the vertical ambient field profile can be simply expressed as (*Biagi et al*., 2011):

$$E_A(z) = E_{cloud} + (E_{ground} - E_{cloud})e^{-z/L_c}, \qquad (3.2)$$

where L_c is a characteristic decay height of the corona space charge layer.

Besides, the critical electric field varies with the air density and humidity, hence the height above sea level (*Chen et al*, 2013a), which can be written as:

$$E_C(z) = E_{C0}e^{-\frac{z}{H_0}}, \qquad (3.3)$$

where E_{C0} (about -750 kV/m and 500 kV/m for negative and positive polarity, respectively) is the critical electric field at sea level, H_0 is a characteristic height of about 8400 m, and z is the height above sea.

When the local enhanced electric field is larger than E_C, electrons in the air not only drift opposite to the field, but also ionize the gas and generate an avalanche concurrently. High-energy photons emitted from the primary avalanche provide photoionization in the vicinity, which initiates secondary avalanches. As the local electric field due to electrons in the avalanche keeps comparable to E_C, the avalanche-to-streamer transition may occur and a weakly ionized plasma channel is created, called streamer. As the air temperature increases, a leader channel is created and grows along the path prepared by the preceding

streamers. If the local electric field around the leader tip keeps comparable to E_C, a new streamer zone will grow in front of the leader tip, preparing the path for further propagation. If E_A decreases suddenly and significantly or even reverses its polarity, making the local electric field less than E_C, the streamer and leader will vanish.

3.2.3.2 Leader Channel Electric Field and Charge Profile

While the radial electric field in the leader core (R_L) is assumed to be zero, the radial electric field in the leader transition zone (R_T) is assumed to increase gradually from nearly zero to E_c. The radial electric field inside the corona sheath (R_C) is assumed to be equal to E_c. Outside the sheath, this radial electric field may gradually decrease to E_A. As a result, the leader channel radial electric field profile, as shown in **Figure 3.2** is given by:

$$E(r) = \begin{cases} 0, & r < R_L \\ \frac{E_c(r-R_L)}{R_T-R_L}, & R_T \geq r \geq R_L \\ E_c, & R_C \geq r \geq R_T \\ \frac{E_c R_c}{r}, & r \geq R_C \end{cases}. \tag{3.4}$$

The volume charge density versus leader channel radius, as shown **Figure 3.3**, is given by:

$$\rho(r) = \frac{\varepsilon_0}{r}\frac{\partial[rE(r)]}{\partial r} = \begin{cases} 0, & r < R_L \\ \frac{\varepsilon_0 E_c\left(2-\frac{R_L)}{r}\right)}{R_T-R_L}, & R_T \geq r \geq R_L \\ \frac{\varepsilon_0 E_c}{r}, & R_C \geq r \geq R_T \\ 0, & r > R_C \end{cases}. \tag{3.5}$$

The line charge density versus leader channel radius, as shown in **Figure 3.4**, is given by:

$$\lambda(r) = 2\pi\varepsilon_0 \int_{R_L}^{r} r'\rho(r')dr' = 2\pi\varepsilon_0 \begin{cases} 0, & r < R_L \\ \frac{E_c(r^2-R_L r)}{R_T-R_L}, & R_T \geq r \geq R_L \\ E_c r, & R_C \geq r \geq R_T \\ E_c R_C, & r \geq R_C \end{cases}. \tag{3.6}$$

For the volume charge density shown in **Figure 3.3**,

$$\rho_1 = \frac{\varepsilon_0 E_c}{R_T - R_L}, \qquad \rho_2 = \frac{\varepsilon_0 E_c}{R_T - R_L}\left(2 - \frac{R_L}{R_T}\right), \qquad \rho_3 = \frac{\varepsilon_0 E_c}{R_T}. \tag{3.7}$$

When $R_T >> R_L$, then $\rho_1 \approx \rho_3 = 0.5\rho_2$.

We further hypothesize that the maximum volume charge density (ρ_2) is capped to a limit, then the evolution of the leader transition zone (R_T) is related to that of the leader core radius (R_L) ($\rho_{2_i} = \rho_{2_{i+1}}$). To introduce this tri-zone model, we can select a more physical size of leader channel for charge calculation, which will be discussed later. As most of the charges are deposited inside R_C which may be up to several meters larger, the thin-wire approximation should be modified when it is adopted for the leader channel for charge simulations.

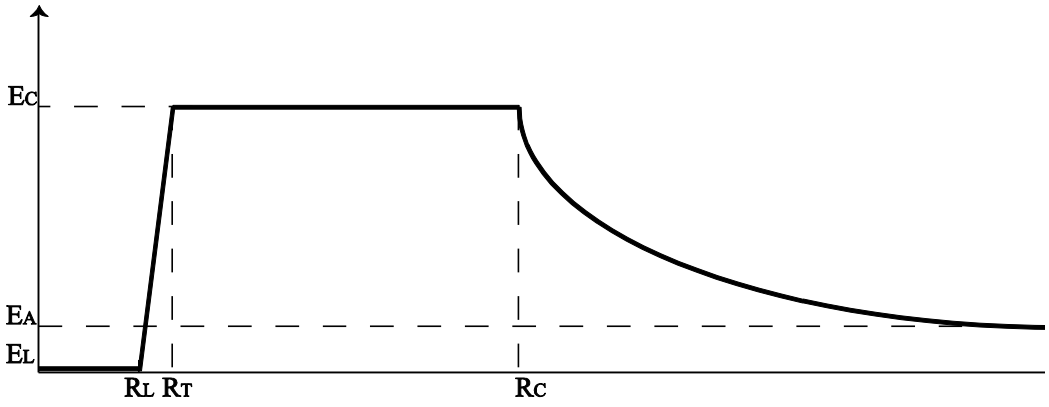

Figure 3.2. The radial electric field profile in a tri-zone leader channel (not to scale).

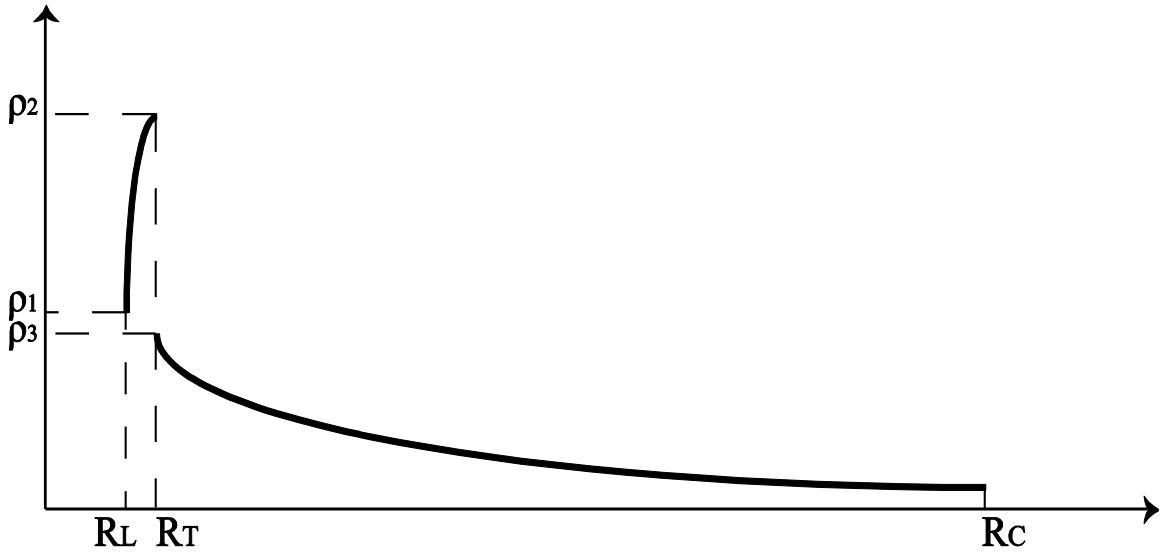

Figure 3.3. The radial volume charge density profile in a tri-zone leader channel (not to scale).

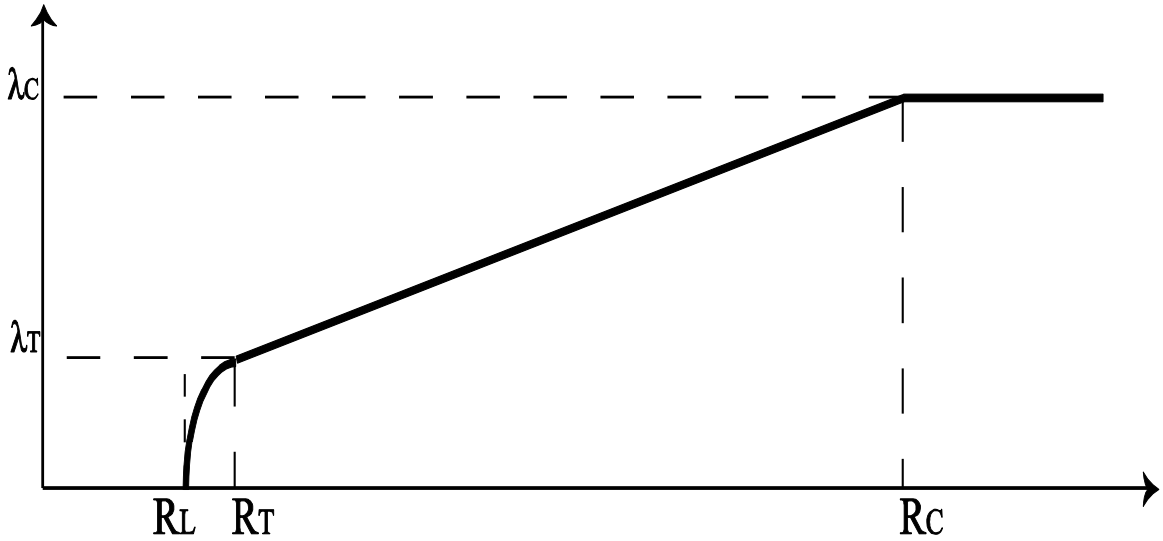

Figure 3.4. The radial line charge density profile in a tri-zone leader channel (not to scale).

3.2.3.3 Leader Head Energy Conservation

The dynamic variation of the streamer-leader transition zone can be described by a plasma physics model in the hydrodynamic scale (*Riousset et al., 2010; da Silva and Pasko, 2013*). To evaluate the overall average propagation speed of the leader in an inertial frame, we assume the leader head is a hemispherical ionized gas cloud, which consists of a transition zone shell and a corona sheath shell (streamer zone) with the leader core tip as the center of the hemisphere. Inside the transition zone shell, the electric field increases gradually from the electric field in the leader core (E_L) to that in the corona sheath (E_c). From the conservation of energy and mass for a short moment inside the leader transition zone (dl), we can write:

$$d\left(\frac{1}{2}M{v_{tip}}^2\right) = \left\{Q_T\left[\left(\frac{E_C+E_L}{2} - E_{Dr}\right)\right] - \frac{(P_C+P_R+P_V+P_D)}{v}\right\} dl, \qquad (3.8)$$

where the left-hand term is the total kinetic energy gained in the leader tip transition zone and the right-hand term is the electrical energy injected and energy losses due to heat conduction (P_C) and radiation (P_R), vibration (P_V), and air resistance and friction (P_D). And $E_{Dr} \approx 5.58 \times 10^{-18} \frac{n_e \ln \Lambda}{T_e}$, is the Dreicer field represents the dynamical friction, $ln\Lambda$ the Coulomb logarithm, T_e the electron temperature, Q_T the total charges and M the total mass of the leader tip transition zone. For thermal electron-electron collisions with $T_e < 10$ eV, $ln\Lambda$ can be well approximated by $\ln \Lambda \approx 23 - 0.5 \ln n_e + 1.5 \ln T_e$, where n_e is expressed in units of cm^{-3} and T_e is expressed in eV.

In the leader head, electron temperature is much higher than the ion and neutral temperatures. This is because charged particles are much heavier than electrons, the external power source (Electric Potential) heats the electrons more strongly than ion and neutral particles.

3.2.3.4 Leader Propagation Speed

We assume that inside the leader tip transition zone the heating process is isobaric ($\Delta(V^2/T) = 0$) and the total mass is conserved ($\Delta M = 0$). Based on conservation of energy, the gain in kinetic energy of total mass is equal to the difference of the total injected electrical charge energy and the energy losses due to heating, vibration and friction, as shown by equation (3.8). If the radius of corona sheath shell (streamer zone) around the leader tip keeps larger than R_{crit}, the leader tip transition zone shell gets more and more kinetic energy as it moves forward within the corona sheath shell by converting a part of the corona sheath shell into a part of conductive leader core step by step, making the leader core extended. As such, the leader tip moving speed is equivalent to the transition zone moving speed, which can be derived from equation (3.8) as:

$$v_{tip} = \sqrt{\int \frac{F[\eta(E_c+E_L)-2E_{Dr}]}{\mathcal{M}} dl}, \qquad (3.9)$$

where, η is coefficient representing the losses of heating, vibration and friction, F = 96485.3365 C/mol is the Faraday constant, and $\mathcal{M} = \sum_i (w_i \mathcal{M}_i)$ is the effective molar mass among ions composition, within the leader tip transition zone.

For the molar mass M, a gas dynamic modeling result (*Aleksandrov and Bazelyan*, 1999) show that, on rainy days, for a positive streamer under standard conditions, $H_3O^+(H_2O)_3$ ions dominate at ground altitudes with a relatively high recombination rate with electrons. Note: $Q_T/\mathcal{M} = eN/\mathcal{M} = F/\mathcal{M}$.

The leader propagation speed is then given by:

$$v_L = \frac{v_{tip}}{1+\tau_d/\tau_a}, \qquad (3.10)$$

where, τ_a and τ_d are the three-body attachment time scale and the delay time for a new leader segment to cross the streamer-to-leader transition zone, respectively. τ_d is also defined as the time needed to heat the leader tip channel up to 5000 K.

Recently, some gas dynamic modeling results (*Riousset et al*., 2010; *da Silva and Pasko*, 2013) have shown that $\tau_d \propto \rho^{-2}$, where ρ is the ambient air density. In the present model, referring to equation (3.10), we assume that:

$$\tau_d = \tau_{d0} e^{\frac{2z}{H_0}}. \tag{3.11}$$

3.2.3.5 Leader Corona Sheath and Conductive Core

From equation (3.6), the leader corona sheath radius (R_C) can simply be related to the leader line charge density (λ_L) by (*Xu and Chen,* 2013):

$$R_c(z) = \frac{\lambda_L(z)}{2\pi\varepsilon_0 E_c(z)}. \tag{3.12}$$

Arc discharge experiments show that the power per unit length of an ideal leader keeping in thermal balance is a constant:

$$E_L I_L = \frac{{I_L}^2}{\pi {R_L}^2 \sigma_L} = \frac{{I_L}^2}{g_L} = b, \tag{3.13}$$

where E_L is the average leader core longitudinal electric field, I_L the leader current, σ_L the conductivity and g_L the conductance of the leader core per unit length, and b a constant of 30 kWm^{-1} (*Bazelyan and Raizer,* 2000).

To maintain a leader in thermal equilibrium, when the leader current increases, both the leader core radius and the leader conductivity should also increase. Even though the leader core radius and the leader conductivity evolution are complex functions with time, we simply assume the heating process inside the leader core obeys the ideal gas law (*pV/T*

= constant), and the mass is conserved, $\Delta M = 0$, where $V = \pi R_L^2$ the volume, p the pressure and T the temperature of per unit length of the leader core. In addition, the temperature is related to the leader core conductivity by $\sigma \propto e^{-\frac{C}{T}} \approx \sigma \propto T$ (C is a constant) (*Bazelyan and Raizer*, 2000). Further hypothesizing p and V increase in an equal weighting with T, then $\sigma_L \propto V^2 \propto {R_L}^4$ and $g_L \propto {R_L}^6$.

Hence, the evolution of R_L and σ_L versus g_L can be expressed as:

$$R_L(t) = R_L(0)\left(\frac{g_L(t)}{g_L(0)}\right)^{1/6}, t > 0, \tag{3.14}$$

where $g_L(0)$ and $R_L(0)$ are the initial leader conductance per meter and the initial leader core radius, respectively. And,

$$\sigma_L(t) = \sigma_L(0)\left(\frac{g_L(t)}{g_L(0)}\right)^{2/3}, t > 0, \tag{3.15}$$

where $\sigma_L(0) = \frac{g_L(0)}{\pi R_L(0)^2}$ is the initial leader core conductivity.

3.2.3.6 Leader Line Charge Density

The mirror image and charge simulation method (CSM) are applied to calculate the line charge density of the leader channel. CSM is one of the most developed and adopted computational techniques for solving electrostatic problems. The leader development can be divided into many small developing steps ($j = 1, \ldots, N_T$). At each developing step, the leader core is supposed to extend forward a uniform space length Δl at the leader speed at that moment v_{Lj}, corresponding to a time interval of $\Delta t_j = \Delta l / v_{Lj}$. Thus, at any moment j, the whole leader channel will include three subsections: a grounded tall object (e.g. a lightning rod) with a height of H_r, a leader channel consisting of a thin conductive core channel surrounded by a thick corona sheath with a length of H_{Lj}, and a hemispheric

streamer zone ahead of the leader core tip with a length/radius of H_{sj}. The lightning rod is assumed to be thin wire with a radius r_{rod}. The leader channel contains a length of $H_{Lj} = j\Delta l$, a spatial-temporal dependent corona sheath radius of $R_{Cj-1}(z)$, and a time-dependent longitudinal electric field of E_{Lj-1} in its core. The hemispheric streamer zone is supposed to have a length and radius that is equal to the corona sheath radius at the leader tip (z_{tip}), i.e. $H_{sj} = R_{Cj-1}(z_{tip})$, and a radial/longitudinal electric field equal to the critical electric field $E_C(z)$ there. Since the E_{Lj} and $R_{Cj}(z)$ at the present step j are unknown, we will take the E_{Lj-1} and $R_{Cj-1}(z)$ got at the previous step $j-1$ to solve the leader channel charge distributions λ_{Lij} at the present step. The solution of λ_{Lij} is then used to update the E_{Lj} and $R_{Cj}(z)$ as described in next section.

The schematic diagram for the CSM for an upward leader channel is shown in **Figure 3.5**. With the assumption in the above paragraph, at any step j ($j=1, \ldots, N_T$), the whole channel consists of the lightning rod, the leader channel and the streamer zone, can be divided into N_j small segments in an equal interval of Δl. The potential difference between the channel centre (along the z axis) and the ambient at a segment z_k ($k = 1, \ldots, N_j$) is then related to the channel line charge densities λ_{Lij} ($i =1, \ldots, N_j$) at other segments by following matrix:

$$\sum_{i=1}^{N_j}(\alpha_{ki} - \alpha'_{ki})\lambda_{Lij} = 4\pi\varepsilon_0[\varphi_A(z_k) - \sum_{i=1}^{N_j} E_{Li}(z_i)\Delta l], \tag{3.16}$$

where

$$\alpha_{ki} = \frac{1}{{r_i}^2}\begin{bmatrix} (z_{i2} - z_k)\left(\sqrt{(z_{i2} - z_k)^2 + {r_i}^2} - |z_{i2} - z_k|\right) \\ -(z_{i1} - z_k)\left(\sqrt{(z_{i1} - z_k)^2 + {r_i}^2} - |z_{i1} - z_k|\right) \\ +{r_i}^2 \log\frac{z_{i2} - z_k + \sqrt{(z_{i2} - z_k)^2 + {r_i}^2}}{z_{i1} - z_k + \sqrt{(z_{i1} - z_k)^2 + {r_i}^2}} \end{bmatrix},$$

$$\alpha'_{ki} = \frac{1}{r_i^2}\begin{bmatrix} (z_{i2}+z_k)\left(\sqrt{(z_{i2}+z_k)^2+r_i^2}-|z_{i2}+z_k|\right) \\ -(z_{i1}+z_k)\left(\sqrt{(z_{i1}+z_k)^2+r_i^2}-|z_{i1}+z_k|\right) \\ +r_i^2\log\frac{z_{i2}+z_k+\sqrt{(z_{i2}+z_k)^2+r_i^2}}{z_{i1}+z_k+\sqrt{(z_{i1}+z_k)^2+r_i^2}} \end{bmatrix},$$

and

$$E_{Li} = \frac{I_{Lj-1}}{g_{rod}}, \quad r_i = r_{rod},\ for\ i = 1\ to\ N_r, lightning\ rod.$$

$$E_{Li} = \frac{b}{I_{Lj-1}}, \quad r_i = R_{Cj-1}(z_i),\ for\ i = N_r+1\ to\ N_r+j, leader.$$

$$E_{Li} = E_C(z_i),\ r_i = \sqrt{{H_{sj}}^2 - \left(z_i - z_{N_r+j}\right)^2},\ for\ i = N_r + j + 1\ to\ N_j, streamer.$$

$$H_{sj} = R_{Cj-1}\left(z_{N_r+j}\right), \quad N_{sj} = int\left(\frac{H_{sj}}{\Delta l}\right).$$

$$N_r = int(H_r/\Delta l), \quad N_j = N_r + j + N_{sj}.$$

Where, g_{rod} is the conductance per meter of the lightning rod, r_{rod} = 10 mm is the radius of the lightning rod. The α_{ki} and α'_{ki} are the charge and image charge potential coefficients respectively, which are adopted from *Chen et al.* (2013a). The λ_{Lij} is the line charge density of the i^{th} segment at step j, which is to be solved out. The z_{i2} and z_{i1} are the coordinates of the two ends of the i^{th} segment, and $\sum_{i=1}^{N_j} E_{Li}(z_i)\Delta l$ the leader core potential and $\varphi_A(z_k) = \int_0^{z_k} E_A(z)dz$ the ambient potential for the element z_k.

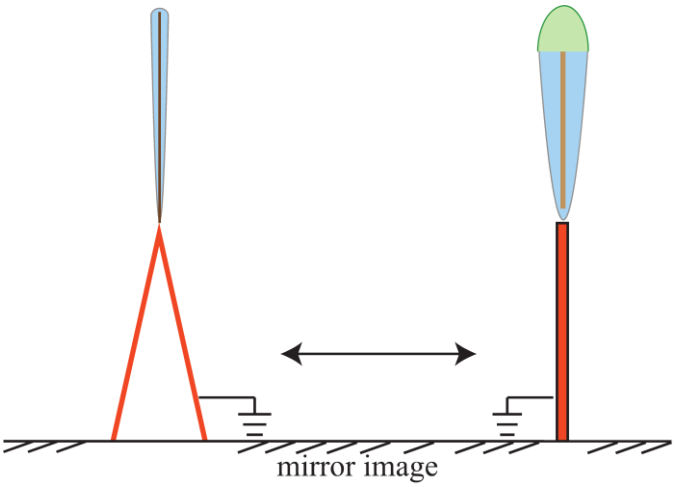

(a)

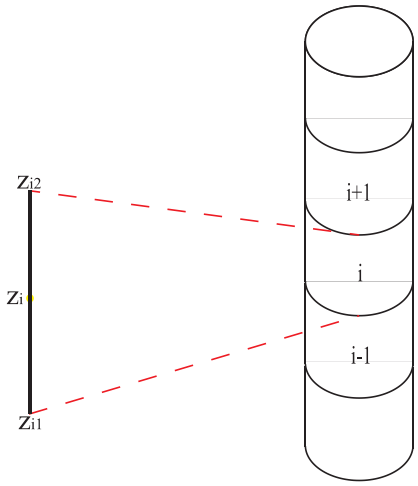

(b)

Figure 3.5. For modelling leader charge distribution with CSM: (a) The leader channel is equivalent to a cylindrically symmetric corona sheath surrounding a thin conductive core with the corona sheath radius varies with time and height; (b) The channel is divided into many small segments each with an equal length.

3.2.3.7 Leader Evolution

Based on the line charge density got from equation (3.16) for all the whole channel z_i (i =1 to N_j) and leader speed got from equation (3.10) for the developing step j (j=1,...,N_T), the evolution of leader core current, electrical field, conductance, leader core and corona sheath (hence the transition zone and streamer zone) radii, and core conductivity behind the leader tip at step j can then be updated iteratively as:

$$I_{Lj} = \lambda_{tipj} v_{Lj} = g_{Lj} E_{Lj}, where\ i = N_r + j\ \ is\ the\ leaer\ core\ tip, \quad (3.17a)$$

$$g_{Lj} = {I_{Lj}}^2 / b, \quad (3.17b)$$

$$E_{Lj} = b / I_{Lj}, \quad (3.17c)$$

$$R_{Cj}(z_i) = \frac{\lambda_{Lij}}{2\pi\varepsilon_0 E_C(z_i)}, i\ =\ N_r + 1 \text{ to } N_r + j, \quad (3.17d)$$

$$R_{Lj} = (\frac{g_{Lj}}{g_{L_0)}})^{\frac{1}{6}} R_{L_0}, \quad (3.17e)$$

$$\sigma_{Lj} = (\frac{g_{Lj}}{g_{L_0)}})^{\frac{2}{3}} \sigma_{L_0}, \quad (3.17f)$$

The radius of transition zone R_{Tj} can then be updated according to the core radius R_{Lj} via Eq. (3.7), if ρ_2 keeps a constant determined by R_{T0} and R_{L0} values. The time interval at step j is linked to the space step by $\Delta t_j = \Delta l / v_{Lj}$. As the leader stopping criterion, when $E_{Lj} \geq E_B(z_{tip})$ around the leader tip, the leader will stop propagating and the leader's current cutoff will begin (*Mazur* and *Ruhnke*, 2014). In other words, the leader survival condition is

$$E_{Lj} < E_B(z_{tip})\ \text{ or }\ I_{Lj} > b/E_B(z_{tip}) \text{ or } \lambda_{tip,j} > b/(E_B(z_{tip}) v_{Lj}). \quad (3.18)$$

3.2.3.8 Critical Corona Size and Charge for a Steady Leader Initiation

When the leader is just initiated ($t = 0$), $E_C >> E_L$ and E_{Dr}, the leader initial speed (v_{L0}) in relation to the initial corona length (l_0) can be approximated from equations (3.9-3.10) as:

$$v_{L_0} \approx \sqrt{\frac{F\eta E_C l_0}{\mathcal{M}}} / (1 + \frac{\tau_d}{\tau_a}). \tag{3.19}$$

It is noted that equation (3.20) can be further approximated as equation (2.8) by setting $a = \sqrt{\frac{F\eta}{\mathcal{M}}}/(1 + \tau_d/\tau_a)$ and $\Delta U_{tip} = E_C l_0$. This means that equations (3.9-3.10) are similar to the empirical equation (2.8) for a short air gap discharge in lab.

In addition, both field observations and lab experiments have showed that the minimum leader speed is not less than 10^4 m/s (*Bazelyan and Raizer*, 2000; *Wang et al*, 2016). If we set v_{crit} = 10^4 m/s as the critical (least) leader starting speed, with the parameters showed in **Table 3.1**, the critical initial corona length at ground level can then be estimated from equation (3.20) as:

$$l_0 = 0.105 \text{ m} \approx R_{crit}.$$

Here, we further assume the critical corona sheath radius of leader head is equal to the critical initial coronal length at ground level (R_{crit}), the critical initial corona line charge density at ground level (λ_{crit}) hence the critical charge at ground level (Q_{crit}) can then be estimated from equation (3.12) as:

$$\lambda_{crit} = 2\pi\varepsilon_0 E_C R_{crit} = 2.91\ \mu\text{C/m}, \quad Q_{crit} = \lambda_{crit} R_{crit} = 0.305\ \mu\text{C}. \tag{3.20}$$

The Q_{crit} at ground level is about 0.3 μC, which is the upper bound reported in *Wu et al*. (2013). Since E_C and τ_d are a function of the height above ground, R_{crit} and λ_{crit} hence

Q_{crit} are height dependent. **Figure 3.6** illustrates the R_{crit} and Q_{crit} versus initiation height for UPL with the parameters showed in **Table 3.1**. For example, the values of R_{crit} and Q_{crit} of a 500-m high grounded object are about 0.14 m and 0.5 μC respectively.

Furthermore, the minimum (critical) height (H_b) for a grounded object to initiate a steady upward leader under a given E_A profile can be estimated from equation (3.1) as:

$$(\int_0^{H_b} E_A dz)/E_C(z) \geq R_{crit}. \qquad (3.21)$$

H_b is defined as the minimum height, where the value of E_L starts to be a little bit smaller than E_A, a stable upward leader can be self-triggered at the top of the grounded object, propagating towards the charged cloud.

Shown in **Figure 3.7** is a flowchart to illustrate the computing algorithm of the model.

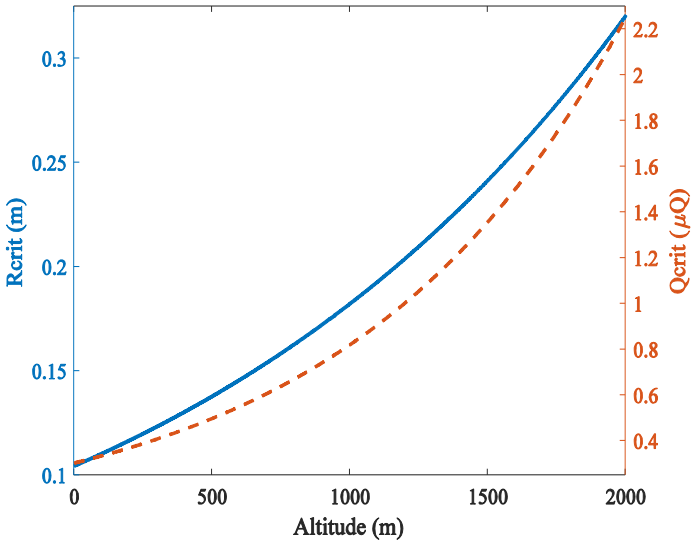

Figure 3.6. The critical corona length (R_{crit}) and charge (Q_{crit}) versus the initiation height for a successful UPL initiation.

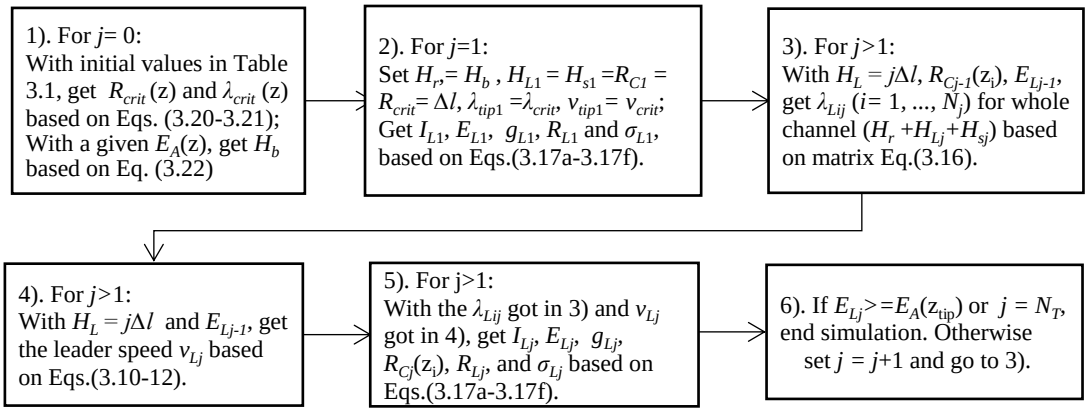

Figure 3.7. Flowchart of the leader modelling algorithm at each space/time step j.

TABLE 3.1. Initial parameters for the upward positive leader simulation.

Symbol	Description and Value	
M	Effective molar mass	73 g/mol
H	Simulation height	3000 m
E_{cloud}	Electric field due to the cloud charge	-30 to -10 kV/m
E_{C0}	Breakdown electric field at ground level	+500 kV/m
$g_L(0)$	Initial conductance per unit length	0.1 mS/m
$R_L(0)$	Initial leader core radius	1 mm (Gallimberti, 1979)
T_e	Electron temperature	20000 K (Gallimberti, 1979)
$T_L(0)$	Initial leader temperature	4000 K (Bazelyan et al., 2000)
τ_{a0}	Three-body attachment time at ground level	0.1 μs (Bazelyan et al., 2000)
τ_{d0}	Delay time at ground level	1 μs (Bazelyan et al. 2007)
η	Heat and vibrational energy lost	0.175
l_0	Minimum leader length at ground level	0.105 m

3.3 Summary

In this chapter, we have introduced a macroscopic self-triggered upward leader model based on electrostatics. The main points of this model can be summarized as following:

i. A three-zone leader channel structure;

ii. The first leader segment will be created if the local electric field enhancement on the top of a grounded object reaches the critical breakdown electric field in a certain range;

iii. The leader speed is subjected to the conservation of energy and mass inside the streamer-to-leader transitional zone around the leader head;

iv. A steady leader requires the leader initial speed (energy) should be larger than the minimum (critical) speed observed for leaders in both field and lab experiments ($\approx 10^4$ ms^{-1}), which corresponding to a critical corona sheath radius hence a critical corona sheath charge ahead of the leader;

v. The leader charge distribution is calculated by the CSM;

vi. The leader ceases when its channel electric field is larger than the E_A.

Simulation results and the model's application will be discussed in next chapter.

Chapter 4

Simulation Results of Self-triggered UPL Model and Its Validation to Observations

4.1 Introduction

This chapter presents the simulation results of the self-triggered upward leader model described in the previous chapter. This model has been applied to investigate an UPL self-initiated from the top of a tall grounded object with or without the consideration of the effect of corona space charge layer near the ground. The minimum height of a grounded object for self-initiation of an upward leader under different initial conditions are estimated and discussed. This model is further testes with two set of experiment data and very promising results are obtained. Modeling results can help us to design an effective lightning protection system for tall grounded objects.

4.2 Modeling Results for UPL in General

With the parameter values in **Table 3.1**, the model introduced in the previous chapter is applied to study the UPL inception under a thundercloud with and without a space charge layer being considered.

Two cases are studied:

Case 1. A self-initiated UPL from a grounded object under constant E_A.

Case 2. A self-initiated UPL from a grounded object under different E_{cloud} with E_{corona} being considered as E_{ground} = -3 kV/m and L_c = 250 m.

In *Case* 1, the E_A is assumed as a constant. This may occur over sea, like an operational offshore wind turbine (*Malinga* and *Niedzwecki*, 2015). With equations (3.20-22), the minimum self-initiation height (H_b) under different E_{cloud} is evaluated, as shown in **Figure 4.1** and **Table 4.1**. The figure and table also include the leader stabilization electric field versus the triggering height estimated with other models (*Rizk,* 1994; *Lalande et al.*, 1996; *Becerra* and *Cooray*, 2006b). The results from all these models shown that the triggering height (H_b) is inversely proportional to the ambient electric field (E_{cloud}). As it is very hard for E_{cloud} to be above -30 kV/m according to observations, we just show the values up to -30 kV/m for comparisons. Our modelling results well match with that of *Lalande et al.* (1996), but have a higher triggering height than others for the same electric field value. This difference is partially due to that we take +500 kV/m as the critical value for the positive breakdown while others take +450kV/m. Meanwhile it also means that the criterion (E_{crit} and v_{crit}, hence the R_{crit} and Q_{crit}) for self-triggered UPL in the present model is stricter than that in other models. Nevertheless, our results well match the usual

assumption that a structure with a height less than 100 m is struck only by downward lightning.

In *Case* 2, we have modified our model with a changing E_A by taking account a corona space charge layer near the ground. E_A(z) is based on equation (3.2). By choosing an adequate L_c, equation (3.2) can match well with observed space electric field profiles in literature. Taking E_{ground} = -3 kV/m and L_c = 250 m, H_b versus E_{cloud} is also evaluated, as shown in **Figure 4.1** and **Table 4.1**. As can be seen from both the figure and the table, the minimum self-initiation height becomes larger when the space charge layer is considered. For example, for E_{cloud} = -15 kV/m the minimum initiation height is only 469 m in *Case* 1 but becomes 601 m in *Case* 2. This is because E_A produced by the thundercloud is distorted by the corona space charge layer near the ground. In general, the minimum self-initiation height strongly depends on the actual E_{cloud} and E_{ground} values, and the results here are comparable to those in *Aleksandrov et al.* (2005).

TABLE 4.1. The minimum UPL self-triggering height versus cloud electric field (E_{cloud}) for *Case* 1 and *Case* 2 from the present model, and the triggering height versus leader stabilization field from other models.

E_{cloud} *or* $E_{stab.}$ (kV/m)	*Case* 1 (H_b, m)	*Case* 2 (H_b, m)	Rizk[1] (H_b, m)	Lalande[2] (H_b, m)	Becerra[3] (H_b, m)
-10	1191.5	1259.5	151.7	1337.5	330.6 m
-15	469.0	601.0	99.8	712.5	214.3 m
-20	252.5	410.0	73.9	290.7	157.1 m
-25	157.5	319.0	58.4	176.7	120.4 m
-30	108.0	265.0	48.0	124.0	83.7 m

[1] Rizk (1994); [2] Lalande et al. (1996); [3]Becerra and Cooray (2006b)

Simulation results of the current, speed, channel size, and conductivity of an UPL propagating from its initiation height (H_b) up to 3000 m high under different E_{cloud}, for both *Case* 1 and *Case* 2 are summarized in **Table 4.2**. These results show that while the initial leader velocity is fixed at 10^4 m/s, initial values of all the leader current, line charge density and corona sheath size are inversely proportional to the ambient electric field (E_{cloud} and E_{ground}) but proportional to the initiation height (H_b). The final values of all these parameters are dependent on the leader propagation length (3000 m – H_b). Simulation results also show that UPLs self-initiated at different heights exhibit different speed evolution. Such a phenomenon has already been mentioned in a recent observation in Japan (*Wang and Takagi*, 2012). Other observations (*Kito et al*., 1985; *Asakawa et al*., 1997; *Wada et al*., 2003) have reported the speed of UPLs ranging from 6×10^4 to 1.4×10^6 m/s. Our simulation results (1.0×10^4 to 7.3×10^5 m/s) are within this range.

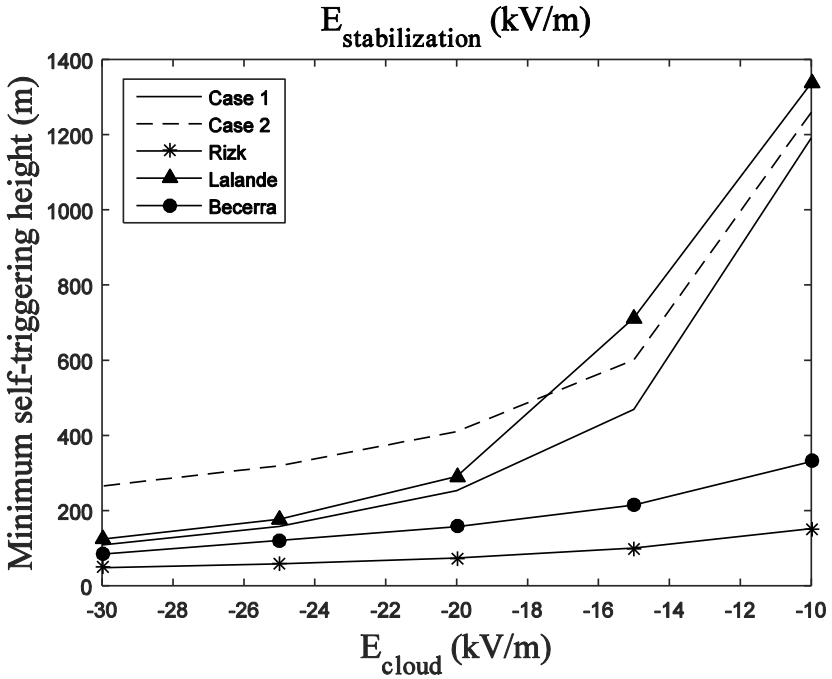

Figure 4.1. The minimum UPL self-triggering height versus cloud electric field (E_{cloud}) with (dashed-line) and without (solid-line) a space charge layer from the present model, and the leader stabilization field versus triggering height from other models (also see **Table 4.1**).

In following, we select the case of E_{cloud} = -20 kV/m as an example to illustrate the details of the evolution of each of the leader parameters.

Shown in **Figures 4.2a** and **4.3a** are evolutions of the leader charge density and the corona sheath radius respectively, for E_{cloud} = -20 kV/m for *Case* 1. As seen from the figures, while the leader is growing, more and more electric charges accumulate along the channel. This is because the potential difference between the leader core and the environment keeps increasing as the leader extends upward. The figures also show that at the beginning stage (t_0) the leader tip charge density is higher than that at stage t_1, while that at stage t_1 is smaller than that at stage t_2 and so on. As the grounded object is supposed to be a good conductor and the voltage drop along it is very small, the leader channel has limited conductance and voltage drop alone it is relatively big. The corresponding evolutions of the leader charge density and the corona sheath radius for E_{cloud} = -20 kV/m for *Case* 2 are shown in **Figures 4.2b** and **4.3b**, respectively. Their evolution trends are very similar to those for *Case* 1, except the difference in the initiation height due to the effect of the corona space charge layer.

Because of the similarity between *Case* 1 and *Case* 2, in following we just present detailed results for E_{cloud} = -20 kV/m for *Case* 2, for the leader speed (**Figure 4.4**), leader current and longitudinal electric field (**Figure 4.5**), leader core conductance and conductivity (**Figure 4.6**), leader core and transition zone radius (**Figure 4.7**), and the leader core temperature (**Figure 4.8**), for discussions.

Shown in **Figure 4.4** is the leader speed evolution verse time and height. It shows the leader keeps accelerating from the 10 km/s self-initiation speed to about 700 km/s when it reaches a height of about 2 km and decelerates to about 670 km/s when it reaches the cloud base. This is because the delay time (τ_d) for a new leader segment to cross the

streamer-to-leader transition region increases with the propagating height. In other words, the required streamer-leader heating time is longer at a lower pressure than that at a higher pressure. The feature of evolution of leader speed for other cases is similar to this case.

The leader current (**Figure 4.5**) keeps increasing from the initial value of about 1.8 A up to about 308 A, while the longitudinal electric field keeps decreasing from the initial value of about -16.7 kV/m down to about -100 V/m, as the leader propagates from the initiation height of 410 m up to 3000 m high.

The conductance (**Figure 4.6**) and radius (**Figure 4.7**) of the leader core increase from their initial values of 10 mS per meter and 1 mm up to about 3.1 S per meter, 5.6 mm, as the leader propagates from the initiation height of 410 m up to 3000 m high. **Figure 4.7** also shows that while the leader core radius (R_L) keeps expanding, the leader streamer-core transition zone radius (R_T = 10~12 mm) does not change too much.

Table 4.2. Summary of simulation results for UPL traveling from its triggering height (H_b) to 3000 m high with different cloud electric field (E_{cloud}) for both Case 1 and Case 2.

Cloud Field (E_{cloud})	Leader Current I_L (A)	
	Case 1 (H_b)	Case 2 (H_b)
-10 kV/m	3.0 – 130.1	3.0 – 116.7
-15 kV/m	2.0 – 248.8	2.2 – 223.6
-20 kV/m	1.5 – 340.5	1.8 – 307.6
-25 kV/m	1.2 – 421.9	1.6 – 387.0
-30 kV/m	1.0 – 494.8	1.5 – 463.8
Cloud Field (E_{cloud})	Leader longitudinal E-field E_L (V/m)	
	Case 1 (H_b)	Case 2 (H_b)
-10 kV/m	- 9999 – -231	-9953 – -257
-15 kV/m	-14999 – -121	-13914 – -134
-20 kV/m	-19981 – -88	-16695 – -98
-25 kV/m	-24999 – -71	-18842 – -78
-30 kV/m	-29956 – -61	-20613 – -65
Cloud Field (E_{cloud})	Leader tip line charge density λ_L (μC/m)	
	Case 1 (H_b)	Case 2 (H_b)
-10 kV/m	147.4 – 247.9	144.1 – 236.7
-15 kV/m	80.7 – 368.1	78.6 – 345.6
-20 kV/m	59.9 – 494.9	62.4 – 459.1
-25 kV/m	48.8 – 624.9	54.5 – 574.0
-30 kV/m	41.5 – 757.3	49.6 – 690.0
Cloud Field (E_{cloud})	Leader tip corona sheath radius R_C (m)	
	Case 1 (H_b)	Case 2 (H_b)
-10 kV/m	0.203 – 12.74	0.211 – 12.16
-15 kV/m	0.136 – 18.91	0.146 – 17.76
-20 kV/m	0.120 – 25.43	0.131 – 23.59
-25 kV/m	0.114 – 32.11	0.125 – 29.49
-30 kV/m	0.111 – 38.91	0.121 – 35.45
Cloud Field (E_{cloud})	Leader propagation speed v_L (10^4 m/s)	
	Case 1 (H_b)	Case 2 (H_b)
-10 kV/m	1.0 – 52.5	1.0 – 49.3
-15 kV/m	1.0 – 69.5	1.0 – 66.1
-20 kV/m	1.0 – 72.9	1.0 – 69.8
-25 kV/m	1.0 – 73.3	1.0 – 71.3
-30 kV/m	1.0 – 72.7	1.0 – 71.9

Cloud Field (E_{cloud})	Leader conductance g_L (mS/m)	
	Case 1 (H_b)	Case 2 (H_b)
-10 kV/m	10 – 564	10 – 454
-15 kV/m	10 – 2063	10 – 1667
-20 kV/m	10 – 3864	10 – 3154
-25 kV/m	10 – 5934	10 – 4992
-30 kV/m	10 – 8160	10 – 7169
Cloud Field (E_{cloud})	Leader core radius R_L (mm)	
	Case 1 (H_b)	Case 2 (H_b)
-10 kV/m	1 – 3.5	1 – 4.1
-15 kV/m	1 – 5.0	1 – 5.1
-20 kV/m	1 – 6.1	1 – 5.6
-25 kV/m	1 – 7.1	1 – 6.1
-30 kV/m	1 – 7.9	1 – 6.5

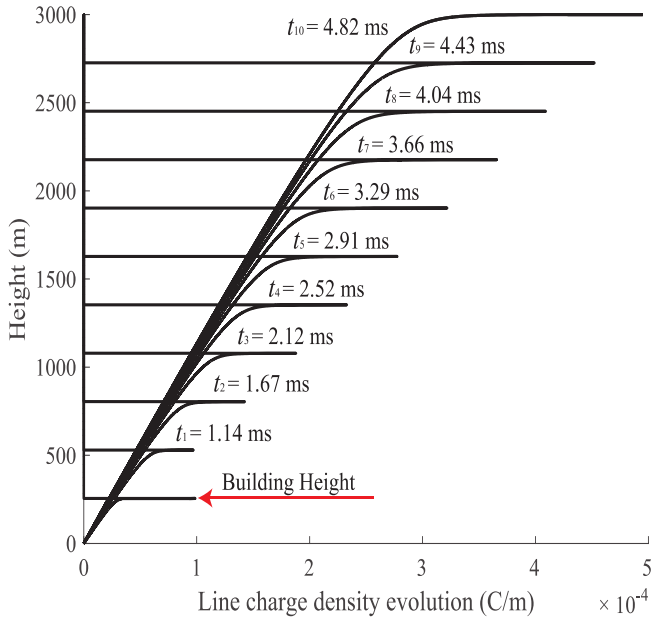

(a)

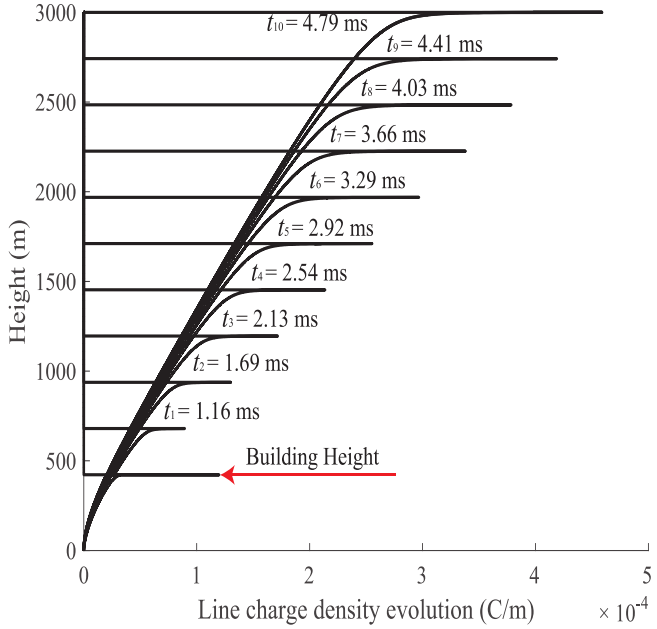

(b)

Figure 4.2. Spatial and temporal evolution of the leader line charge density (λ_L). (a) for *Case* 1 for E_{cloud} = -20 kV/m, (b) for *Case* 2 for E_{cloud} = -20 kV/m and E_{ground} = -3 kV/m.

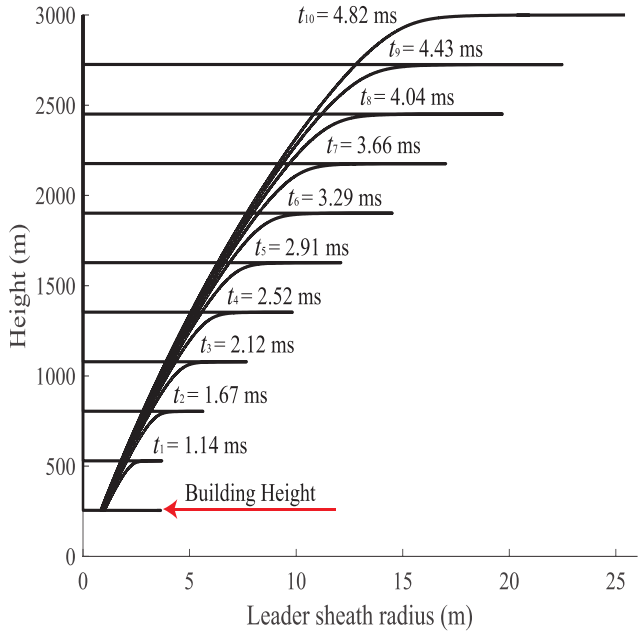

(a)

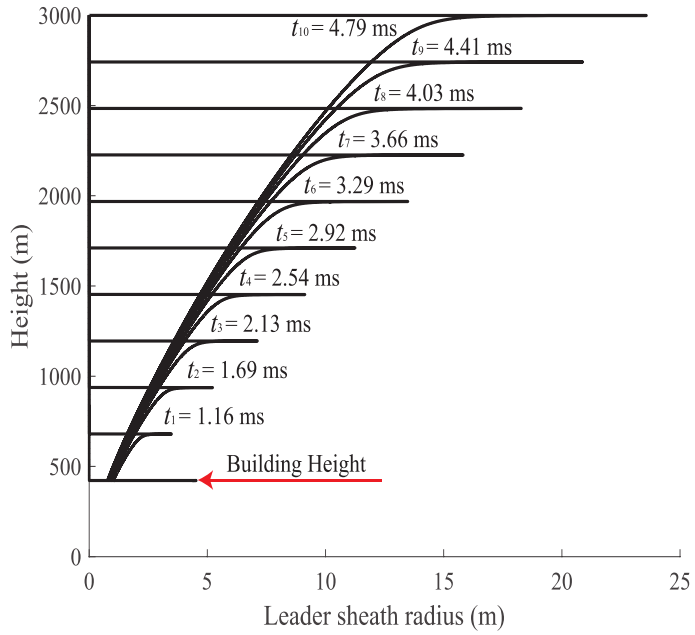

(b)

Figure 4.3. Spatial and temporal evolution of the leader corona sheath radius (R_C). (a) for *Case* 1 for E_{cloud} = -20 kV/m, (b) or *Case* 2 for E_{cloud} = -20 kV/m and E_{ground} = -3 kV/m.

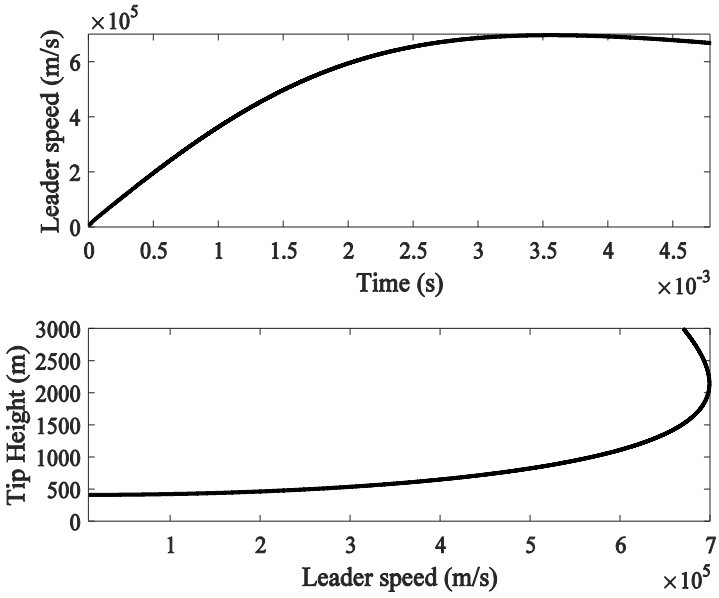

Figure 4.4. Leader speed (v_L) versus propagation time (top) and that versus leader tip height (below), for *Case* 2 for E_{cloud} = -20 kV/m and E_{ground} = -3 kV/m.

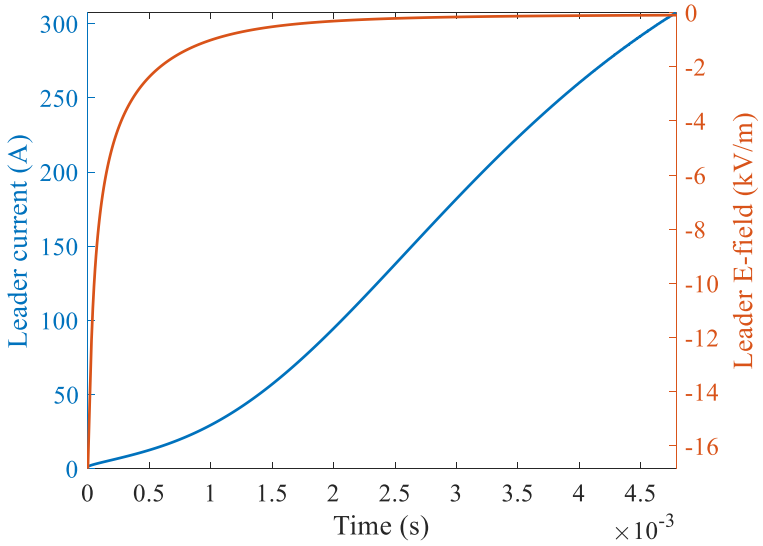

Figure 4.5. Leader current (I_L in blue) and leader electric field (E_L in brown) versus propagation time for *Case* 2 for E_{cloud} = -20 kV/m and E_{ground} = -3 kV/m.

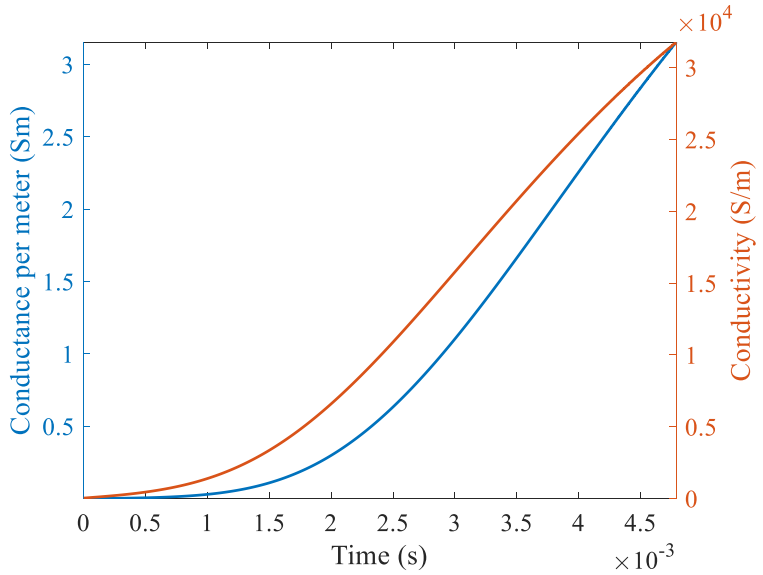

Figure 4.6. Leader channel conductance per meter length (g_L in blue) and conductivity (σ_L in brown) versus leader propagation time, for *Case* 2 for E_{cloud} = -20 kV/m and E_{ground} = -3 kV/m.

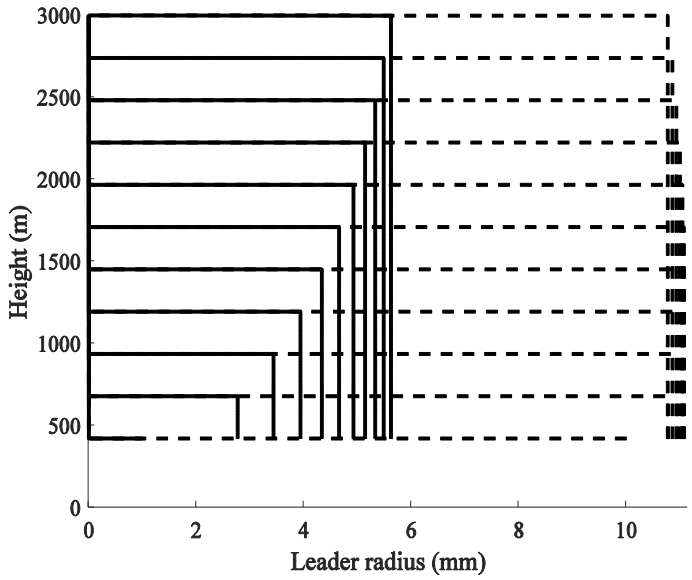

Figure 4.7. Leader core radius (R_L solid line) and transition zone radius (R_T dash line) versus leader tip height for *Case* 2 for E_{cloud} = -20 kV/m and E_{ground} = -3 kV/m.

4.3 Model Validation

4.3.1 Leader Current and Speed

Experiment 1: Recently, *Chen et al*., (2013b) have reported an UPL in a rocket-triggered lightning discharge. It is the initial UPL in a classical triggered lightning discharge succeeded on 2 August 2005 during the SHATLE program (*Qie et al*., 2009). Measurements of the leader included the channel base currents and high-speed camera images. The initiation height of the leader was estimated at 266.4m above the ground, and the final height viewed by the camera was about 602.4m above the ground.

To simulate the UPL in *Experiment* 1, following initial model parameters are adopted: E_{cloud} = -31.75 kV/m with E_{ground} = -3 kV and L_c = 250 m, R_{L0} = 1 mm, η = 0.046. Other initial parameters are the same to **Table 3.1**. It should be mentioned that the model initial parameters like η and $\mathcal{M}$ might be case dependent. They can be fine-tuned to better match with observations when necessary. Comparisons of the leader current and leader speed between the model-based and experiment-based estimation are shown in **Figure 4.8** and **Figure 4.9**, respectively. Other leader parameters like the leader line charge density, leader core electric field and conductance, leader core and corona sheath radius are also modeled, which are not shown here for conciseness. The modelled leader currents and speeds match well with the experiment data, indicating that the model well describes the relationships

between the ambient electric field (E_A), leader initiation height (H_b) and propagation speed (v_L), and leader current (I_L) and charge deposit (λ_L).

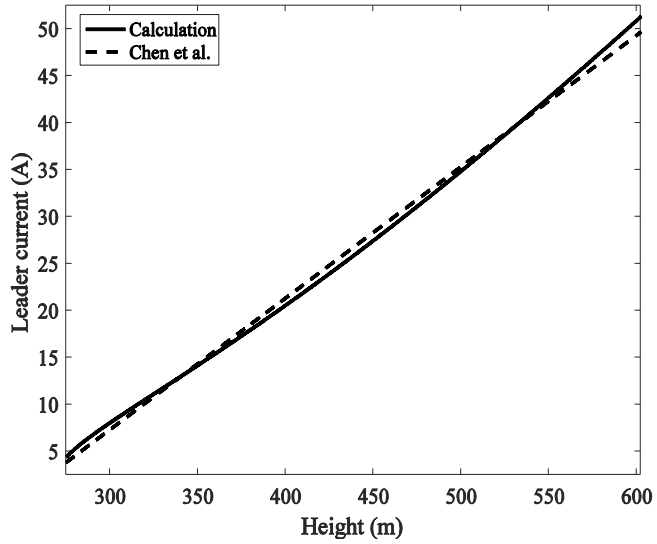

Figure 4.8. Comparison of the leader current evolution between modeled (solid-line) and observed (dashed-line) results for the UPL reported in *Chen et al.* (2013b).

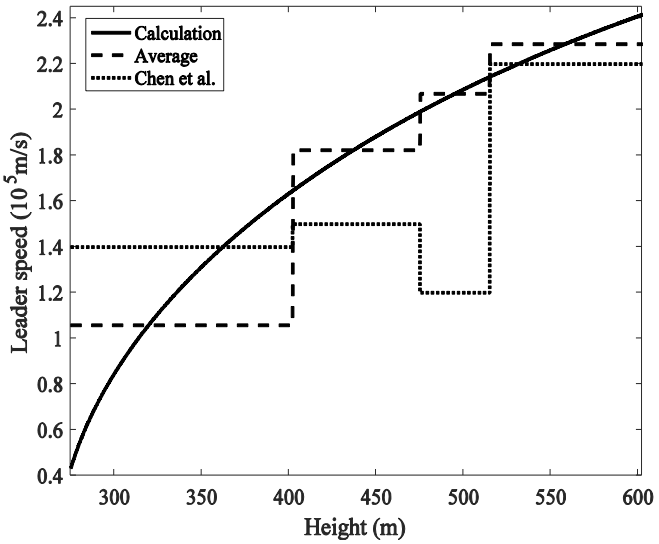

Figure 4.9. Comparison of the leader speed evolution between modeled (solid-line) and observed (short-dashed-line) results for the UPL reported in *Chen et al.* (2013b). Long-dashed-line is the model-based averaged speed for different channel segments in accordance with the observed result.

4.3.2 Leader Core Radius Expansion

Experiment 2: To test our proposed leader core expansion equation, we have compared the simulation results to a positive point-to-plane air gap discharge reported in *Zhou et al*. (2015). The discharge was made for a 0.93 m point-plane gap under a positive IEC standard switching impulse voltage (250/2500 μs) with the amplitude of about 350 kV. In the experiment, a 4-m optical path Mach-Zehnder interferometer was set up to observe the gas density variation and radial expansion of leader discharges. Theoretically, a leader discharge is an isobaric process (*Riousset et al., 2010; da Silva and Pasko, 2013*). By the ideal gas law, a high temperature leader can reduce the gas density and change the refractive index of the air. Their results show that the estimated diameter of the leader channels is expanded from 1.5 mm to 3.5 mm and the average expansion speed is about 6.7 m/s.

To simulate the point-to-plane gap discharge in *Experiment* 2, a uniform E_A of -350 kV/m is assumed to match with that in the experiment. A 1-m high metallic rod with a radius 1 cm placed on a grounded plane and a plane-to-plane gap of 6.5 m is assumed so that the modeled leader propagation time can match with the leader heating time period in the experiment. Since the major purpose is to evaluate the evolution trend of leader core radius as describe by equation (3.17d) of the model with the experiment, three different initial values (d_0 = 1 mm, 1.5 mm and 2 mm) of leader core diameter are tried with the model. Other initial parameters are the same to those in **Table 3.1.** Shown in **Figure 4.10** is a comparison of the leader core diameter between the modeled and measured results for the experiment. As can be seen from the figure, the evolution trend of modeled leader core diameter with d_0 = 1.5 mm is well consistent with that of the experiment, indicating that the equation (3.17d) well describes the leader core evolution trend. Other parameters such

as the leader current, leader speed, leader charge and core conductance are also modeled but not shown here for conciseness.

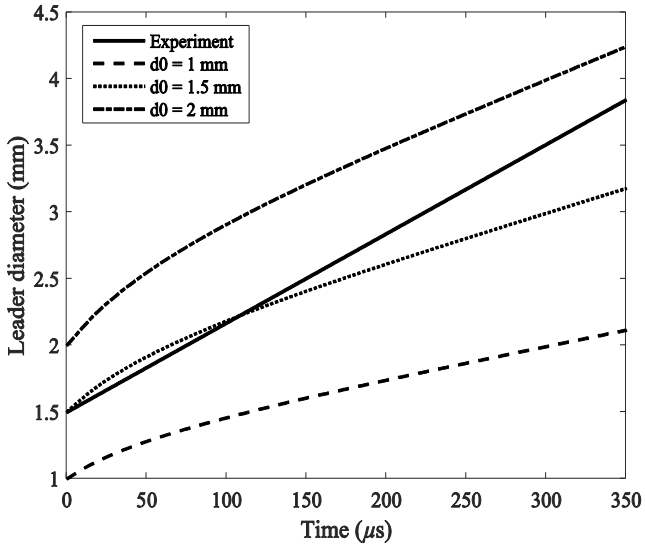

Figure 4.10. Evolution trends of the leader core diameter modeled with different initial values (1, 1.5 and 2 mm respectively) and that measured in lab, for the point-to-plane gap discharge reported in *Zhou et al.* (2015).

4.4 Summary

In this chapter, we have presented our simulation results and model validation for the UPL model. This model has been applied to study UPL inceptions from tall structures under different thunderclouds with and without the corona space charge layer effect near the ground. Based on the leader initiation criterion described in the model, the critical corona sheath length and corona charge as a function of the leader initiation height and the minimum leader initiation height as a function of the thundercloud condition for UPL are estimated and discussed. Simulate results such as the evolutions of the speed, charge distribution, current, electric field, conductance and conductivity, channel size and temperature of UPL under different thundercloud conditions are also obtained and discussed. Our model has further been adjusted based on two set of experiment data. Last but not least, we should validate our model to more observations, so that we can select a correct mass percent of water in a hydrate.

Chapter 5

Modeling of Leader Attachment Process and Its Validation to Observations

5.1 Introduction

In this chapter, the macroscopic lightning leader model described in chapter 3 is used to study upward positive leaders triggered by a downward negative leader on some grounded objects. For this, a spatiotemporal electric field due to the descending leader is derived and applied to check whether the enhanced electric field strength is large enough to initiate upward leaders. A similar spatial and temporal electric field expression for the upward leaders is also introduced. Calculation results are agreed with the Rizk's assumption. Two case studies of lightning attachment of upward leaders reported in two recent optical observation experiments are evaluated. Based on the measured distance and average speed of the downward leader, upward connecting leader (UCL), and unconnected upward leader (UUL), our model can also estimate the surrounding vertical ambient electric field profile of that observation site and leaders' parameters, such as leader line charge density, leader current, and leader core longitude electric field.

5.2 Downward Leader Model

To simulate a DNL, the physical model described in chapter 3 is modified by adding some extra assumptions. Details are shown as follows:

i. Shown in **Figure 5.1**, the preliminary breakdown process inside a thundercloud (*Tran and Rakov*, 2016) is not within the scope. The cloud base is simply assumed as a conductive plane with a potential, φ_{cloud} (e.g. -30 MV), at a height, H (e.g. 3000 m), and the DNL is assumed to initiate from the cloud base, propagates along a straight line and does not separate into branches. It is also not influenced by the structures at ground level.

ii. Although we do not know the exact distance between the source of the thundercloud charge to the ground, we assume the total charges inside the cloud generate a nearly constant cloud electric field below the cloud base, E_{cloud}, (e.g. -10 kV/m), within a few milliseconds (*Stolzenburg et al*., 2002, 2007; *Chen et al*., 2013a). We assume there is a leader seed induced from the cloud base (*Xu and Chen*, 2013) and this leader seed is assumed to be 500 m long. In addition, a macroscopic average step length is introduced to describe the extension of leader within a step.

iii. Like the chapter 3, the leader corona sheath radius (R_C) can simply be related to the leader line charge density (λ_L) by

$$R_c(z) = \frac{\lambda_L(z)}{2\pi\varepsilon_0 E_c(z)}. \qquad (5.1)$$

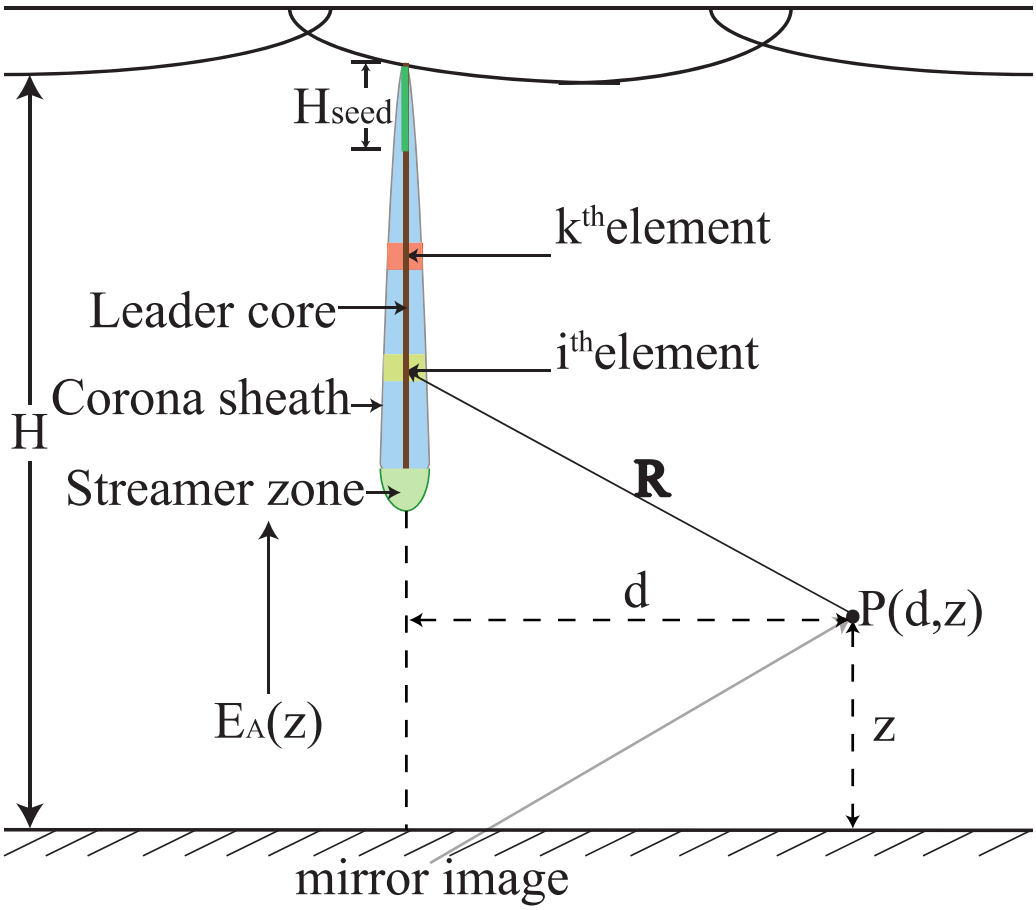

Figure 5.1. Diagram for the calculation of CSM and electrostatic fields from a DNL at point P (not drawn to scale).

iv. Similar to the UPL, because of the negative differential resistance characteristic of a leader channel, the longitudinal electrical field (potential gradient) in the channel can be simply related to the channel current by

$$E_L I_L = b, \qquad (5.2)$$

where b is a constant = 30 kW/m (*Bazelyan and Raizer*, 2000).

v. The mirror image and CSM are applied to calculate the line charge density along the DNL channel. As shown in **Figure 5.1**, the channel is assumed to be a tri-zone structure as in chapter 3, propagates towards the flat ground. Like the UPL described in chapter 3, the DNL development can be divided into many small developing steps (j = 1, …, N_T). At each developing step, the leader core is supposed to extend forward a uniform space length Δl at the leader speed at that moment v_{Lj}, corresponding to a time interval of $\Delta t_j = \Delta l / v_{Lj}$. Thus, at any moment, the whole leader channel consists of three subsections: the leader seed with a length of H_{seed} = 500 m, the descending leader channel with a length of $H_{Lj} = j\Delta l$, and the hemispheric streamer zone ahead of the leader tip with a length/radius equal to the corona sheath radius at leader core tip as $H_{sj} = R_{Cj\text{-}1}(z_{tip})$, which can be divided into N_j small segments in an interval of Δl. The potential difference between the channel centre and the ambient at a segment z_k (k = 1, …, N_j, count from the cloud base down to the leader head) is then related to the channel line charge densities λ_{Lij} (i =1, …, N_j) at other segments by following matrix:

$$\sum_{i=1}^{N_j}(\alpha_{ki} - \alpha_{k'i})\,\lambda_{Lij} = 4\pi\varepsilon_0 \sum_{i=1}^{N_j}\big(E_A(z_i) - E_L(z_i)\big)\Delta l, \tag{5.3a}$$

where

$$\alpha_{ki} = \frac{1}{{r_i}^2}\begin{bmatrix} (z_{i2} - z_k)\left(\sqrt{(z_{i2} - z_k)^2 + {r_i}^2} - |z_{i2} - z_k|\right) \\ -(z_{i1} - z_k)\left(\sqrt{(z_{i1} - z_k)^2 + {r_i}^2} - |z_{i1} - z_k|\right) \\ +{r_i}^2 \log\frac{z_{i2} - z_k + \sqrt{(z_{i2} - z_k)^2 + {r_i}^2}}{z_{i1} - z_k + \sqrt{(z_{i1} - z_k)^2 + {r_i}^2}} \end{bmatrix},$$

$$\alpha'_{ki} = \frac{1}{{r_i}^2}\begin{bmatrix} (z_{i2} + z_k)\left(\sqrt{(z_{i2} + z_k)^2 + {r_i}^2} - |z_{i2} + z_k|\right) \\ -(z_{i1} + z_k)\left(\sqrt{(z_{i1} + z_k)^2 + {r_i}^2} - |z_{i1} + z_k|\right) \\ +{r_i}^2 \log\frac{z_{i2} + z_k + \sqrt{(z_{i2} + z_k)^2 + {r_i}^2}}{z_{i1} + z_k + \sqrt{(z_{i1} + z_k)^2 + {r_i}^2}} \end{bmatrix},$$

and

$E_L = \frac{b}{I_{Lj-1}}, \quad r_i = R_{Cj-1}(z_i),\ for\ i = 1\ to\ N_{seed} + j, leader\ seed\ and\ leader.$

$E_{Li} = E_C(z_i),\ r_i = \sqrt{{H_{sj}}^2 - \left(z_i - z_{N_{seed}+j}\right)^2},\ for\ i = N_{seed} + j +$

$1\ to\ N_j, streamer.$

$H_{sj} = R_{Cj-1}\left(z_{N_{seed}+j}\right),\ N_{sj} = int\left(\frac{H_{sj}}{\Delta l}\right).$

$N_{seed} = int(H_{seed}/\Delta l), \quad N_j = N_{seed} + j + N_{sj}.$

Where, α_{ki} and α'_{ki} are the charge and image charge potential coefficients respectively, which are adopted from *Chen et al*. (2013a). The z_{i2} and z_{i1} are the coordinates of the two ends of the i^{th} segment, and

$$E_A(z) = E_{cloud} + \left(E_{ground} - E_{cloud}\right)e^{-\frac{z}{L_c}}, \qquad (5.3b)$$

vi. The leader propagation speed from Eq. (3.9) and (3.10) is simplified as:

$$v_L = \frac{\sqrt{\int_0^L \left\{\frac{F}{\mathcal{M}}[\eta(E_C+E_L)]\right\}dl}}{1+\tau_{d0}/\tau_{a0}e^{2z/H_0}}, \qquad (5.4)$$

where η represents the heat and vibrational energy lost, F is the Faraday constant, $\mathcal{M} = \sum_i(w_i\mathcal{M}_i)$is the effective molar mass among ions composition, E_C is the breakdown electric field, E_L is the leader core longitudinal electric field, τ_{a0} is the three-body attachment time scale at ground level, τ_{d0} is delay time for a new leader segment to cross the stream-to-leader transition region at ground level, z is the longitudinal direction above sea, and H_0 is a constant of 8400 m.

Here, we assume the delay time constant of a DNL is longer than the UPL described in Chapter 3. This is because in each fixed propagation length, Δl, we assume positive leaders move faster than negative leaders. However, this initial parameter might be case dependent.

vii. While a negative streamer is propagating in humid air, the most abundant negative ions produced by the electron attachment process for different time scales are shown in **Table 5.1**.

viii. Based on the line charge density got from Equation (5.3) and the leader speed got from Equation (5.4) for the developing step *j*, the leader current, longitudinal electric field, conductance, leader core and corona sheath (hence the transition zone and streamer zone) radii, and core conductivity behind the leader tip at step *j* can then be updated iteratively as:

$$I_{Lj} = \lambda_{tipj} v_{Lj} = g_{Lj} E_{Lj}, where\ i = N_{seed} + j\ \ is\ the\ leader\ core\ tip, \quad (5.5a)$$

$$g_{Lj} = {I_{Lj}}^2/b, \text{ and } E_{Lj} = b/I_{Lj}, \quad (5.5b)$$

$$R_{Cj}(z_i) = \frac{\lambda_{Lij}}{2\pi\varepsilon_0 E_C(z_i)}, i\ =\ N_{seed} + 1 \text{ to } N_{seed} + j, \quad (5.5c)$$

$$R_{Lj} = (\frac{g_{Lj}}{g_{L_0)}})^{\frac{1}{6}} R_{L_0}, \text{ and } \sigma_{Lj} = (\frac{g_{Lj}}{g_{L_0)}})^{\frac{2}{3}} \sigma_{L_0}, \quad (5.5d)$$

The radius of transition zone R_{Tj} can then be updated according to the core radius R_{Lj} described in Chapter 3. When $E_{Lj} \geq E_B(z_{tip})$ around the leader tip, the leader will stop moving.

TABLE 5.1. The most abundant negative ions among different time scales (*POPOV*, 2010).

Time scales	0.1 *m*s > *t* ≥ 0.1 μs	0.01 s > *t* ≥ 0.1 *m*s	*t* ≥ 0.01 s
Ions	$O_2^-(H_2O)_N$	$CO_3^-(H_2O)_N$	$NO_3^-(H_2O)_N$
Relative molar mass	31.99886 + 18.015324N	60.00907 + 18.01528N	62.00501 + 18.01528N

5.3 Simulation Results of a DNL model

By above modified physical model and considering the corona space charge layer near the ground surface, a DNL from the thunderstorm cloud base propagates towards the flat ground is simulated. Then, the electric field due to the DNL as a function of space and time is evaluated, so the other-triggered upward positive leader initiation process can be simulated. **Table 5.2** lists the initial values and **Figures 5.2** – **5.8** are simulation results of the DNL.

Figures 5.2 – 5.5 show the line charge density (λ_L) and corona sheath radius (R_C) evolution of the DNL, with and without the corona space charge layer with an opposite polarity near the ground. Because of this space charge layer near the ground, when the leader tip is 400 m above the ground, more negative charges are accumulated along the channel. Under the thin-wire approximation (Chapter 3), the overall charge distribution along the channel is smaller than other existing models. However, the values of electric field due to the DNL seem to be more reasonable, which will be discussed in the next section.

Starting in this paragraph, we only consider the case that the space charge layer near the ground is included. **Figures 5.6** – **5.8** illustrate the evolution of other physical properties of the DNL, for E_{cloud} = -10 kV/m and E_{ground} = -3 kV/m. Simulation results show an increase in speed as the DNL approached the ground. The leader speed increases from about 10^5 m/s to about $5 \times 10^5\, ms^{-1}$ with the average speed of about $3 \times 10^5\, ms^{-1}$, which is dependent on the height of the thundercloud base, the length of the leader seed, and the delay time, τ_{d0}. A statistical analysis (*Campos et al*., 2014) showed the 2-D speed of downward negative leaders ranges from 0.90 to $19.8 \times 10^5\, ms^{-1}$, with an arithmetic mean value of $3.30 \times 10^5\, ms^{-1}$, which are well consistent with our results.

TABLE 5.2. Simulation parameters used in Section 5.3-5.5.

Symbol	Description	Value	Unit
M	Effective molar mass	114.05491	*g/mol*
H	Height of the cloud base	3000	*m*
H_{seed}	Leader seed length	500	*m*
Δl	Average step length	0.3	*m*
E_{cloud}	Electric field due to the charged cloud	-10	*kV/m*
E_{ground}	Electric field due to corona space charge at ground level	-3	*kV/m*
L_c	Characteristic height	0.25	*km*
E_{c0}	Breakdown electric field at ground level	-750	*kV/m*
g_{L0}	Initial conductance per unit length	0.1	*mS·m*
R_{L0}	Initial leader core radius	1	*mm*
τ_{a0}	Three-body attachment time scale at ground level	≈ 0.1	μs
τ_{d0}	Delay time at ground level	≈ 2.25	μs
η	Heat and vibrational energy lost	0.1	Not applicable

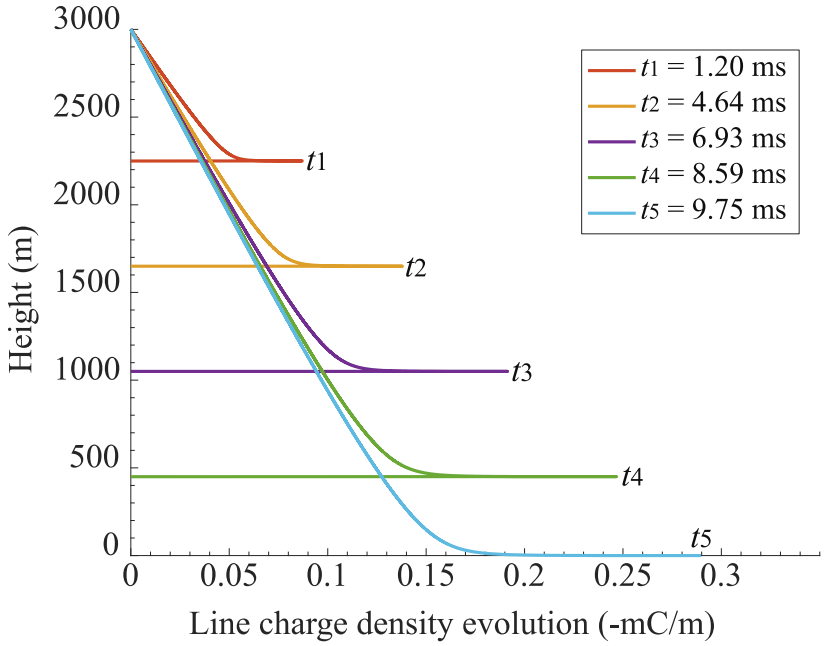

Figure 5.2. Line charge density evolution of the leader with E_{cloud} = -10 kV/m (without space charge layer near the ground).

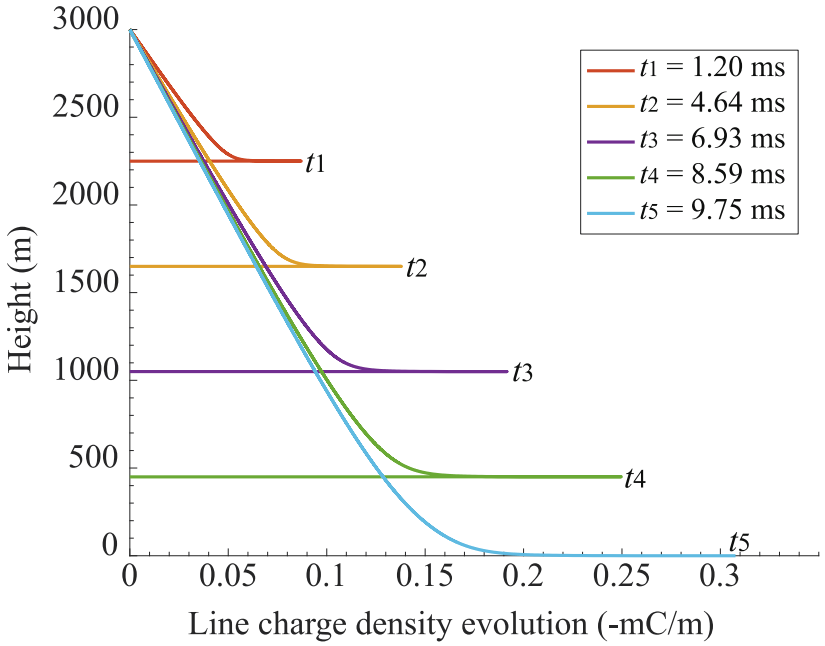

Figure 5.3. Line charge density evolution of the leader with E_{cloud} = -10 kV/m and E_{ground} = -3 kV/m (space charge layer near the ground is included).

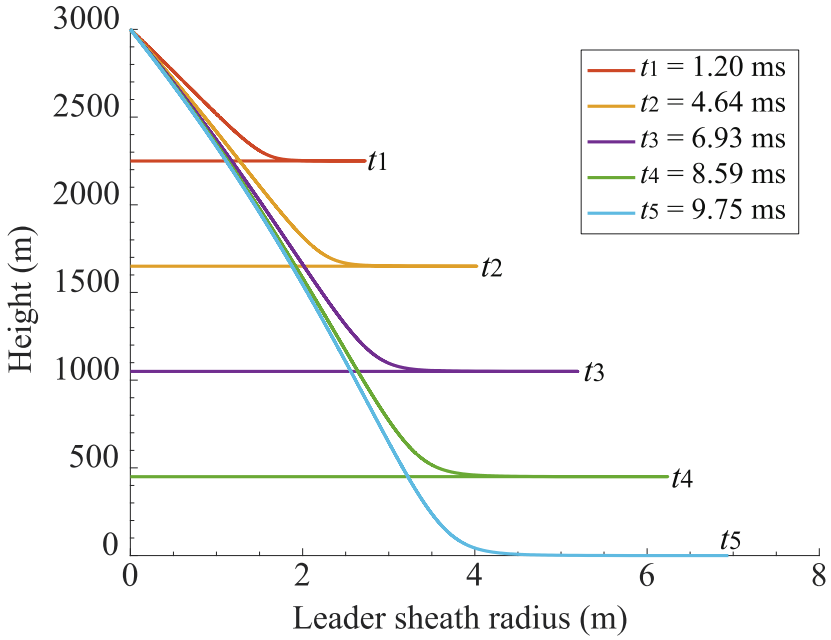

Figure 5.4. Corona sheath radius evolution of the leader with E_{cloud} = -10 kV/m (without space charge layer near the ground).

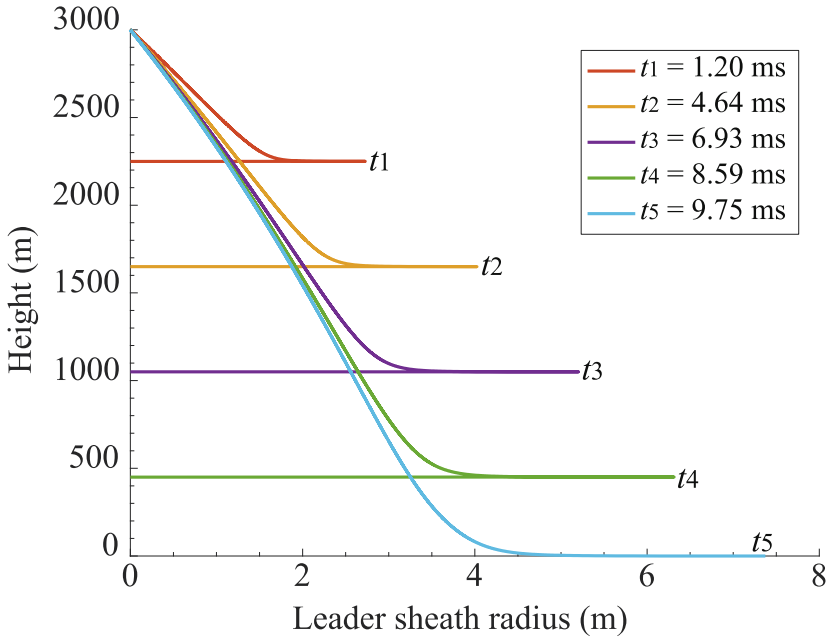

Figure 5.5. Corona sheath radius evolution of the leader with E_{cloud} = -10 kV/m and E_{ground} = -3 kV/m (space charge layer near the ground is included).

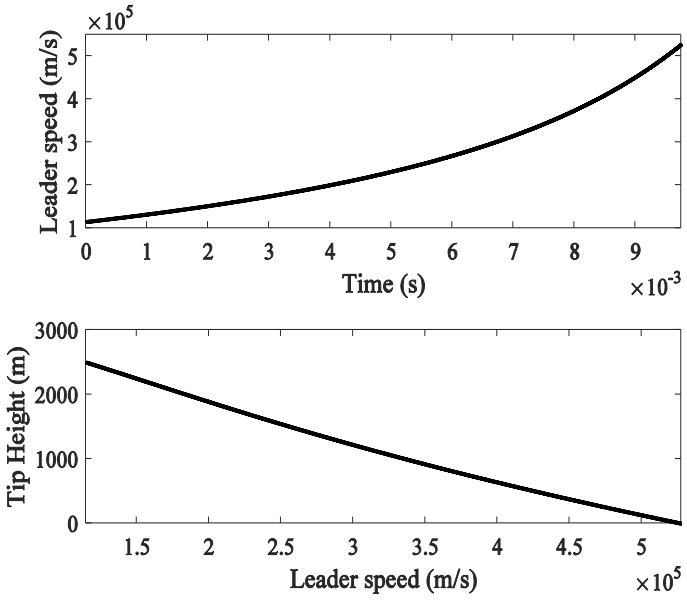

Figure 5.6. (top) Speed against Time, (below) Tip Height against Speed (space charge layer near the ground is included).

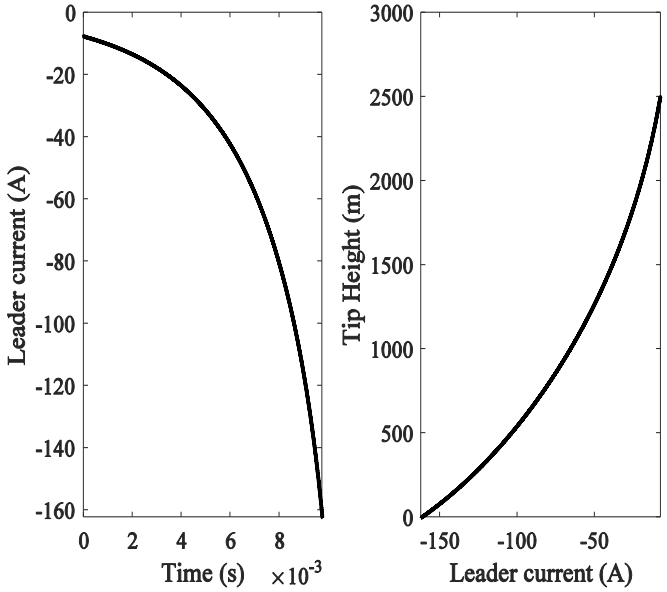

Figure 5.7. (left) Current against Time, (right) Tip Height against Current (space charge layer near the ground is included).

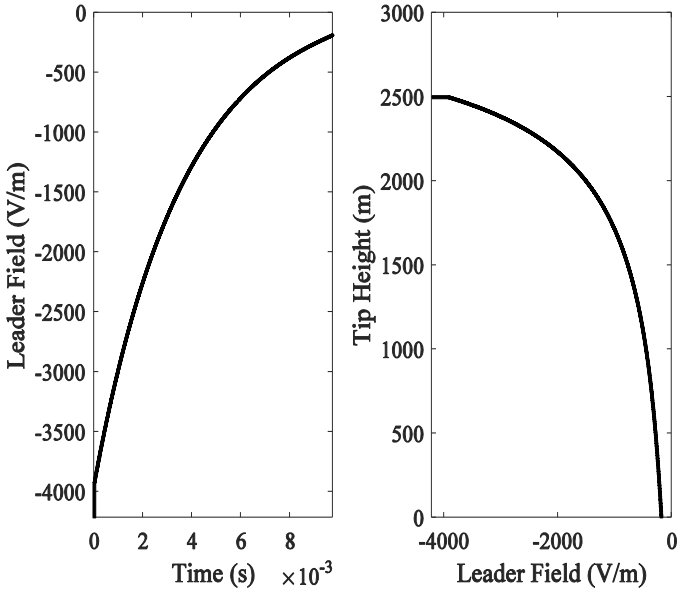

Figure 5.8. (left) E-field against Time, (right) Tip Height against E-field (space charge layer near the ground is included).

5.4 DNL-caused Spatial and Temporal Vertical Ambient Electric Field Profile Above a Flat Ground

Starting in this section, an extra term is added to the vertical ambient electric field:

$$E_A(d,z,t) = E_{cloud} + \left(E_{ground} - E_{cloud}\right)e^{-\frac{z}{L_C}} + E_z(d,z,t), \tag{5.6}$$

where E_z is vertical component the electric field due to the descending leader.

As shown in the **Figure 5.1**, the electric potential at the observing point *P* due to the DNL channel at each propagation time step *j* can be expressed as:

$$V_{DNL}(d,z,t_j) =$$

$$\frac{\Delta l}{4\pi\varepsilon_0}\sum_{i=1}^{j}\lambda_{Lij}\left[\left(\frac{1}{\sqrt{(H-i\Delta l+z)^2+d^2}}-\frac{1}{\sqrt{(H-i\Delta l-z)^2+d^2}}\right)+\left(\frac{1}{\sqrt{(H-z)^2+d^2}}-\frac{1}{\sqrt{(H+z)^2+d^2}}\right)\right], \tag{5.7}$$

where Δl, d, H, z, $H - i\Delta l$ is the propagation step length, the horizontal distance between the DNL and the observing point P, the height of the leader origin, that of the observing point P and that of the i^{th} element to the ground respectively.

In addition, the electrostatics field at P due to the DNL channel at each time step j is given by

$$\boldsymbol{E}_{DNL}(d,z,t_j) = -\nabla V_{DNL} = \begin{pmatrix} E_h(d,z,t_j) \\ E_z(d,z,t_j) \end{pmatrix} =$$

$$\frac{\Delta l}{4\pi\varepsilon_0}\begin{pmatrix} \sum_{i=1}^{j}\lambda_{Lij}\left(\frac{d}{((H-i\Delta l+z)^2+d^2)^{3/2}}+\frac{d}{((H-z)^2+d^2)^{3/2}}-\frac{d}{((H-i\Delta l-z)^2+d^2)^{3/2}}-\frac{d}{((H+z)^2+d^2)^{3/2}}\right) \\ \sum_{i=1}^{j}\lambda_{Lij}\left(\frac{(H-i\Delta l+z)}{((H-i\Delta l+z)^2+d^2)^{3/2}}+\frac{(H-i\Delta l-z)}{((H-i\Delta l-z)^2+d^2)^{3/2}}-\frac{(\mathrm{H}+z)}{((\mathrm{H}+z)^2+d^2)^{3/2}}-\frac{(\mathrm{H}-z)}{((\mathrm{H}-z)^2+d^2)^{3/2}}\right) \end{pmatrix}, \quad (5.8a)$$

$$t_j = \sum_{i=0}^{j}\frac{\Delta l}{v_i}, \quad (5.8b)$$

where E_h and E_z are the horizontal and vertical component of $\boldsymbol{E}_{DNL}$.

At each time step j, the line charge density distribution along the channel can be calculated by the CMB, then $\boldsymbol{E}_{DNL}$ at any point in space can be obtained by Equation (5.8). **Figures 5.9** and **5.10** illustrate the evolution of E_A (Equation 5.6) and V_A verse height with (a) d = 100 m and (b) d = 200 m, E_{cloud} = -10 kV/m, and E_{ground} = -3 kV/m. Other initial values used in this section are shown in **Table 5.2**. Behind the DNL tip, the direction of E_A is reversed.

We assume there are three isolated flat-plate slow antennas placed on the flat ground to measure the electric field change. Shown in **Figure 5.11** is the time evolution of E_z on the flat ground among different horizontal distance (d = 50 m, z = 0 m), (d= 100 m, z = 0 m), and (d = 500 m, z = 0 m).

Mathematically,

$$\boldsymbol{E}_{DNL}(d,0,t_j)=\begin{pmatrix}E_h(d,0,t_j)\\E_z(d,0,t_j)\end{pmatrix}=\frac{\Delta l}{4\pi\varepsilon_0}\begin{pmatrix}0\\\sum_{i=1}^{j}\lambda_{Lij}\left(\frac{2(H-i\Delta l)}{\left((H-i\Delta l)^2+d^2\right)^{3/2}}-\frac{2H}{\left(H^2+d^2\right)^{3/2}}\right)\end{pmatrix}.$$

When $H-i\Delta l=\frac{\sqrt{2}}{2}d$, $\boldsymbol{E_z}(d,0,t_j)$ has a local minimum at that point $\approx \frac{\Delta l}{4\pi\varepsilon_0}\sum_{i=1}^{j}\lambda_{Lij}\left(\frac{0.7698}{d^2}-\frac{2H}{(H^2+d^2)^{3/2}}\right)$.

Since λ_{Lij} is negative (DNL is propagating to the ground), E_z at all positions first decrease at different time and later begin to increase. When d is larger, ${E_z}''(d,0,t_j)|_{H-i\Delta l=\frac{\sqrt{2}}{2}d}\rightarrow 0$, the shape of E_z is wider and shorter and finally becomes positive. Our calculated electric field shapes are similar to the electric field change measurement reported in *Saba et al*. (2015).

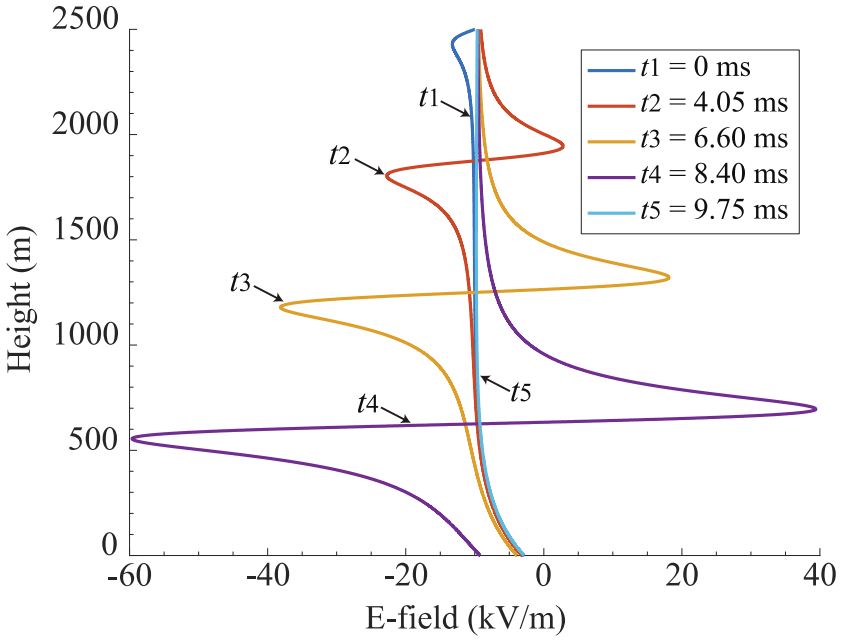

(a)

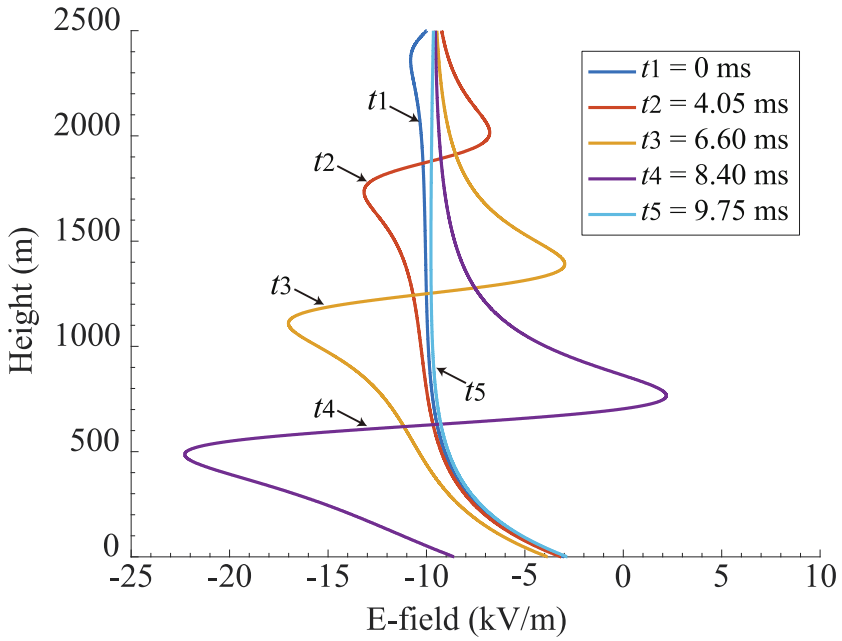

(b)

Figure 5.9. Ambient electric field evolution verse height with (a) d = 100 m and (b) d = 200 m (space charge layer near the ground is included).

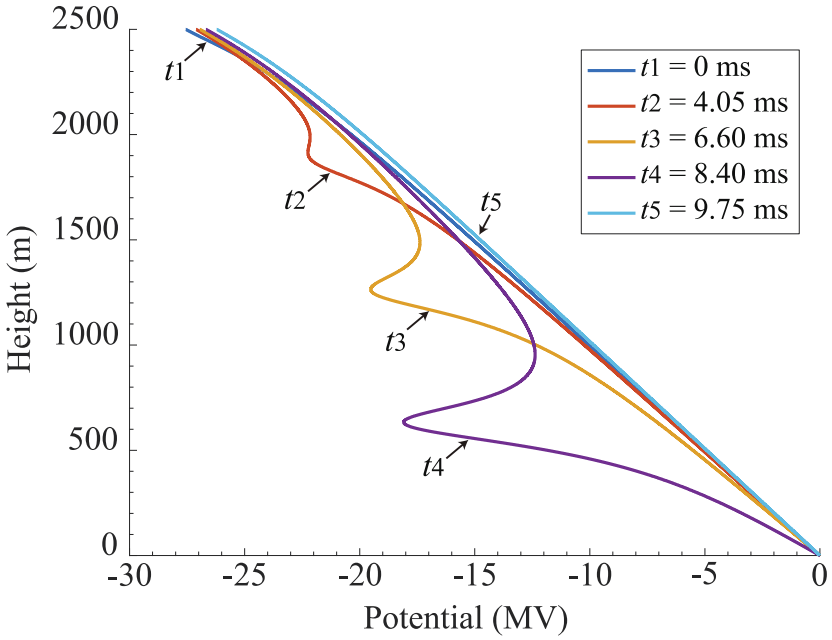

(a)

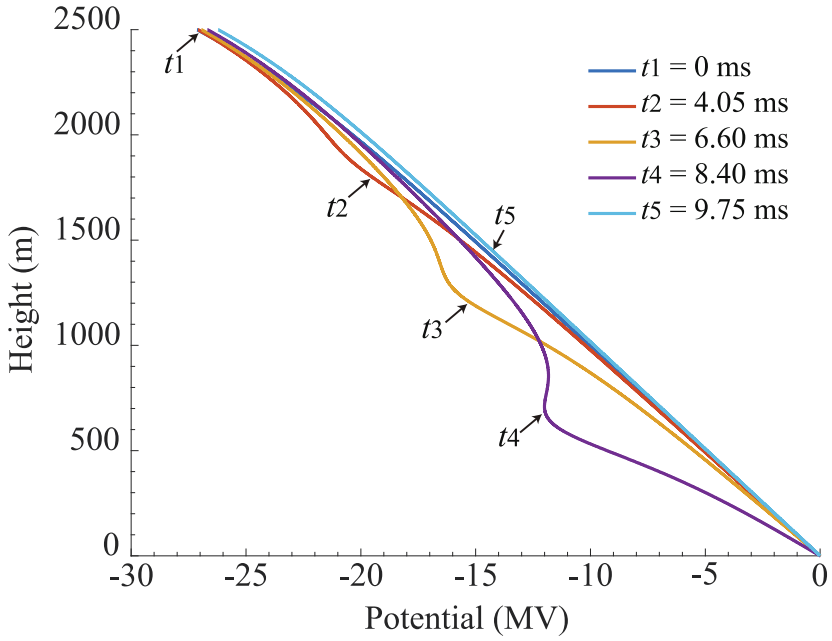

(b)

Figure 5.10. Ambient electric potential evolution verse height with (a) d = 100 m and (b) d = 200 m (space charge layer near the ground is included).

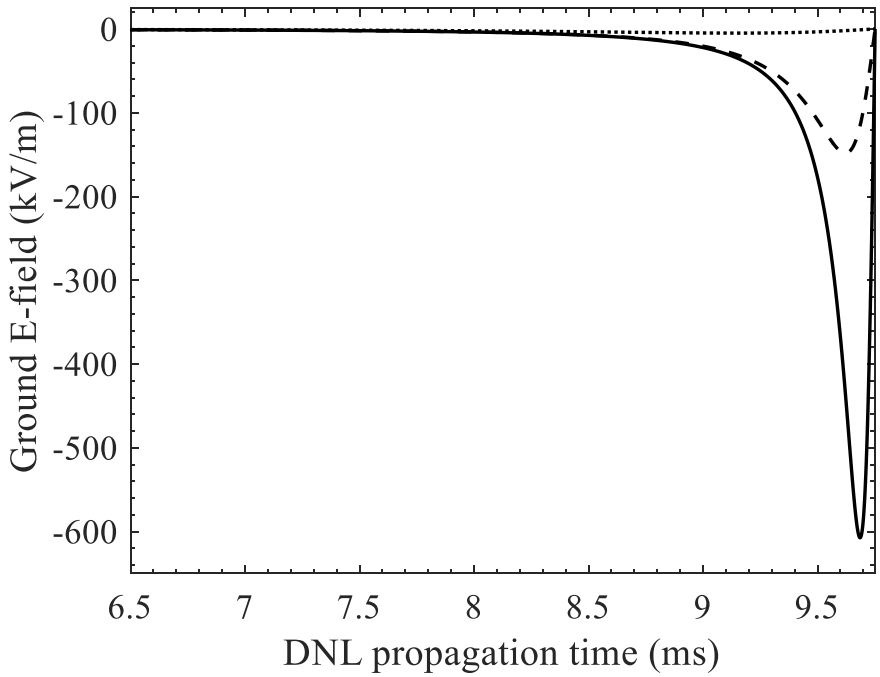

Figure 5.11. Ground electric field change produces by the DNL and cloud source as a function of time with different distance *d* (solid: *d* = 0 m), (dash: *d* = 100 m), and (dot: *d* = 500 m) (space charge layer near the ground is included).

5.5 DNL-triggered Upward Positive Leader Simulation

Rizk (1994) assumed that during the lightning attachment process, while the downward leader keeps propagating vertically down without being affected by the grounded object and the upward leader, the upward leader would always move toward the tip of the downward leader. This is because the electric field due to the downward leader is much larger than the upward leader.

To simulate a DNL-triggered UPL, all equations showed in chapter 3 for calculating the UPL are modified to include the electric field (E_z) and potential (V_{DNL}). However, in our model, for a fixed Δl, the propagation time step of each leader Δt, will be different. Hence, it is necessary to interpolate the whole-time series of the E_z and V_{DNL} to adapt with each time step of the UPL.

The UPL survival condition is same as Chapter 3:

$$E_{UL} < E_A,$$

$$E_{UL} < E_{cloud} + \left(E_{ground} - E_{cloud}\right)e^{-\frac{z}{L_c}} + E_z, \qquad (5.9a)$$

$$\Rightarrow I_{UL} > \frac{b}{E_{cloud}+\left(E_{ground}-E_{cloud}\right)e^{-\frac{z}{L_c}}+E_z}, \qquad (5.9b)$$

According to the results in section 5.4, it is easy to show when the UPL tip is higher than the DNL tip, the direction of E_z is reversed, hence $E_{UL} \geq E_A$ is met and the UPL will stop propagating and the leader's current cutoff begins [*Mazur and Ruhnke*, 2014], unless it is horizontally close to the DNL. Our simulation scenario is illustrated in **Figure 5.12**, a DNL propagates overhead an UCL with some UULs triggered at other different height of objects. Details of simulation results are shown as follow:

Again, all initial values of the DNL used in this section is shown in **Table 5.2**. Shown in **Figure 5.13** and **5.14** are simulation results for the UCL and UULs at four isolated buildings (UUL1, d = 100 m, $z = h$ = 100 m), (UUL2, d = 100m, $z = h$ = 200m) and (UUL3, d = 200m, $z = h$ = 200m), and the down-coming DNL, E_z is adopted from the results discussed in section 5.4. However, the E_z at another building (d = 200m, $z = h$ = 100m) is not strong enough to trigger any UUL. Simulation results show that when an UPL is just initiated, $E_{UL} > E_{cloud}$. This large leader core electric field is balanced by the E_z. In our model, we assume the initiation speed of each UPL is a constant (Chapter 3), which may need to further validate by observation. Note that our model is based on electrostatics only, which cannot be used to simulate the transient final breakdown process (*Rosy et al*., 2011; *Cai et al*., 2017). When both streamer zone tips are touched, the final

breakdown process is imminent and the simulation stops. The size of the touched streamer zones showed in **Figure 5.13** is about 29 m.

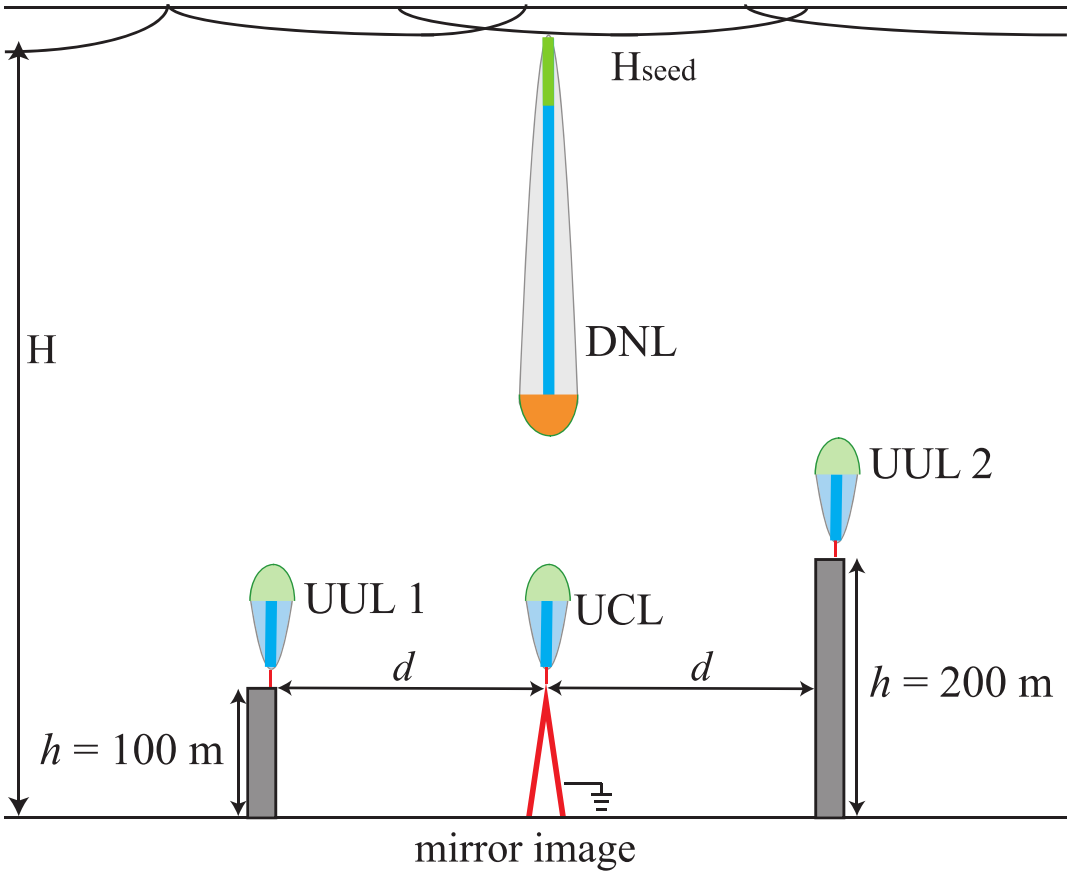

Figure 5.12. Sketch of the simulation: a DNL propagates overhead an UCL with two UULs triggered at different height of objects (not drawn to scale).

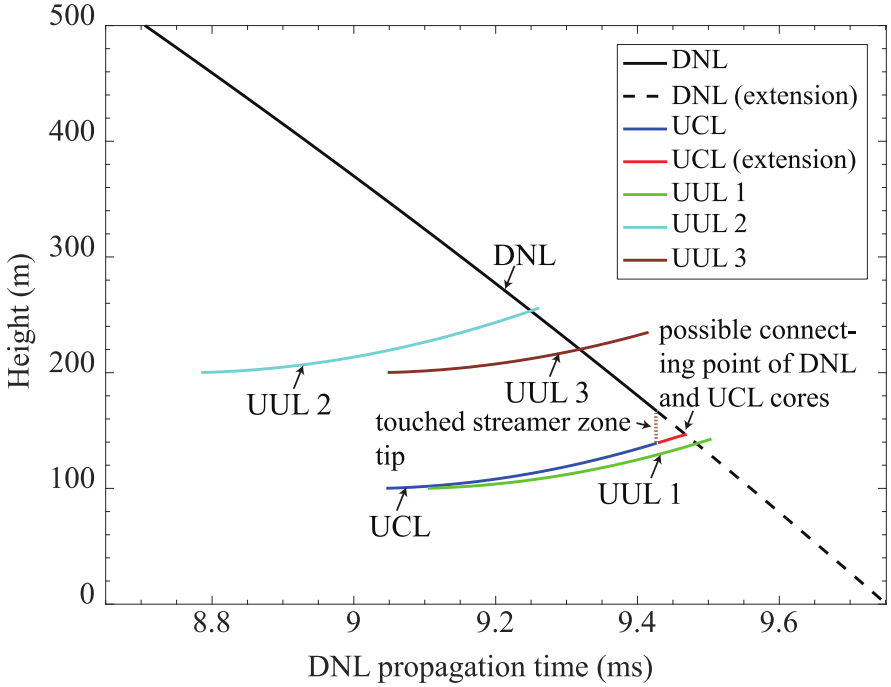

(a)

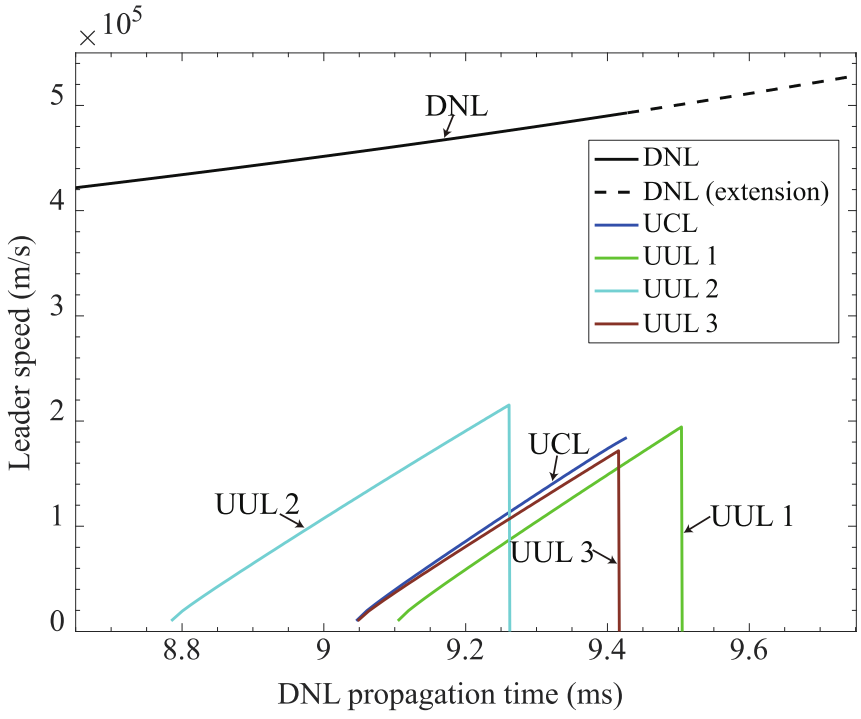

(b)

Figure 5.13. Simulation results (space charge layer near the ground is included): (a) the Altitude-time graph and (b) the Leader speed-time graph.

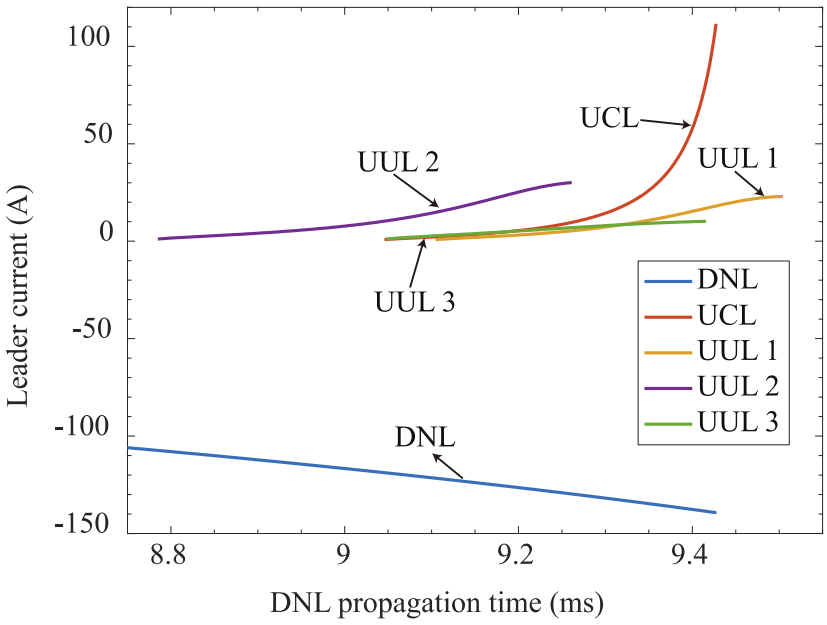
100
50
0
-50
-100
-150
Leader current (A)
8.8
9
9.2
9.4
DNL propagation time (ms)
UCL
UUL 2
UUL 1
UUL 3
DNL
DNL
UCL
UUL 1
UUL 2
UUL 3

(a)

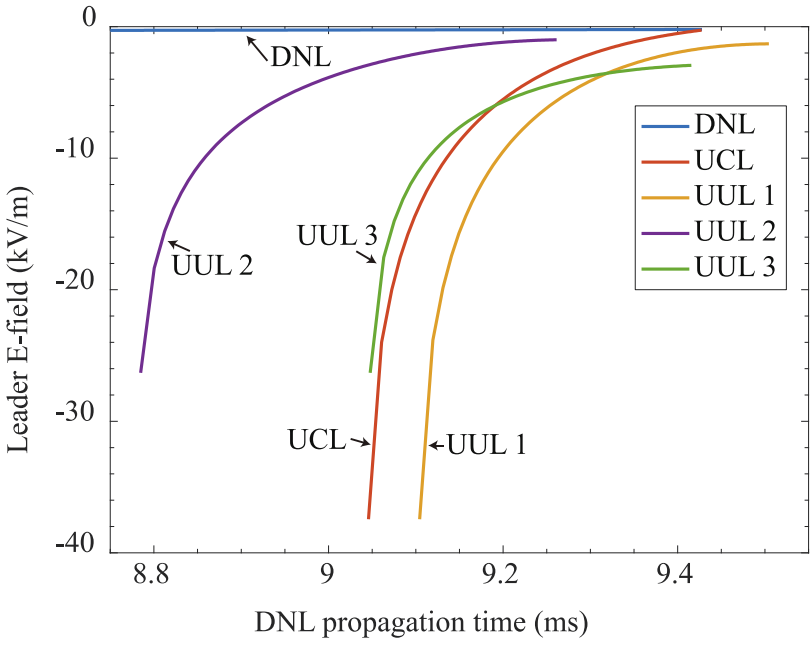
0
-10
-20
-30
-40
Leader E-field (kV/m)
8.8
9
9.2
9.4
DNL propagation time (ms)
DNL
UUL 2
UUL 3
UCL
UUL 1
DNL
UCL
UUL 1
UUL 2
UUL 3

(b)

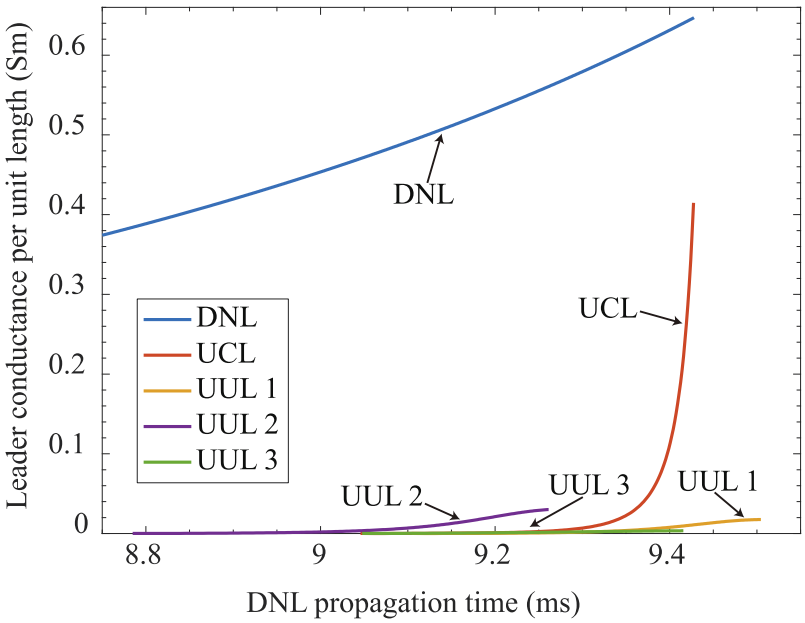

(c)

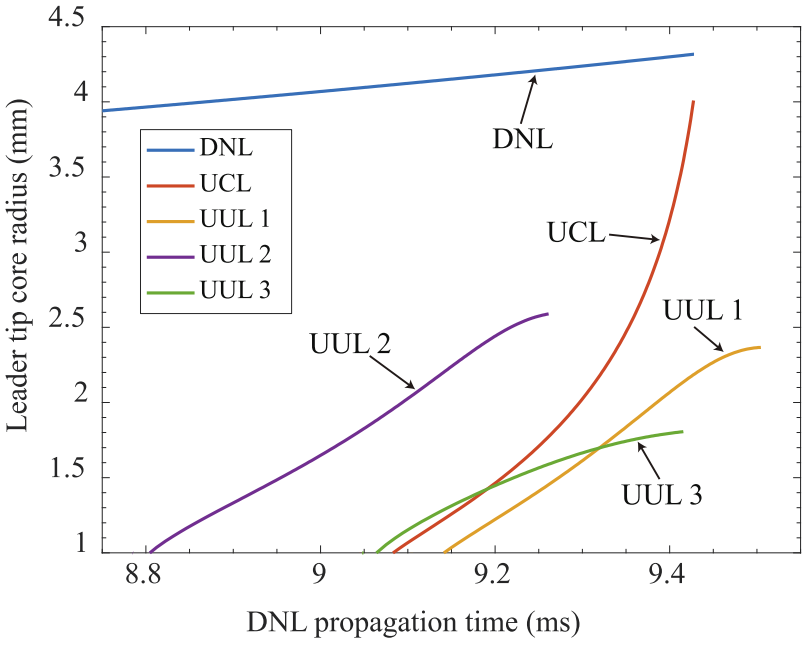

(d)

Figure 5.14. Simulation results (space charge layer near the ground is included): (a) Leader current verse propagation time, (b) Leader E-field verse propagation time (c) Leader conductance verse propagation time, and (d) Leader core radius verse propagation time.

Shown in **Figure 5.15** is leader line charge density evolution of a UCL (d = 0 m, h = 100 m) and other three UULs at the top of three isolated buildings (d = 100 m, h = 100 m), (d = 100 m, h = 200 m) and (d = 200 m, h = 200 m). The charge distribution along the UCL channel tends to increase exponentially but the charge distribution along each UUL increases linearly. The final value of the UCL is about twice larger than the DNL.

5.5.1 Striking Distance Estimation

We can also estimate the striking distance (S), which is the distance between the downward leader tip and the top of the object, where the streamer zones of DNL and UCL come in contact (*Tran* and *Rakov*. 2015). While most of the existing striking distance equation is estimated by the prospective return stroke peak current, in our model, the striking distance is as a function of E_{cloud} and E_{ground}. We select E_{cloud} = - 10 kV/m and E_{ground} = -3 kV/m as an example. Data with different height of objects is shown in **Table 5.3. Figure 5.16** shows the estimated striking distance is linearly related to the estimated object height. The higher the isolated grounded object, the longer the estimated striking distance. From that figure, if there is no any object (z = h = 0 m), the estimated striking distance is about 29.6 m.

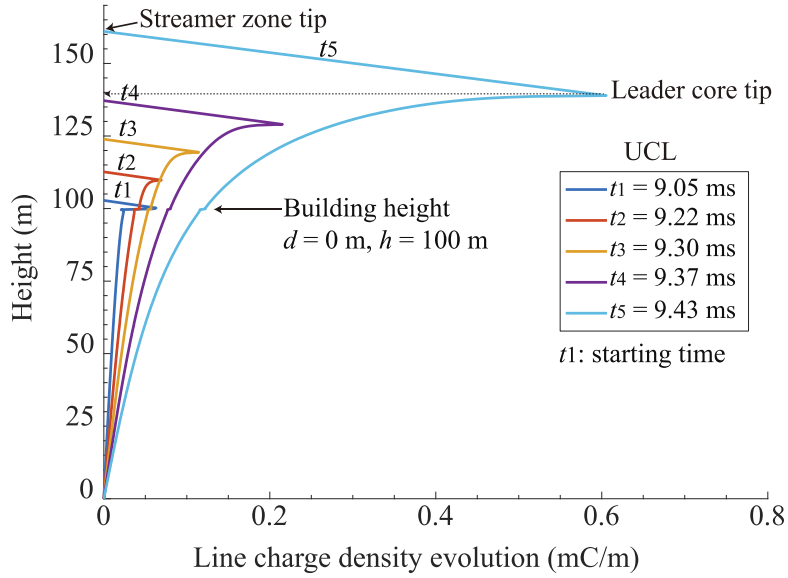

(a)

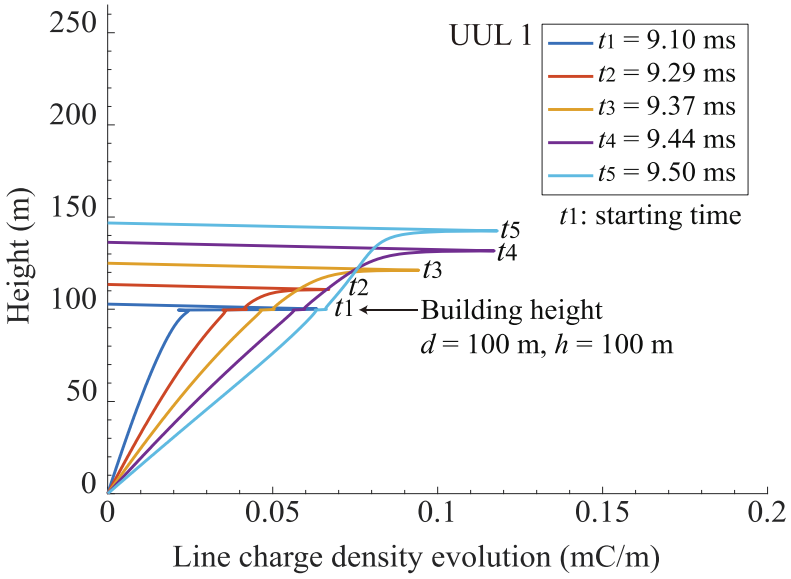

(b)

Figure 5.15. Line charge density evolution (space charge layer near the ground is included): (a) UCL (d = 0 m; z = h = 100 m) , (b) UUL 1 (d = 100 m; z = h = 100 m), (c) UUL 2 (d = 100; z = h = 200 m) and (d) UUL 3 (d =200 m; z = h = 200 m).

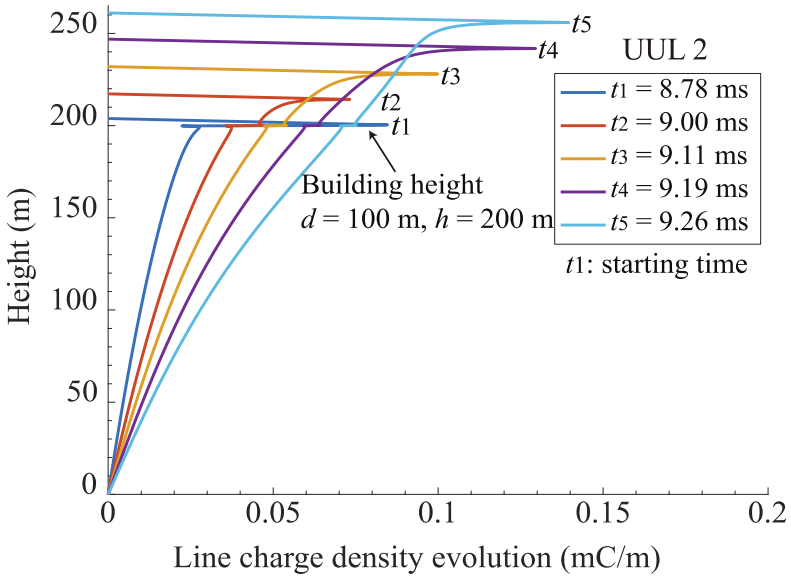

(c)

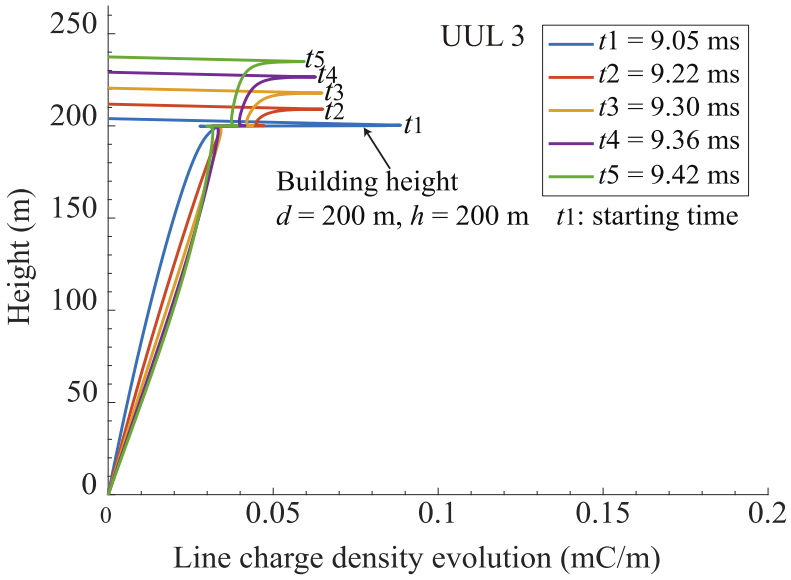

(d)

Figure 5.15. Line charge density evolution (space charge layer near the ground is included): (a) UCL (d = 0 m; z = h = 100 m) , (b) UUL 1 (d = 100 m; z = h = 100 m), (c) UUL 2 (d = 100; z = h = 200 m) and (d) UUL 3 (d =200 m; z = h = 200 m).

Table 5.3. Striking distance estimation for E_{cloud} = - 10 kV/m and E_{ground} = -3 kV/m.

Object height, *h* (m)	Striking distance, *S* (m)	UCL propagation length (m)
0	29.6	8.50
50	59.2	31.9
100	66.8	39.1
200	80.5	52.6
300	93.4	66.4
400	107.5	80.8
500	122.5	97.0
600	141.9	116.5

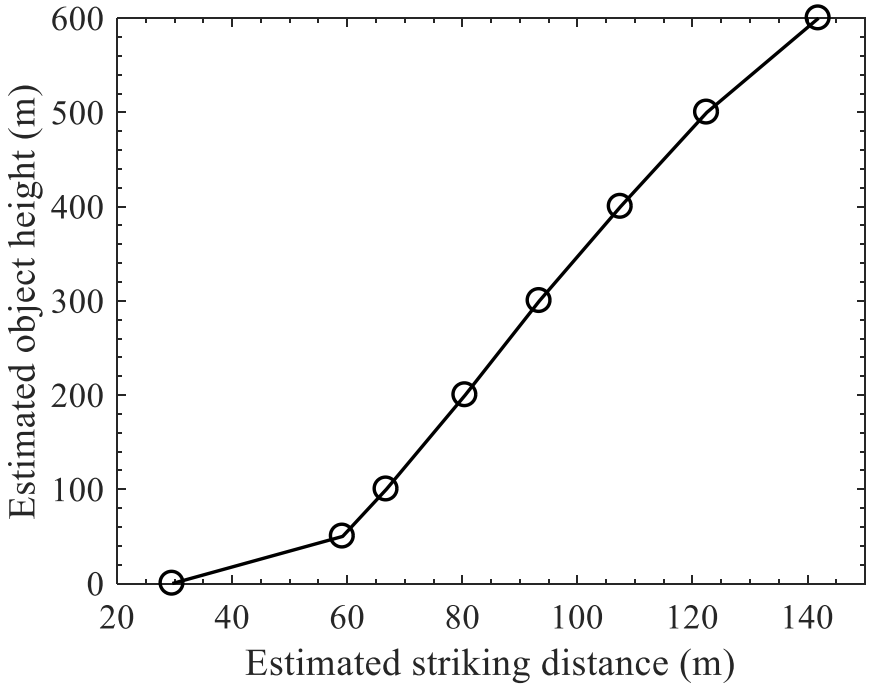

Figure 5.16. Estimated striking distance verse Estimated object height for E_{cloud} = - 10 kV/m and E_{ground} = -3 kV/m (space charge layer near the ground is included).

5.5.2 UCL Spatial and Temporal Vertical Electric Field

To check whether the Rizk`s assumption is correct. We have derived a simple electric field equation generated by an UCL. As shown in the **Figure 5.17**, the scalar potential at the observing point *P* due to the UPL channel at step *j* can be expressed as:

$$V(d,z,t_j)=\frac{\Delta l}{4\pi\varepsilon_0}\sum_{i=1}^{j}\lambda_{Lij}\left(\frac{1}{\sqrt{(H+i\Delta \mathrm{l}-z)^2+d^2}}-\frac{1}{\sqrt{(H+i\Delta \mathrm{l}+z)^2+d^2}}\right), \tag{5.10}$$

where *d*, H, *h* and H + *i*Δ*l* is horizontal distance between the upward positive leader and the observing point *P*, the height of the leader origin, that of the observing point *P* and that of the i^{th} element to the ground respectively.

The electrostatics field at *P* due to the UPL channel at step *j* is given

$$\boldsymbol{E}(d,z,t_j)=-\nabla V=\boldsymbol{E_h}(d,\mathrm{z},t_j)+\boldsymbol{E_z}(d,z,t_j),$$

$$\boldsymbol{E_h}(d,z,t_j)=\frac{\Delta l d}{4\pi\varepsilon_0}\sum_{i=1}^{j}\lambda_{Lij}\left(\frac{1}{((H+i\Delta l-z)^2+d^2)^{3/2}}-\frac{1}{((H+i\Delta l+z)^2+d^2)^{3/2}}\right), \tag{5.11a}$$

$$\boldsymbol{E_z}(d,z,t_j)=\frac{-\Delta l}{4\pi\varepsilon_0}\sum_{i=1}^{j}\lambda_{Lij}\left(\frac{(H+i\Delta l-z)}{((H+i\Delta l-z)^2+d^2)^{3/2}}+\frac{(H+i\Delta l+z)}{((H+i\Delta l+z)^2+d^2)^{3/2}}\right), \tag{5.11b}$$

$$t_j=\sum_{i=0}^{j}\frac{\Delta l}{v_i},$$

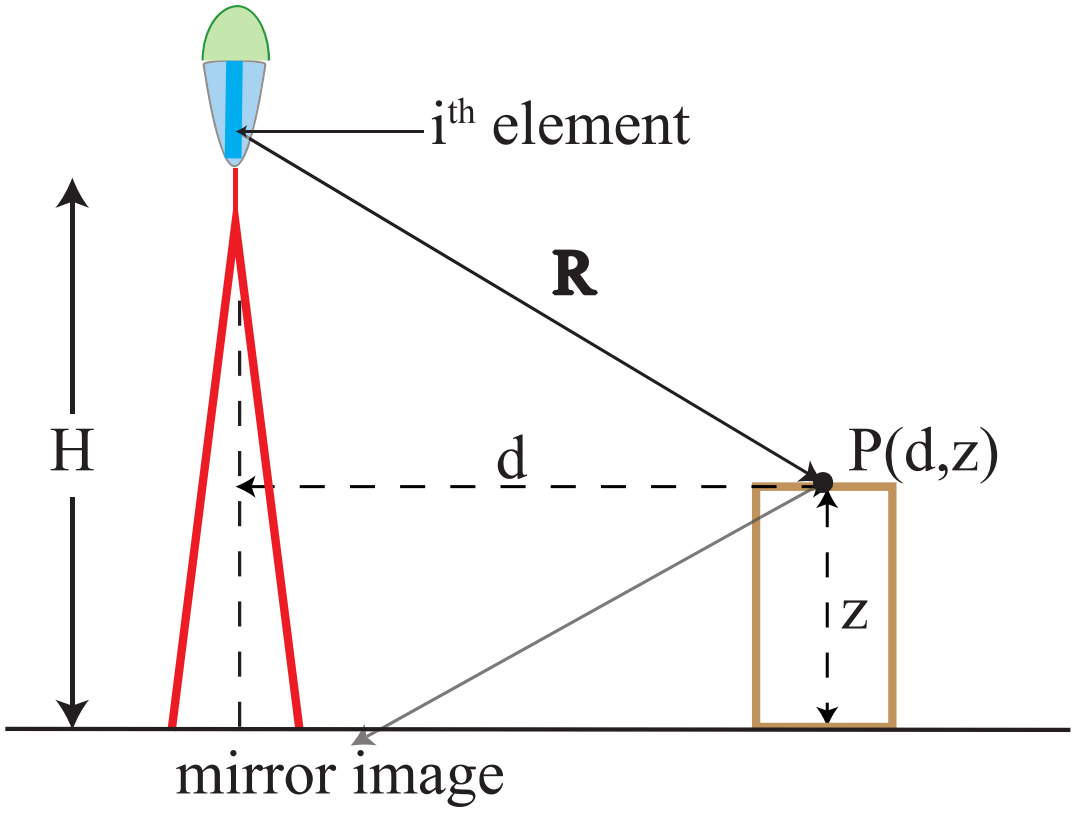

Figure 5.17. Sketch of the E-field calculation at point P (not drawn to scale).

Shown in **Figure 5.18** is the ground-level E-field as a function of propagation length of the UCL triggered at a 100-m object (d = 0 m; $z = h$ = 100 m). Since the positive ground-level electric field due to the UCL is very small ($E_{UL} << |E_A|$), our calculation agrees with the Rizk`s assumption that the effect of the UPL along the DNL is insignificant.

Wang et al. (2008b) have pointed a possible situation that an upward leader occurred from a tall grounded object may trigger another upward leader with opposite polarity from a nearby high-grounded object if favorable electrical charge structures of thunderstorms are available. In a follow up study, *Lu et al*. (2009) have recently observed two associated upward lightning with opposite polarity in Japan. However, from our calculation (**Figure 5.18**), although the ground-level electric field polarity due to the UCL is different from the

DNL, this electric field is much smaller than the DNL's. Our results may suggest this phenomenon is only due to the strong descending leader generates a large electric field at different position, which may be either positive or negative, depends on the exact distance between the leader and each tall grounded object. Our calculation (**Figure 5.19**) also shows when point P is higher than the object, the direction of E_z is reversed.

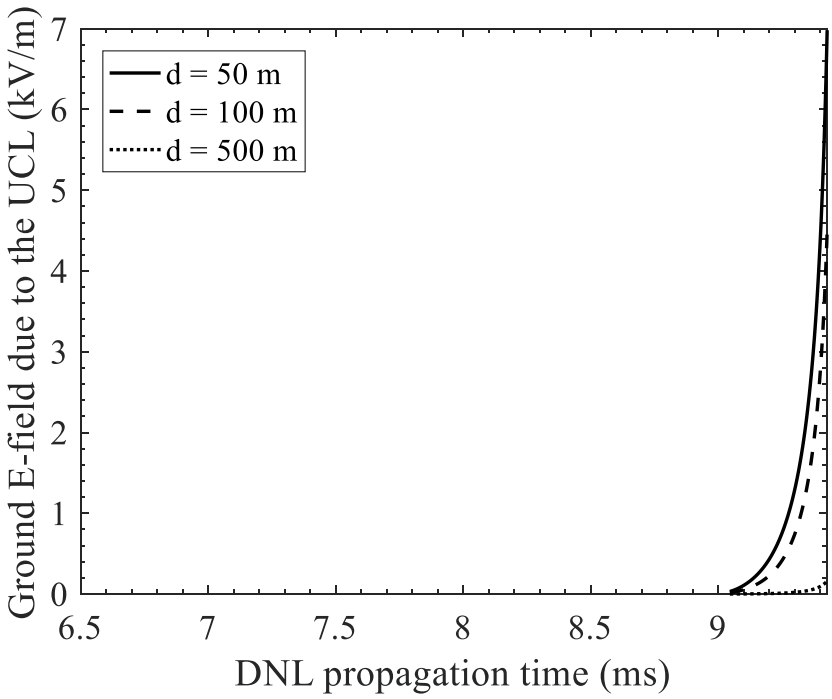

Figure 5.18. Ground E-field due to the UCL initiated at the top of a 100-m object as a function of DNL propagation time with different distance *d* (solid: *d* = 50 m), (dash: *d* = 100 m), and (dot: *d* = 500 m) (space charge layer near the ground is included).

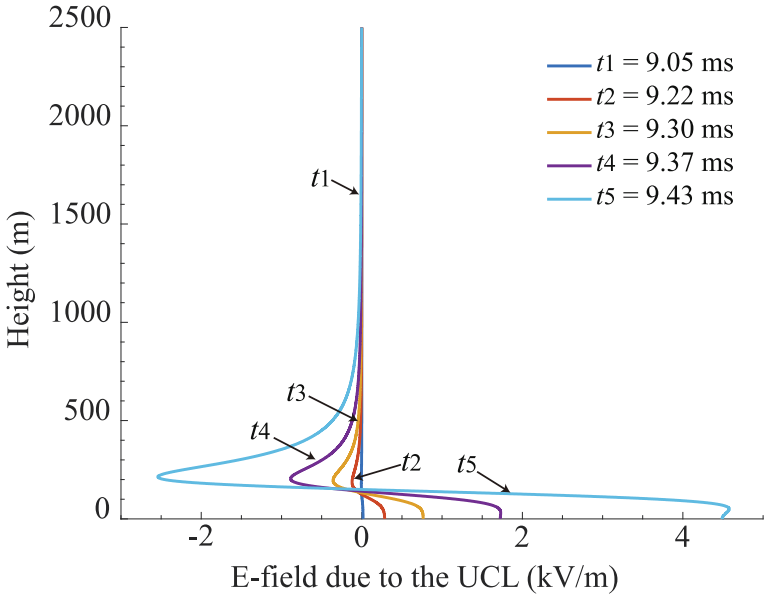

(a)

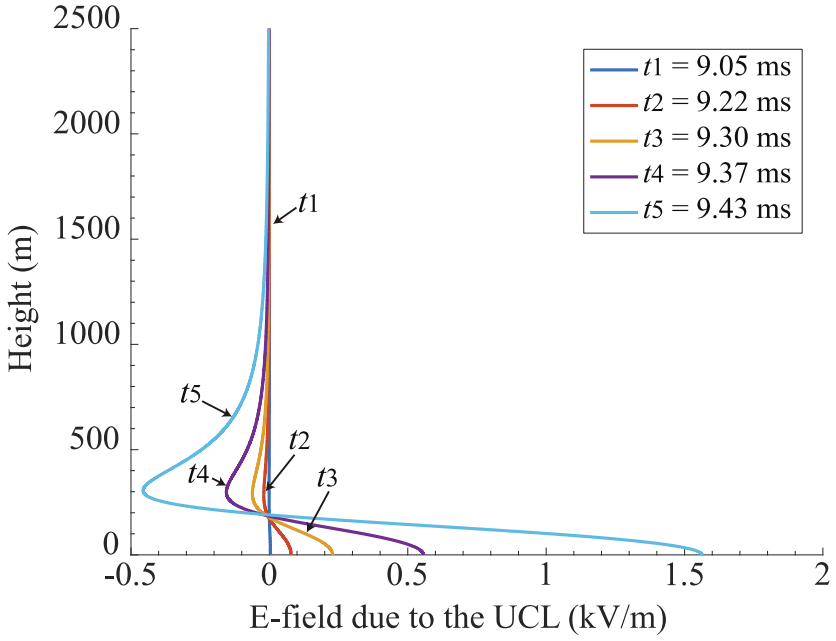

(b)

Figure 5.19. E-field due to the UCL initiated at the top of a 100-m object verse height with different *d* (a), (*d* = 100 m), and (b) (*d* = 200 m) (space charge layer near the ground is included).

Figures 5.20 and **5.21** illustrate the total ground E-field changes due to the DNL and the UCL at close distance (d = 50 m and 100 m) and far distance (d = 0.5 km, 1 km, and 5 km). These close and far distance E-field shapes (**Figure 5.22**) are similar to the electric field change measurements reported in *Jerauld et al.* [2008].

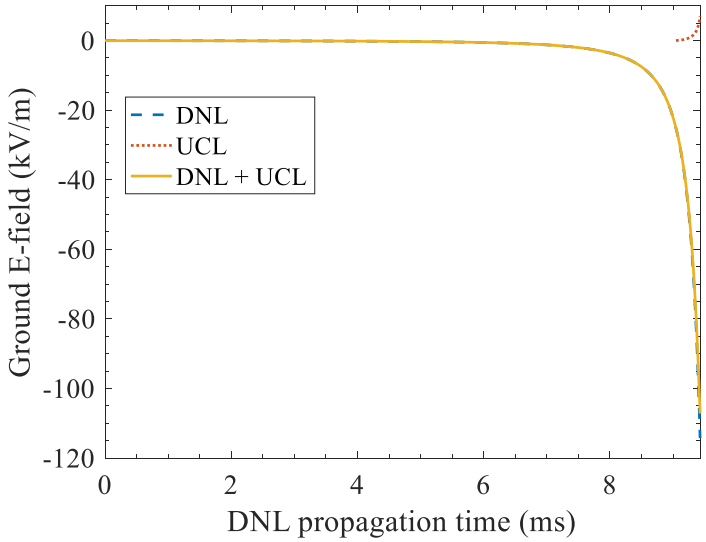

(a)

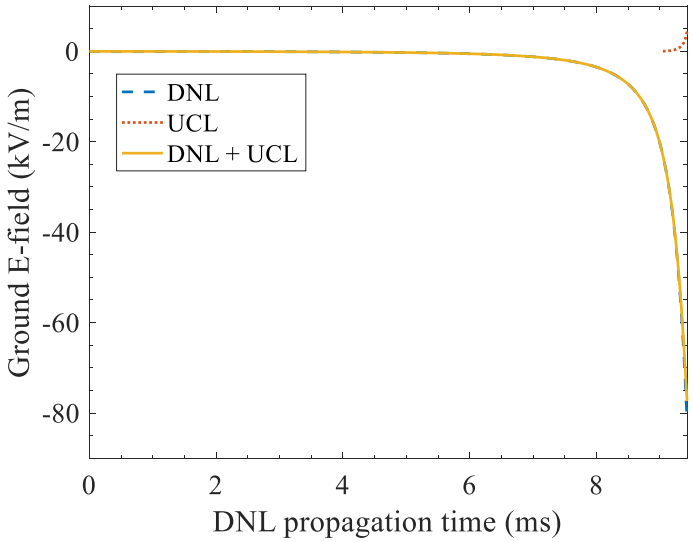

(b)

Figure 5.20. Ground E-field changes due to the DNL and UCL with different distance d (a), (d = 50 m) and (b) (d = 100 m) (space charge layer near the ground is included).

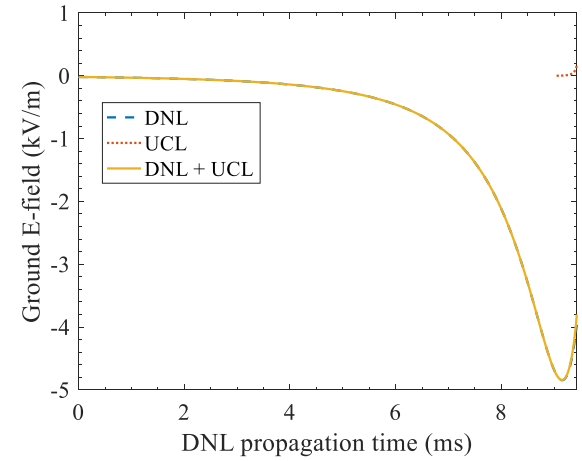

(a)

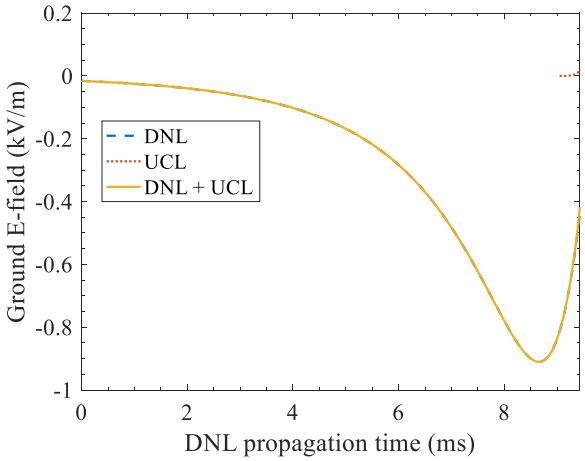

(b)

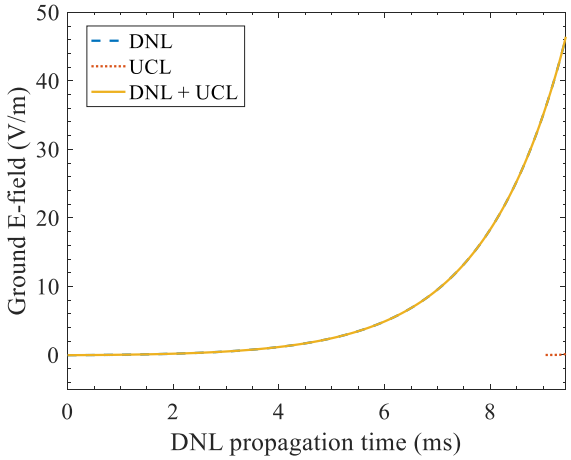

(e)

Figure 5.21. Ground E-field changes due to the DNL and UCL with different far distance *d* (a), (*d* = 0.5 km), (b) (*d* = 1 km), and (c) (*d* = 5 km) (space charge layer near the ground is included).

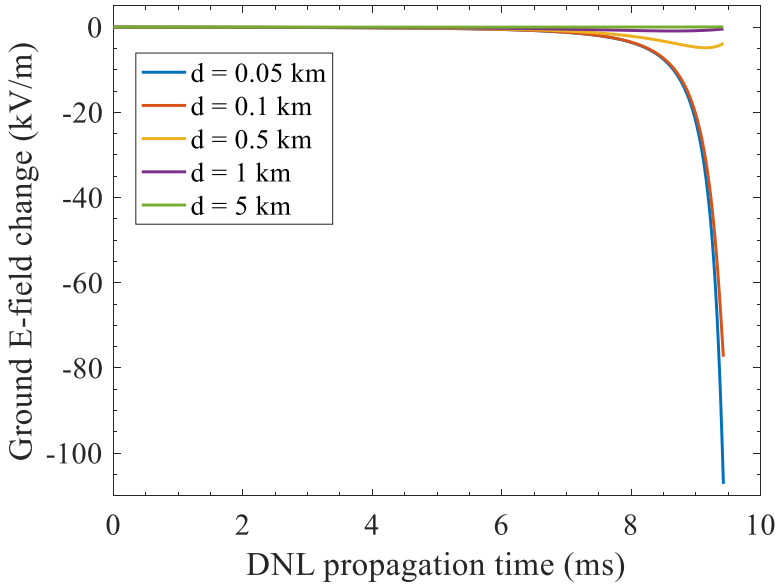

Figure 5.22. Ground E-field changes due to the DNL and UCL with different distance *d*, (blue) (*d* = 0.05 km), (red) (*d* = 0.1 km), (yellow) (*d* = 0.5 km), (purple) (*d* = 1 km), and (green) (*d* = 5 km) (space charge layer near the ground is included).

5.6 Case Study 1: an UCL and UULs Triggered from Residential Buildings by an Approaching DNL

Case B of lightning strokes to two identical residential buildings Sao Paulo in works of *Saba et al*. (2016a) is adopted for modelling with the present model. The attachment process included a DNL, an UCL and two UULs, which were recorded with a high-speed camera with time-resolution of 50 μs (20,000 fps). Both buildings, including the lightning rod, have the same height of 52 m above ground.

A summary of the observed results is shown in **Figure 5.23** and **5.24**, which is cited from *Saba et al*. (2016a) for Case B. (Time 0 is set at the beginning of the return stroke.) In another study, *Saba et al*. (2016b) reported that the height of the thundercloud base in Sao Paulo is usually in a range of 1.2 - 3.4 km. The topography presented in *Saba et al*. (2016a) showed that the surrounding terrain of those buildings is relatively flat. Details of our simulations of this case are as follows:

Shown in **Figure 5.25** is a schematic diagram of the DNL, the UCL from P2 and the UUL from P1 for simulation use. The pair of 52 m grounded objects are simply assumed as two lightning rods with a radius of 1 cm, placed on the ground. The distance between two rods is assumed to be 25 m. A 500 m leader seed of the DNL is assumed to initiate from the cloud base at a height of 1800 m overhead the P2 building and the altitude above mean sea level is estimated at about 780 m. The values of E_{cloud}, E_{ground}, L_c, and τ_{d0} are -6.45 kV/m, -1 kV/m, 800 m, and 3.01 s respectively. The average step length of DNL and UPL, Δl, is fixed to 0.2 m. Our simulation results are shown in **Figure 5.26**. which matches well with the observation as shown in **Figure 5.24**. Other physical parameters of the leaders are shown in **Figures 5.27 and 5.28**.

Similar to **Figures 5.20 - 5.22**, we can also calculate the total ground E-field changes due to the DNL and the UCL among different distances (0.05 km – 5 km) (**Figure 5.29**). However, the reference does not provide the ground electric field change measurement.

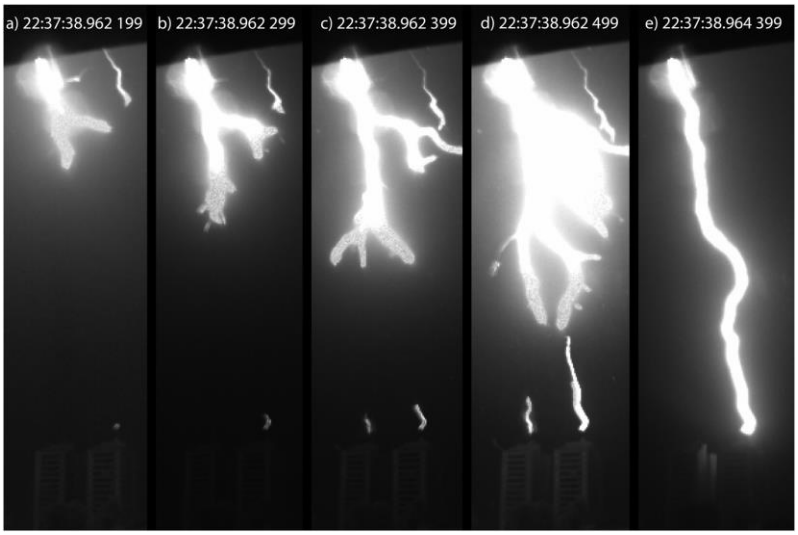

Figure 5.23. Sequence of video images showing the initiation and development of an UCL and two UUL (adapted from *Saba et al*. 2016a).

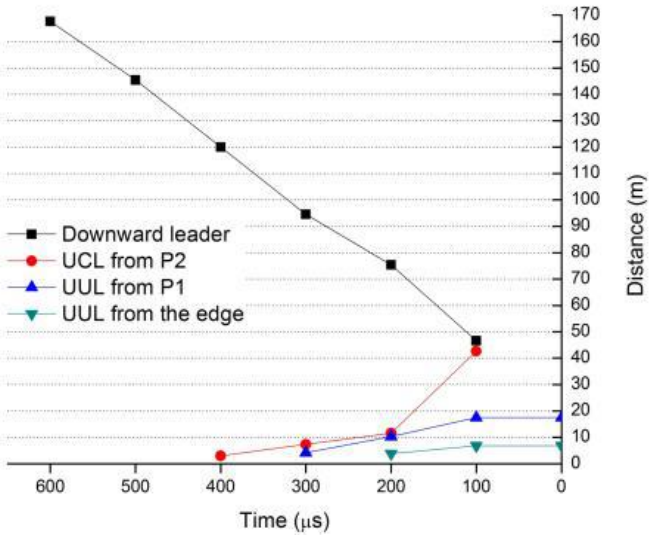

(a)

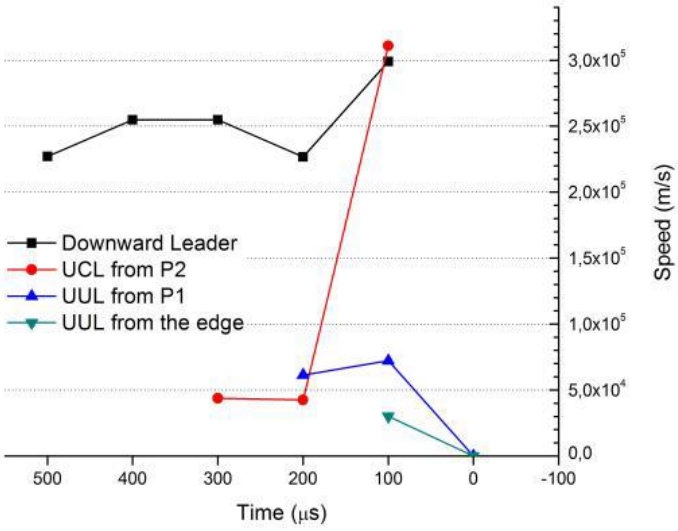

(b)

Figure 5.24. Observation results of Case B: a lightning stroke to two buildings including a DNL, a UCL and two UUL leaders. (a) the distance-time graph and (b) the average speed-time graph for these leaders. Adapted from Saba et al. (2016a).

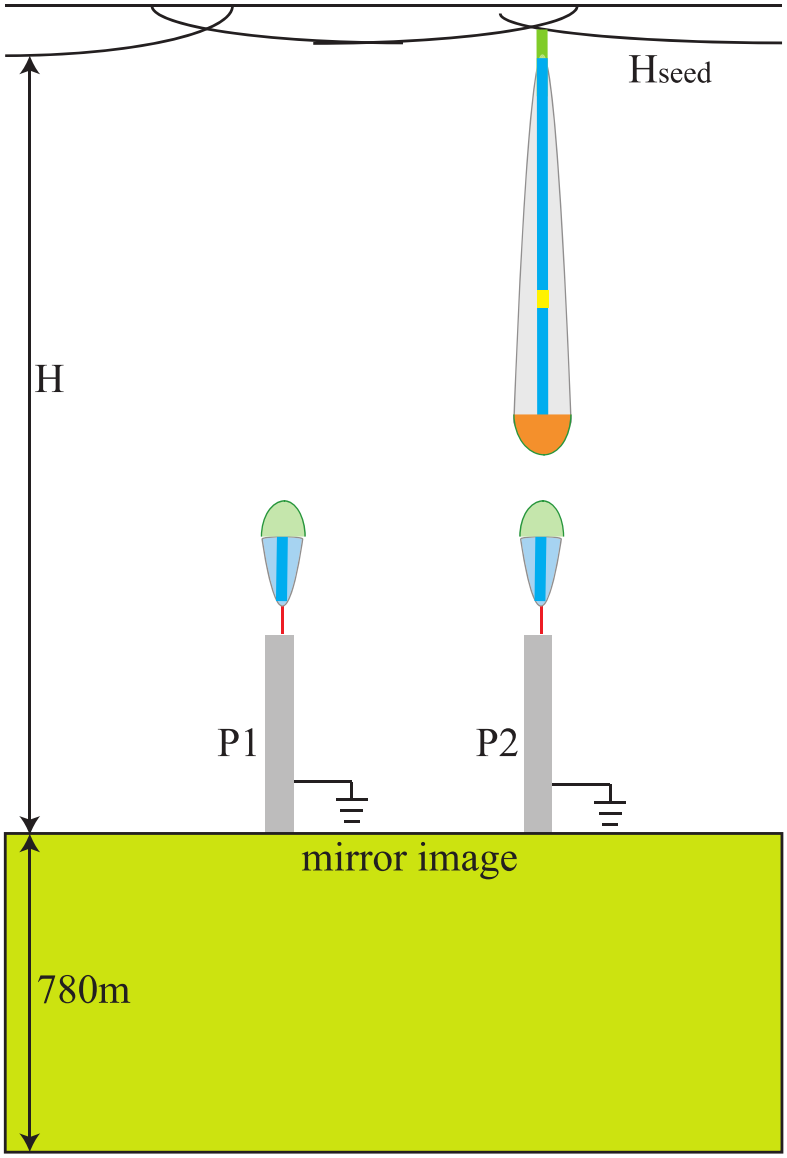

Figure 5.25. A schematic diagram of the DNL, UCL from P2 and the UUL from P1 for modelling use (not drawn to scale).

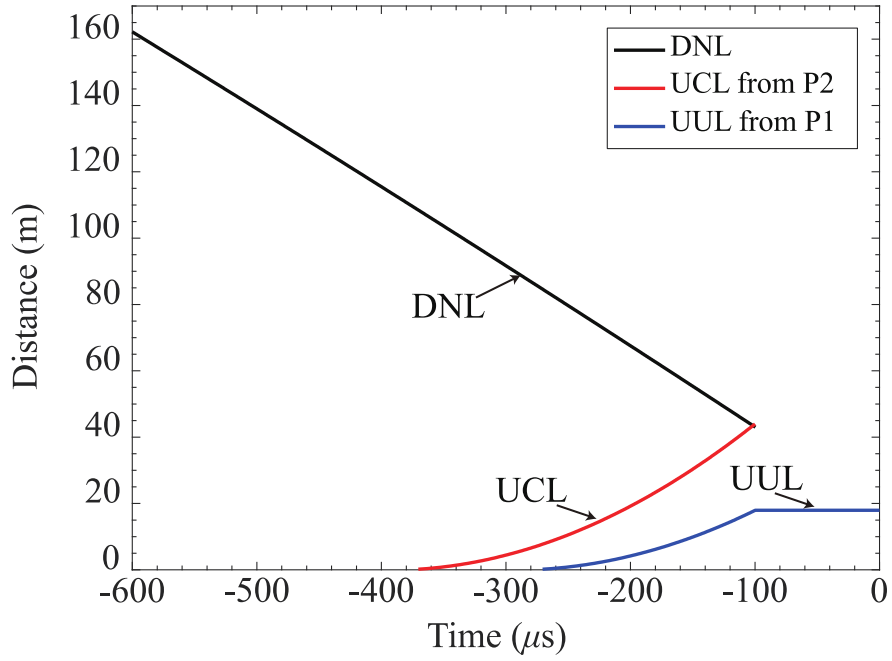

(a)

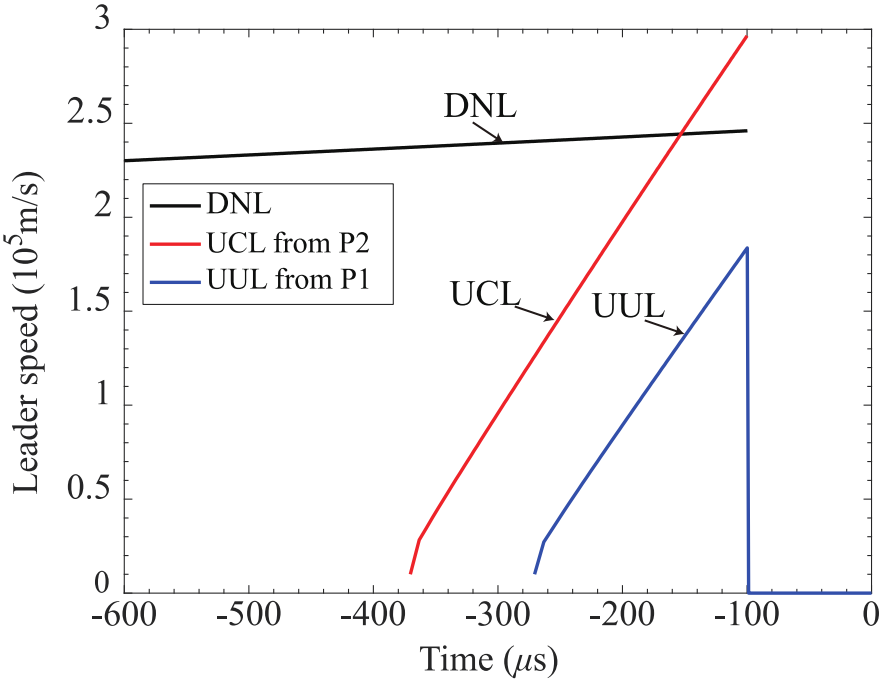

(b)

Figure 5.26. Simulation results (space charge layer near the ground is included): (a) the Distance-time graph and (b) the Speed-time graph.

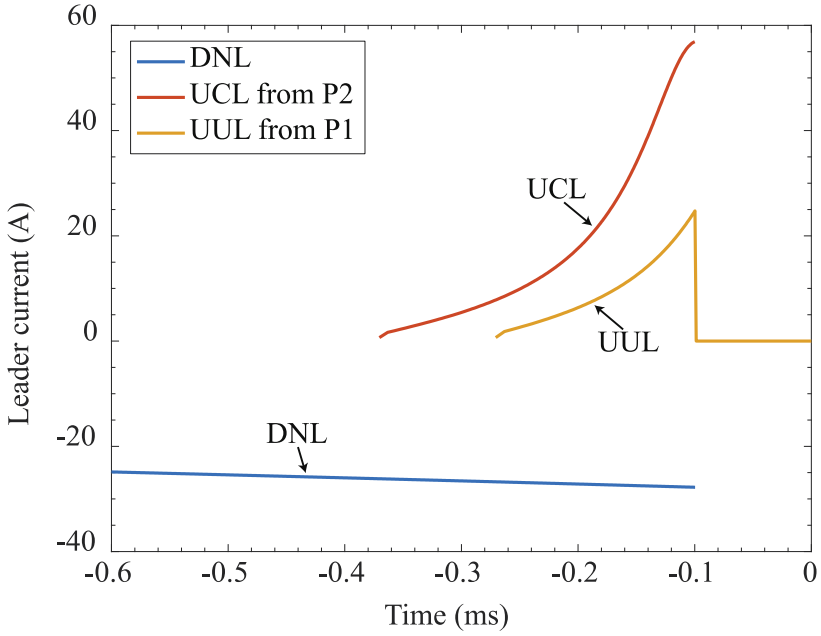

(a)

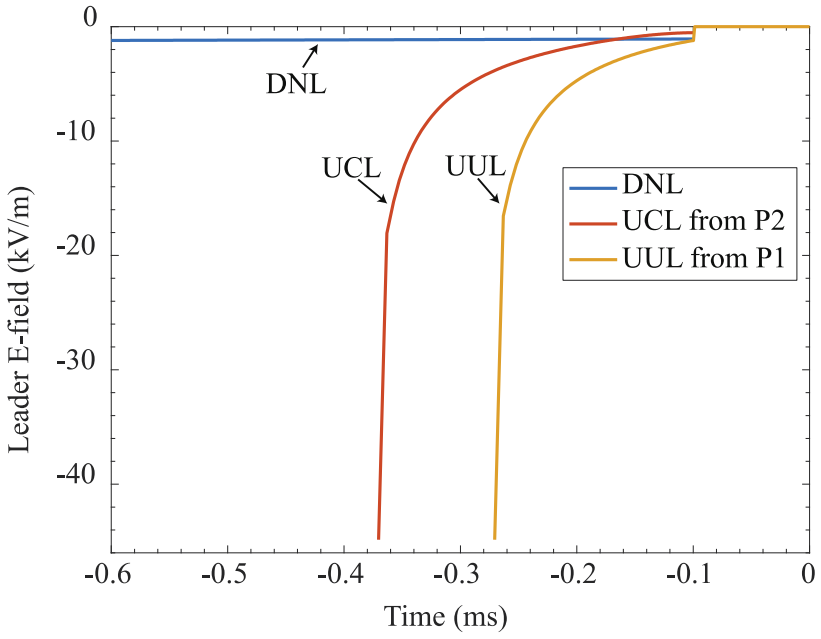

(b)

Figure 5.27. Simulation results (space charge layer near the ground is included): (a) Leader current verse propagation time, (b) Leader E-field verse propagation time (c) Leader conductance verse propagation time, and (d) Leader core radius verse propagation time.

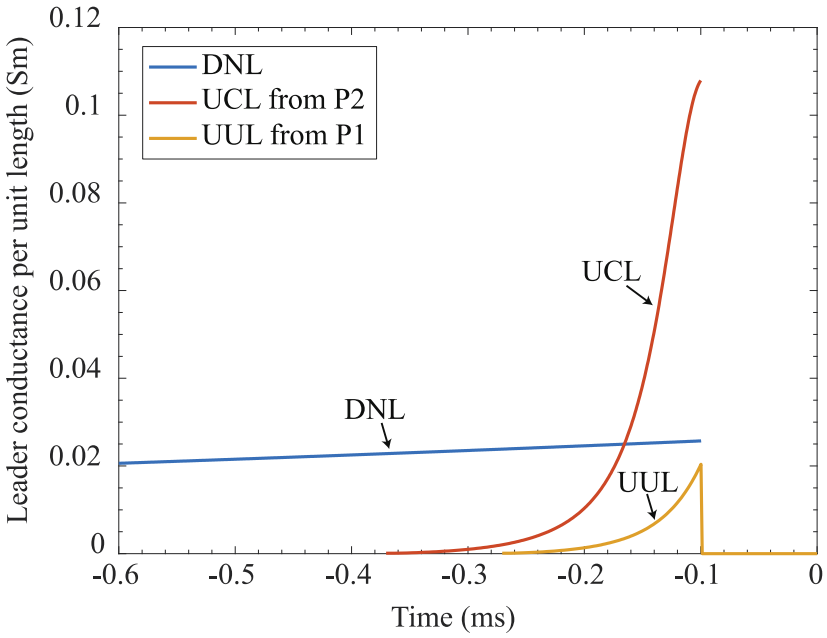

(c)

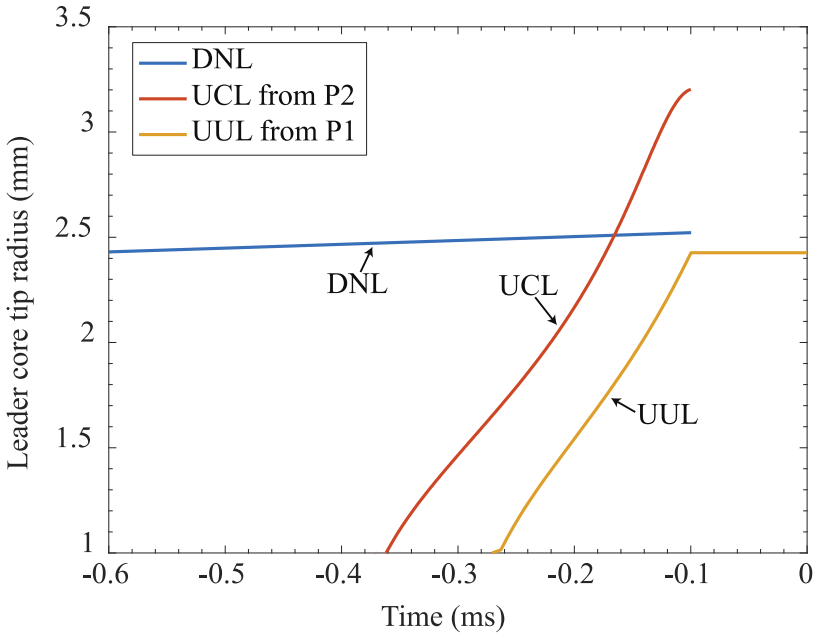

(d)

Figure 5.27. Simulation results (space charge layer near the ground is included): (a) Leader current verse propagation time, (b) Leader E-field verse propagation time (c) Leader conductance verse propagation time, and (d) Leader core radius verse propagation time.

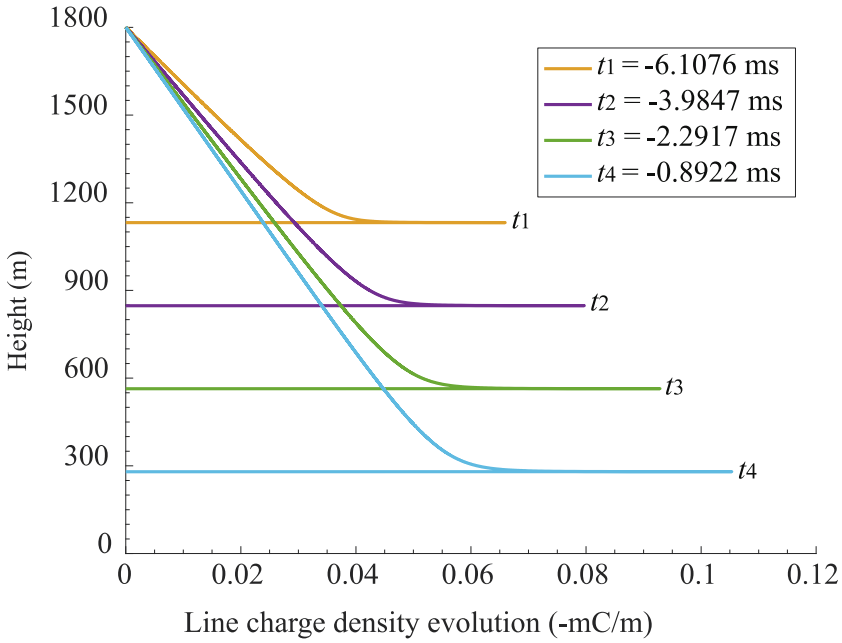

(a)

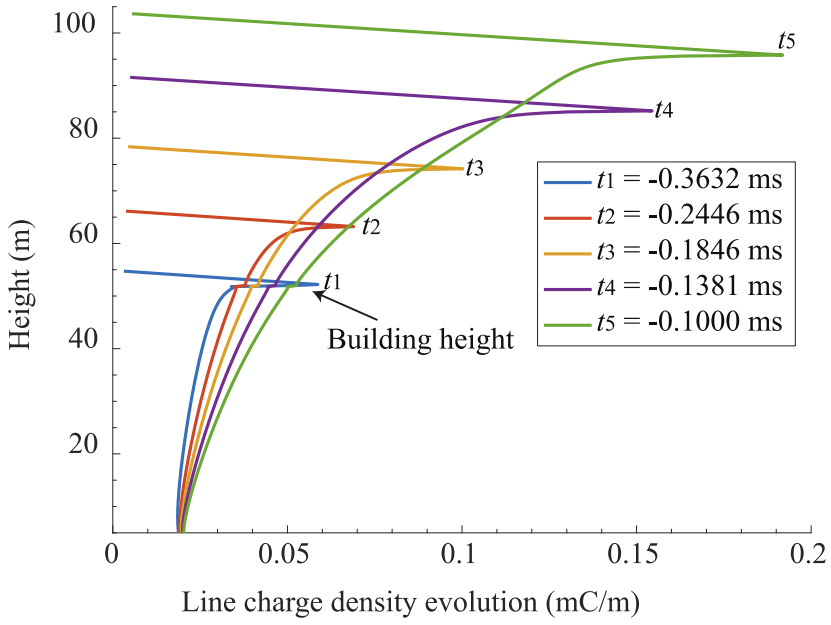

(b)

Figure 5.28. Line charge density evolution (space charge layer near the ground is included): (a) DNL, (b) UCL, and (c) UUL.

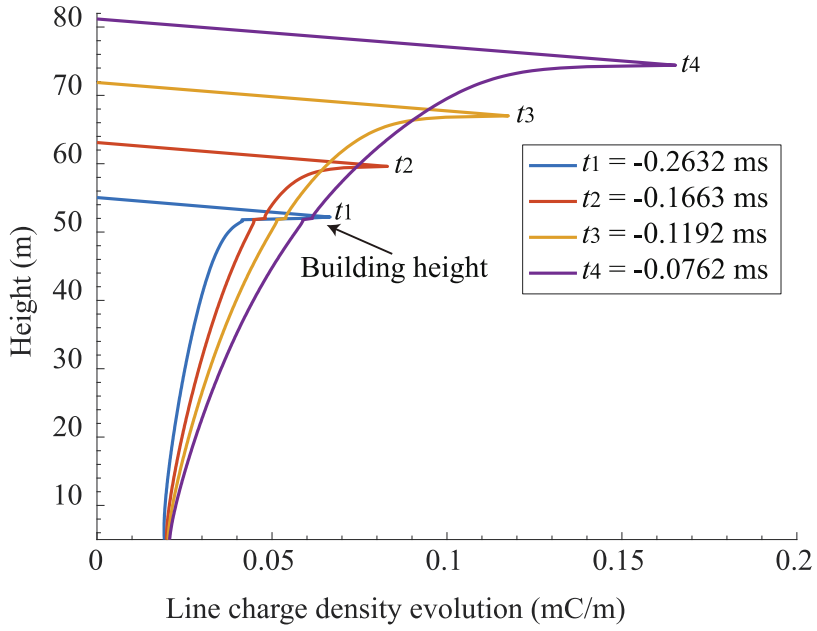

(c)

Figure 5.28. Line charge density evolution (space charge layer near the ground is included): (a) DNL, (b) UCL, and (c) UUL.

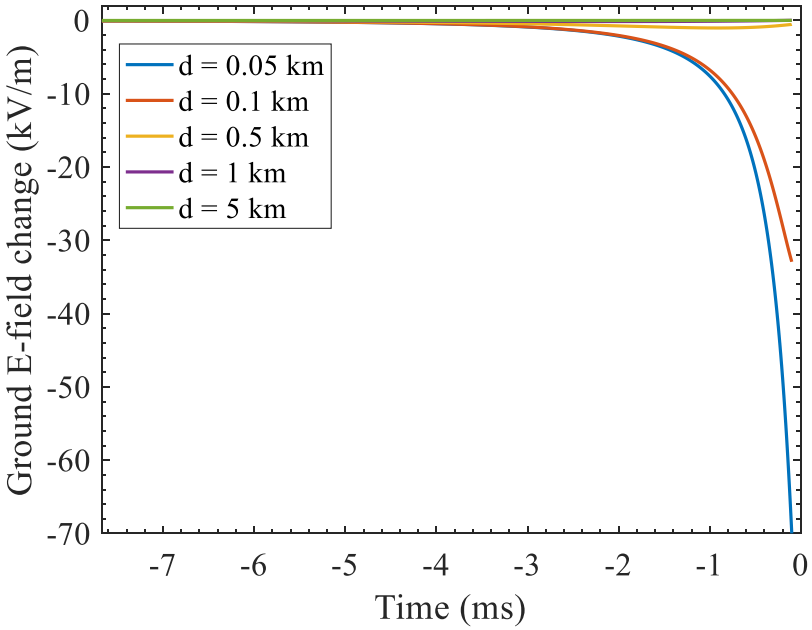

Figure 5.29. Ground E-field changes due to the DNL and UCL with different distance *d*, (blue) (*d* = 0.05 km), (red) (*d* = 0.1 km), (yellow) (*d* = 0.5 km), (purple) (*d* = 1 km), and (green) (*d* = 5 km) (space charge layer near the ground is included).

5.7 Case Study 2: an UCL Triggered from a 163-m tall tower by an Approaching DNL

In addition to common structures, in case study 2, a lightning stroke to a 163-m tower in works of (*Warner*, 2010), Case 1, 8/4/07, is adopted for modelling with the present model. Time 0 is again set at the beginning of the return stroke. From the reference, the author estimated the DNL was first entered the camera field of view at about 543 m and the inception time of UCL from the tower was about 1.665 +/- 0.135 ms prior to the return stroke. The attachment point was about 184 m from the tip of the tower.

According to the *Saba et al*. (2016b), they reported that the height of the thundercloud base in Rapid City is usually in a range of 2 - 4 km. They also estimated the altitude of the 163-m tower is about 1146 m. **Figure 5.30** shows a schematic diagram of the DNL, the UCL from the tower for modelling use. The DNL is simply assumed to propagate vertically towards the hill and the 163-m tower is assumed as a long lightning rods with a radius of 1 cm, placed on the hill. The horizontal distance (d) between the two leaders is assumed to be 50 m according to the reference (*Warner*, 2010). Again, a 500 m leader seed of the DNL is assumed to initiate from the cloud base at a height of 2.5 km. The values of E_{cloud}, E_{ground}, L_c, and τ_{d0} are -19 kV/m, -1 kV/m, 1.35 km, and 2.5 μs respectively. The simulated results are shown in **Figure 5.31**. From this figure, the inception height is estimated as 573.6 m.

Simulation result is a little different from the observation result because our model simplified the DNL as a straight line and we did not consider the effective height of the hill. However, all the differences are within the error bound.

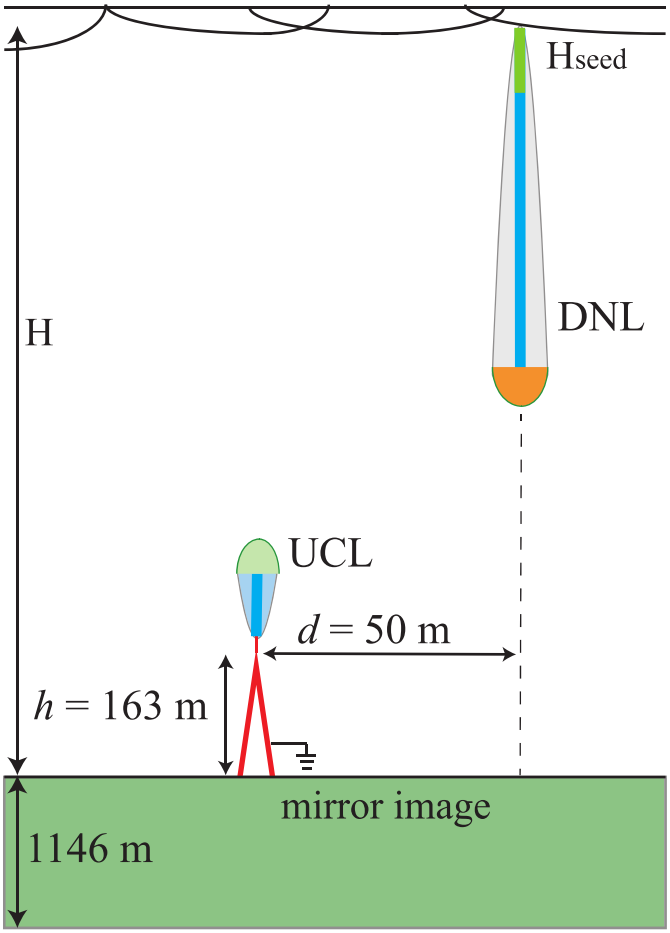

Figure 5.30. A schematic diagram of the DNL and UCL from a 163-m tower for modelling use (not drawn to scale).

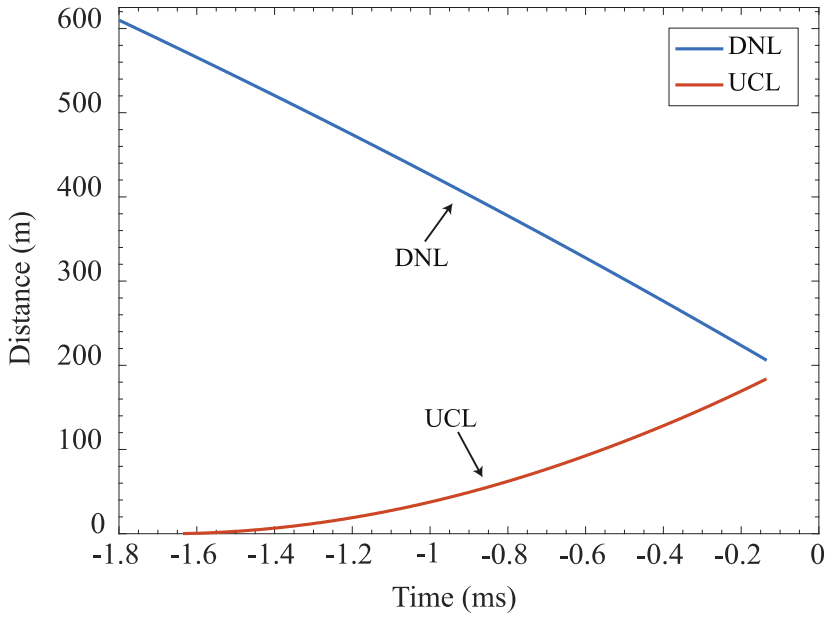

(a)

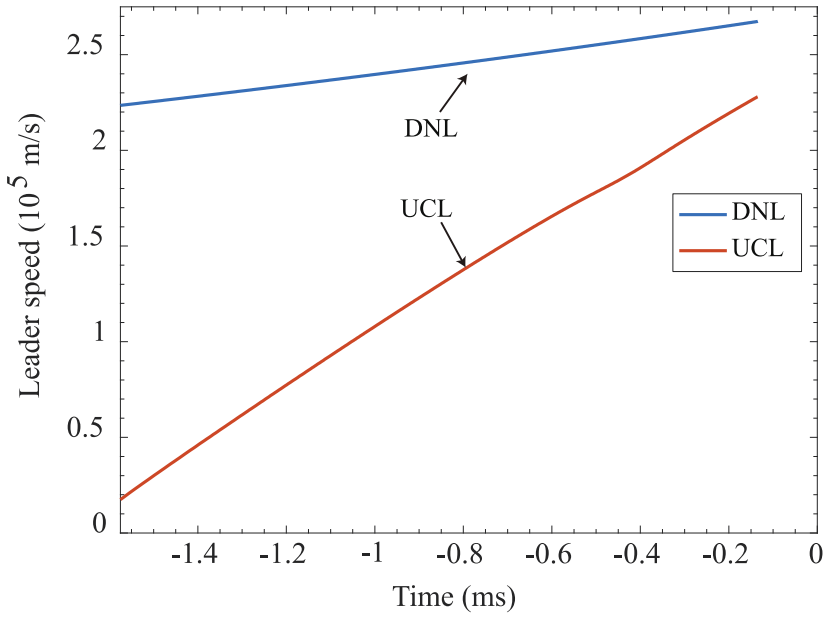

(b)

Figure 5.31. Simulation results (space charge layer near the ground is included): (a) the Distance-time graph and (b) the Speed-time graph.

5.8 Summary

This chapter introduces a downward stepped leader to a grounded object model before the final breakdown take places. The evaluation is performed with a modified physical leader model. A simple spatial and temporal electric field expression for both descending and ascending leaders is also derived respectively. This model can also be used to estimate the striking distance between the DNL tip and the top of the grounded object. The predictions of the model have been compared with two natural lightning observations of lightning attachment process with two different scenarios. Results are comparable with observations and those in literatures.

Chapter 6

Conclusions and Recommendations

6.1 Conclusions

In chapter 2, we briefly review some recent upward lightning observation results. Observation results have summarized three types of upward lightning discharges. In addition, the corona space charge layer near the ground is discussed, and some optical observation and lightning location techniques are reviewed.

In chapter 3, we have introduced a macroscopic self-triggered upward leader model. The main points of this model can be summarized as following:

i. A three-zone leader channel structure;
ii. The leader speed is subjected to the conservation of energy and mass inside the streamer-to-leader transitional zone around the leader head;
iii. The breakdown electric field is assumed as a function of height;
iv. A steady leader requires the leader initial speed (energy) should be larger than the minimum (critical) speed observed for leaders in both field and lab experiments ($\approx 10^4$ ms^{-1}), which corresponding to a critical corona sheath radius hence a critical corona sheath charge ahead of the leader;
v. The minimum initiation height is as a function of E_A;
vi. The leader charge distribution is calculated by the CSM;
vii. The leader will cease if its channel electric field is larger than E_A.

To insert a transition zone radius inside the leader channel, the radial electric field can increase from nearly zero to the E_C continuously. By fine-tuning the energy loss factor, the estimated critical corona sheath charge at ground-level can match well with experimental results as well.

In chapter 4, we present our simulation results with and without the corona space charge layer effect. Simulation results included speed, charge distribution, current, electric field, conductance and conductivity, channel size and temperature of the UPL. In addition, we fine turn the initial parameters to test with two experiment results. Although our model is simple, in the sense that it does not consider the details of plasma physics inside the leader channel, it works well in the prediction of main parameters of an UPL initiated from grounded objects. Simulation results show that if the space charge layer is included, the minimum self-initiation height becomes higher. The increasing trend of the proposed core radius equation can match well with experimental results as well.

In chapter 5, we introduce a lightning leader attachment model which can simulate downward stepped leaders to grounded objects. We compare our results with two natural lightning observations of lightning attachment process to two different buildings. Results are comparable with observations and those in literatures. The proposed lightning attachment model can also estimate other leaders' physical characteristics and the ground electric field change among different horizonal distances.

6.2 Limitations

i. Since the value of constant *b* is based on experiment, it may only be applied for currents in the range of 10^{-1} – 10^{2} A (Mazur and Ruhnke, 2014).

ii. The calculation of straight leader line charge density is based on the CSM. A

nature leader can also be branched and tortuous, so the simulation result of the line charge density is just an effective value.

iii. As the average step length is fixed, the microscopic stepwise propagating phenomenon of either positive or negative leader cannot be simulated.

iv. Our model has not considered the leader initiation process due to wind shear and air humidity effects.

v. Our model did not consider the shielding effect of a three-dimension local corona space charge layer near the ground and the effect of the rough earth surface.

vi. In chapter 5, we have neglected the electric field due to the upward leader. It may affect the down-coming leader. However, the difference is very small.

6.3 Summary of Model Characteristics

i. Many existing microscopic leader models assume either constant propagation speed or constant leader current. Our proposed macroscopic leader model can simultaneously estimate the overall leader speed and leader current.

ii. Since some physical parameters are height dependent, there is a maximum propagation speed for the upward leader. For some scenarios, the proposed overall continuous upward leader propagation speed can be further simplified as equation (2.9).

iii. Most of the existing downward leader models are applied the well-known Cooray's charge distribution equation [*Cooray et al.* 2014]. However, this equation requires the cloud base should be at least 3 km above the ground

[*Cooray et al.* 2006]. Usually, many existing models assumed the cloud base is fixed as 4 km high. We believe 4 km is too high for some observation results such as the case studies 1 and 2 [*Saba et al*. 2016]. The advantage of our model is we can estimate a relatively lower cloud base for charge calculation so that we can estimate a lower vertical ambient electric field as a function of space and time to match with observations.

iv. Engineering models assumed the striking distance is as a function of the perspective return stroke peak current. Our proposed striking distance estimation method is based on the ambient environment before the first return stroke take places which is more physical.

6.4 Recommendations for Further Research

6.4.1 Unusual Features of Negative Leaders' Development

A recent experiment has observed both downward and upward leaders that form in two cloud-to-ground lightning discharges. Our lightning attachment model described in chapter 5 can be modified further to simulate this phenomenon.

6.4.2 Upward Leaders Triggered by the First Return Stroke

A return stroke can initiate an upward leader. We can insert the electromagnetic field generated by the return stroke as an initial value to simulate unconnected upward leaders. This EM field may calculate from other Time-Domain Electric Field Integral Equation (TD-EFIE) model (*Cai et al*., 2017).

6.4.3 Striking Distance Estimation

By statistical analysis of the attachment to a given tall structure under various downward lightning events, one can estimate accurately the striking distance versus the lightning strength for the given tall structure and proposed a more physical relation among the perspective return stroke peak current, the cloud electric field, and the striking distance.

6.4.4 Other Applications

The model could be used to analyze the incidence and probability of upward lightning to a given tall structure based on the statistics of the ground electric field or vertical electric profile in the area the structure is located. With analyzing results, one optimizes the protection measures for effective protection, such as the optimal mast/lightning rod height etc.

References

Aleksandrov, N. L., and E. M. Bazelyan (1999), Ionization processes in spark discharge plasmas, *Plasma Sources Sci. Technol*., 8(2), 285–294.

Alessandro, F. D. (2003). The use of 'Field Intensification Factors' in calculations for lightning protection of structures. *J. Electrostat.*, 58, 17-43, doi.org/10.1016/S0304-3886(02)00178-X.

Asakawa, A., K. Miyake, S. Yokoyama, T. Shindo, T. Yokota, and T. Sakai (1997), Two types of lightning discharges to a high stack on the coast of the sea of Japan in winter, *IEEE Trans. Power Del*., 12, 1222–1231, doi.org/10.1109/61.636953.

Baba, Y. and Rakov, V.A., 2016. Electromagnetic Computation Methods for Lightning Surge Protection Studies, John Wiley & Sons Singapore Pte. Ltd.

Bazelyan, M, and P. Raizer, Lightning Physics and Lightning Protection, Bristol: Institute of Physics Publishing, UK, 2000.

Bazelyan, E.M., Y.P. Raizer, and N.L. Aleksandrov (2007). The effect of reduced air density on streamer-to-leader transition and on properties of long positive leader. *J. Phys. D: Appl. Phys.*, 40, 4133–4144.

Bazelyan E. M., Yu. P. Raizer, and N. L. Aleksandrov (2008), Corona initiated from grounded objects under thunderstorm conditions and its influence on lightning attachment, *Plasma Sources Sci. Technol*., 17, 024015.

Becerra, M., and V. Cooray (2006a), A self-consistent upward leader propagation model. *J. Phys. D*: *Appl. Phys*., 39, 3708–3715.

Becerra, M. and V. Cooray (2006b), A simplified physical model to determine the lightning upward connecting leader inception *IEEE Trans. Power Del*., 21, No.2, 897-908.

Becerra, M., V. Cooray, S. Soula, and S. Chauzy (2007), Effect of the space charge layer created by corona at ground level on the inception of upward lightning leaders from tall towers, *J. Geophys. Res.*, 112, D12205, doi.org/10.1029/2006JD008308.

Berger, K. (1977), The Earth Flash. In: Golde RH, Ed. Lightning, Part 1- Physics of Lightning: Academic Press.

Biagi, C. J., M. A. Uman, J. Gopalakrishnan, J. D. Hill, V. A. Rakov, T. Ngin, and D. M. Jordan (2011), Determination of the electric field intensity and space charge density versus height prior to triggered lightning, *J. Geophys. Res.*, 116, D15201, doi.org/10.1029/2011JD015710.

Boys, C.V. (1928), Progressive lightning, *Nature*, 118, 749-750.

Cai S., M. Chen, Y. Du, and Z. Qin (2017), A Leader-Return-Stroke Consistent Macroscopic Model for Calculations of Return Stroke Current and Its Optical and Electromagnetic Emissions, *J. Geophys. Res. Atmos.*, 122, doi.org/10.1002/2017JD026490.

Campos, L. Z. S., M. M. F. Saba, T. A. Warner, Jr. Pinto, O. Krider, E.P. Orville, R.E., (2014). High-speed video observations of natural cloud-to-ground lightning leaders — a statistical analysis, *Atmos. Res.* 136, 285–305, doi.org/10.1016/j.atmosres.2012.12.011.

Chan, M., M. Chen, and Y. Du (2018), A Macroscopic Physical Model for Self-Initiated Upward Leaders from Tall Grounded Objects and Its Application, *Atmos. Res.*, 200, 13-24, doi.org/10.1016/j.atmosres.2017.09.012.

Chen, M., N. Takagi, T. Watanabe, D. Wang, Z.-I. Kawasaki, and X. Liu (1999), Spatial and temporal properties of optical radiation produced by stepped leaders, *J. Geophys. Res.*, 104(D22), 27573–27584, doi.org/10.1029/1999JD900846.

Chen, M., T. Watanabe, N. Takagi, Y. Du, D. Wang, and X. Liu (2003), Simultaneous observations of optical and electrical signals in altitude-triggered negative lightning flashes, *J. Geophys. Res.*, 108, 4240, doi.org/10.1029/2002JD002676, D8.

Chen, M, and Y. Du (2009), Possible Impacts of Earthing Path Impedance on Lightning Return Stroke Currents, *HKIE Trans.*, 16, 1, 7–13.

Chen, M., X. Gou, and Y. Du (2013a), The effect of ground altitude on lightning striking distance based on a bi-directional leader model, *Atmos. Res.*, 125, 76-83.

Chen, M., D. Zheng, Y. Du, and Y. Zhang (2013b), Evolution of line charge density of steadily-developing upward positive leaders in triggered lightning, *J. Geophys. Res. Atmos.*, 118, 4670–4678, doi.org/10.1002/jgrd.50446.

Chen, S., R. Zeng, C. Zhuang, X. Zhou, and Y. Ding (2016), Experimental Study on Branch and Diffuse Type of Streamers in Leader Restrike of Long Air Gap Discharge, *Plasma Sci. T.*, 18, no.3.

Cooray, V., V. Rakov, and N. Theethayi (2006), The lightning striking distance-Revisited, J. Electrost., 65, 296-306, doi.org/10.1016/j.elstat.2006.09.008.

Cooray V., and M. Becerra (2010), Attachment of lightning flashes to grounded structures in: Cooray, V., Lightning Protection. IET, London, 165-268.

Cooray, V. (2013), On the attachment of lightning flashes to grounded structures with special attention to the comparison of SLIM with CVM and EGM, *J. Electrostat.*, 71, 577–581, doi.org/10.1016/j.elstat.2012.11.035.

Cooray, V. Mechanism of electrical discharges, Ch. 4 in The Lightning Flash 2nd edition, ed. V. Cooray, IET, London, 2014, 41-229.

Cooray, V., U. Kumar, F. Rachidi, and C. A. Nucci (2014), On the possible variation of the lightning striking distance as assumed in the IEC lightning protection standard as a function of structure height, *Electr. Power Syst. Res.*, 113, 79–87, doi.org/10.1016/j.epsr.2014.03.017.

da Silva, C. L., and V. P. Pasko (2013), Dynamics of streamer-to-leader transition at reduced air densities and its implications for propagation of lightning leaders and gigantic jets, *J. Geophys. Res. Atmos.*, 118, 13,561–13,590, doi.org/10.1002/2013JD020618.

Dellera, L., and E. Garbagnati (1990), Lightning stroke simulation by means of the leader progression model. I. Description of the model and evaluation of exposure of free-standing structures, *IEEE Trans. Power Del.*, 5(4), 2009–2022.

Diendorfer, G. (2014), Tower initiated lightning discharges, Ch. 7 in The Lightning Flash, 2nd edition, V. Cooray, IET, London, 41-229.

Dwyer, J. R., and M. A. Uman (2014), The physics of lightning. Phys. Rep., 534, 4.

Eriksson, A. J. (1987), An Improved Electrogeometric Model for Transmission Line Shielding Analysis, *IEEE Trans. Power Del.*, PWDR-2, 871–886, doi.org/10.1109/TPWRD.1987.4308192.

Fieux, R., C. Gary, and P. Hubert (1975), Artificially triggered lightning above land, *Nature*, 257, 212–214.

Gallimberti, I. (1979). The mechanism of long spark formation. *J. Physique. Physique Coll*, 40, 193–250.

Gallimberti, I., G. Bacchiega, A. Bondiou-Clergerie, and P. Lalande (2002), Fundamental processes in long air gap discharges, *C. R. Phys.*, 3, 1–25.

Hayenga, C. O., and J. W. Warwick (1981), Two-dimensional interferometric positions of VHF lightning sources, *J. Geophys. Res.*, 86(C8), 7451–7462, doi.org/10.1029/JC086iC08p07451.

Hill, J. D., M. A. Uman, and D. M. Jordan (2011), High-speed video observations of a lightning stepped leader, *J. Geophys. Res.*, 116, D16117, doi.org/10.1029/2011JD015818.

Jerauld, J., M. A. Uman, V. A. Rakov, K. J. Rambo, D. M. Jordan, and G. H. Schnetzer (2008), Electric and magnetic fields and field derivatives from lightning stepped leaders and first return strokes measured at distances from 100 to 1000 m, *J. Geophys. Res.*, 113, D17111, doi.org/10.1029/2008JD010171.

Kawasaki, Z. (2012), "Review of the Location of VHF Pulses Associated with Lightning Discharge," *J. Aerospace Lab*, 5.

Kito, Y., K. Horii, Y. Higashiyama, and K. Nakamura (1985), Optical aspects of winter lightning discharges triggered by the rocket-wire technique in Hokuriku district of Japan, *J. Geophys. Res.*, 90(D4), 6147–6157, doi.org/10.1029/JD090iD04p06147.

Lalande, P. (1996), Study of the lightning stroke conditions on a grounded structure, *Doctoral Thesis*, A publication of Office National d'Etudes et de Recherches *A'erospatiales* (ONERA).

Lalande, P and Mazur V (2012), A Physical Model of Branching in Upward Leaders, *J. AerospaceLab*, 5.

Lu, W., D. Wang, Y. Zhang, and N. Takagi (2009), Two associated upward lightning flashes that produced opposite polarity electric field changes, *Geophys. Res. Lett.*, 36, L05801, doi.org/10.1029/2008GL036598.

Lu, W., L. Chen, Y. Ma, V. A. Rakov, Y. Gao, Y. Zhang, Q. Yin, and Y. Zhang (2013), Lightning attachment process involving connection of the downward negative leader to the lateral surface of the upward connecting leader, *Geophys. Res. Lett.*, 40, 5531–5535, doi.org/10.1002/2013GL058060.

Malinga, G. A., and J. M. Niedzwecki (2015), Prediction of Lightning Interactions with Coastal and Offshore Wind Turbines, *JOWE*, 2, 81-88, doi.org/10.17736/jowe.2015.jcr28.

Mazur, V., L. H. Ruhnke, A. Bondiou-Clergerie, and P. Lalande (2000), Computer simulation of a downward negative stepped leader and its interaction with a ground structure, *J. Geophys. Res.*, 105(D17), 22361–22369, doi.org/10.1029/2000JD900278.

Mazur, V., and L. H. Ruhnke (2014), The physical processes of current cutoff in lightning leaders, *J. Geophys. Res. Atmos.*, 119, 2796–2810, doi.org/10.1002/2013JD020494.

McEachron, K.B. (1939), Lightning to the Empire State Building. *J. Franklin Inst.*, 227, 149-217.

Montanyà, J., O. van der Velde, and E. R. Williams (2014), Lightning discharges produced by wind turbines, *J. Geophys. Res. Atmos.*, 119, 1455–1462, doi.org/10.1002/2013JD020225.

Moore, C. B., K. B. Eack, G. D. Aulich, and W. Rison (2001), Energetic radiation associated with lightning stepped-leaders, *Geophys. Res. Lett.*, 28, 2141–2144, doi.org/10.1029/2001GL013140.

Nicoll, K. A. (2012), Measurements of atmospheric electricity aloft, *Surv. Geophys.*, 33(5), 991–1057, doi.org/10.1007/s10712-012-9188-9.

Oetzel, G. N., and E. T. Pierce (1969), VHF Technique for Locating Lightning, *Radio Sci*., 4(3), 199–202, doi.org/10.1029/RS004i003p00199.

Popov, N. A. (2010), Evolution of the Negative Ion Composition in the Afterglow of a Streamer Discharge in Air," *Plasma Phys. Rep.*, 36, 9, 812–818.

Qie, X., Y. Zhao, Q. Zhang, J. Yang, G. Feng, X. Kong, Y. Zhou, T. Zhang, G. Zhang, T. Zhang, D. Wang, H. Cui, Z. Zhao, and S. Wu (2009), Characteristics of triggered lightning during Shandong artificial triggering lightning experiment (SHATLE), *Atmos. Res.*, 91, 310-315.

Rakov, V.A., and M.A. Uman (2003), Lightning: Physics and Effects, Cambridge University Press, UK.

Rakov, V.A. (2016), Fundamentals of Lightning, Cambridge University Press, UK.

Riousset, J. A., V. P. Pasko, and A. Bourdon (2010), Air-density-dependent model for analysis of air heating associated with streamers, leaders, and transient luminous events, *J. Geophys. Res*., 115, A12321, doi.org/10.1029/2010JA015918.

Rizk, F. A. M. (1994), Modeling of lightning incidence to tall structures. I. Theory, *IEEE Trans. Power Del*., 9(1), 162–171, 1994.

Rizk, F. A. M. (2009), Modeling of Lightning Exposure of Buildings and Massive Structures, *IEEE Trans. Power Del*., 24, 4, 2009.

Rosy, B.R., U. Kumar, and R. Thottappillil (2011), A Macroscopic Model for First Return Stroke of Lightning, *IEEE Trans. Electromagn. Compat.*, 53(3), 782-791, doi.org/10.1109/TEMC.2010.2090663.

Saba, M. M. F., M. G. Ballarotti, and O. Pinto Jr. (2006), Negative cloud-to-ground lightning properties from high-speed video observations, *J. Geophys. Res*., 111, D03101, doi.org/10.1029/2005JD006415.

Saba, M. M. F., T. A. Warner, and C. Schumann, Features of lightning flashes obtained from high-speed video recordings, Ch. 5 in The Lightning Flash 2nd edition, ed. V. Cooray, IET, London, 2014, 231-266.

Saba, M. M. F., C. Schumann, T. A. Warner, J. H. Helsdon, and R.E. Orville (2015), High-speed video and electric field observation of a negative upward leader connecting a downward positive leader in a positive cloud-to-ground flash, *Electr*. *Pow*. *Syst*. *Res*., 118, 89-92, doi.org/10.1016/j.epsr.2014.06.002.

Saba, M. M. F., A. R. de Paiva, C. Schumann, J.C. de Oliveira e Silva, K.P. Naccarato, M.A.S. Ferro, and D.M. Custódio (2016a), Lightning attachment process to common buildings, 24th International Lightning Detection Conference and 6th International Lightning Meteorology Conference (ILDC/ILMC) 18th – 21st April 2016 (San Diego, California, USA).

Saba, M. M. F., C. Schumann, T. A. Warner, M. A. S. Ferro, A. R. de Paiva, J. Helsdon Jr, and R. E. Orville (2016b), Upward lightning flashes characteristics from high-speed videos, *J*. *Geophys*. *Res*. *Atmos*., 121, 8493–8505, doi.org/10.1002/2016JD025137.

Saraiva, A. C. V., et al. (2014), High-speed video and electromagnetic analysis of two natural bipolar cloud-to-ground lightning flashes, *J*. *Geophys*. *Res*. *Atmos*., 119, 6105–6127, doi.org/10.1002/2013JD020974.

Schonland, B.F.J (1956), The lightning discharge, *Handb*. *Phys*., 22, 576–628.

Sima, W., Y. Li, V.A. Rakov, Q. Yang, T. Yuan, and M. Yang (2014), An Analytical Method for Estimation of Lightning Performance of Transmission Lines Based on a Leader Progression Model. *IEEE Trans*. *Electromagn*. *Compat*., 56, 6, 1530-1539, doi.org/10.1109/TEMC.2014.2314772.

Stolzenburg, M., T. C. Marshall, W. D. Rust, and D. L. Bartels (2002), Two simultaneous charge structures in thunderstorm convection, *J. Geophys. Res.*, 107(D18), 4352, doi.org/10.1029/2001JD000904.

Stolzenburg, M., T. C. Marshall, W. D. Rust, E. Bruning, D. R. MacGorman, and T. Hamlin (2007), Electric field values observed near lightning flash initiations, *Geophys. Res. Lett.*, 34, L04804, doi.org/10.1029/2006GL028777.

Tran, M. D., V. A. Rakov, and S. Mallick (2014), A negative cloud-to-ground flash showing a number of new and rarely observed features, *Geophys. Res. Lett.*, 41(18), 6523–6529, doi.org/10.1002/2014GL061169.

Tran, M. D., and V. A. Rakov (2015), When does the lightning attachment process actually begin?. J. *Geophys. Res. Atmos.*, 120, 6922–6936, doi.org/10.1002/2015JD023155.

Toland, R. B., and B. Vonnegut (1977), Measurement of maximum electric field intensities over water during thunderstorms, *J. Geophys. Res.*, 82(3), 438–440, doi.org/10.1029/JC082i003p00438.

Wada, A., A. Asakawa, T. Shindo, and S. Yokoyama (2013), Leader and return stroke speed of upward-initiated lightning, *Proceedings Intern. Conf. Atmosph. Electricity* ICAE, C3-20, 2013.

Wang, D., and N. Takagi (2008a), Characteristics of upward bipolar lightning derived from simultaneous recording of electric current and electric field change, in Proceedings of the XXIX General Assembly of the International Union of Radio Science, Chicago, III.

Wang, D., N. Takagi, T. Watanabe, H. Sakurano, and M. Hashimoto (2008b), Observed characteristics of upward leaders that are initiated from a windmill and its lightning protection tower, *Geophys. Res. Lett.*, 35, L02803, doi.org/10.1029/2007GL032136.

Wang D., and N. Takagi (2012), Characteristics of winter lightning that occurred on a windmill and its lightning protection tower in Japan, *IEEJ Trans. Power Energy*, 132, 6, 568–572.

Wang, D., W. R. Gamerota, M. A. Uman, N. Takagi, J. D. Hill, J. Pilkey, T. Ngin, D. M. Jordan, S. Mallick, and V. A. Rakov (2014), Lightning attachment processes of an "anomalous" triggered lightning discharge, *J. Geophys. Res. Atmos.*, 119, 1524–1533, doi.org/10.1002/2013JD020787.

Wang, D., N. Takagi, W. R. Gamerota, M. A. Uman, and D. M. Jordan (2015), Lightning attachment processes of three natural lightning discharges, *J. Geophys. Res. Atmos.*, 120, 10,637–10,644, doi.org/10.1002/2015JD023734.

Wang, X., J. He., Z. Yu., R. Zeng, F. Rachidi (2016). Influence of ground wire on the initiation of upward leader from110 to 1000 kV AC phase line. *Electr. Power Syst. Res.*, 130, 103-112, doi.org/10.1016/j.epsr.2015.08.022.

Warner, T.A. (2010). Upward leader development from tall towers in response to downward stepped leaders, in 30th International Conference on Lightning Protection (ICLP) 13th Sep – 17th Sep 2010, **1069**, IEEE Power and Energy Soc., Cagliari, Italy.

Warner, T.A. (2012). Observations of simultaneous upward lightning leaders from multiple tall structures. *Atmos. Res.*, 117, 45–54, doi.org/10.1016/j.atmosres.2011.07.004.

Willett, J. C., D. A. Davis, and P. Laroche (1999), An experimental study of positive leaders initiating rocket-triggered lightning, *Atmos*. *Res*., 51, 189–219, doi.org/10.1016/S0169-8095(99)00008-3.

Williams, E. and S. Heckman (2012), Polarity asymmetry in lightning leaders: The evolution of ideas on lightning behavior from strikes to aircraft, *J. AerospaceLab*, 5, 1-8.

Wu, C., S. Xie, F. Qi, B. Li, J. Wan, and J. He (2013), Effect of corona discharges on the inception of positive upward leader-streamer system, *Int. J. Mod. Phys. B*, vol. 27, p. 1350165, doi.org/10.1142/S0217979213501658.

Wu, T., S. Yoshida, T. Ushio, Z. Kawasaki, Y. Takayanagi, and D. Wang (2014), Large bipolar lightning discharge events in winter thunderstorms in Japan, *J. Geophys. Res. Atmos*., 119, 555–566, doi.org/10.1002/2013JD020369.

Xu, W., S. Celestin, and V. P. Pasko (2014), Modeling of X-ray emissions produced by stepping lightning leaders, *Geophys. Res. Lett*., 41, 7406–7412, doi.org/10.1002/2014GL061163.

Xu, Y., and M. Chen (2013), A 3D self-organized leader propagation model and its engineering approximation for lightning protection analysis, *IEEE Trans. Power Del*., 28, 4, doi.org/10.1109/TPWRD.2013.2263846.

Zhou, X., R. Zeng, C. Zhuang, S. Chen (2015). Experimental study on thermal characteristics of positive leader discharges using Mach-Zehnder interferometry. *Phys. Plasmas*, 22, 63508, doi.org/10.1063/1.4922660.